



Universiteit  
Leiden

The Netherlands

## Spatial Coherence and Entanglement of Light

Di Lorenzo Pires, H.

### Citation

Di Lorenzo Pires, H. (2011, September 13). *Spatial Coherence and Entanglement of Light. Casimir PhD Series*. Retrieved from <https://hdl.handle.net/1887/17830>

Version: Not Applicable (or Unknown)

License: [Leiden University Non-exclusive license](#)

Downloaded from: <https://hdl.handle.net/1887/17830>

**Note:** To cite this publication please use the final published version (if applicable).

# **Spatial coherence and entanglement of light**

---

Henrique Di Lorenzo Pires

Copyright © 2011 by H. Di Lorenzo Pires.

Publisher: Casimir Research School, Leiden/Delft, the Netherlands.

Cover Design: Gildeprint drukkerijen and H. Di Lorenzo Pires

ISBN: 978-90-8593-104-1

# Spatial coherence and entanglement of light

---

## PROEFSCHRIFT

ter verkrijging van  
de graad van Doctor aan de Universiteit Leiden,  
op gezag van Rector Magnificus prof. mr. P. F. van der Heijden,  
volgens besluit van het College voor Promoties  
te verdedigen op dinsdag 13 september 2011  
klokke 13:45 uur

door

**Henrique Di Lorenzo Pires**

geboren te Belo Horizonte, Brazilië  
in 1984

## PROMOTIECOMMISSIE

Promotor:	Prof. dr. J. P. Woerdman	Universiteit Leiden
Coromotor:	Dr. M. P. van Exter	Universiteit Leiden
Leden:	Prof. dr. E. R. Eliel	Universiteit Leiden
	Prof. dr. C. W. J. Beenakker	Universiteit Leiden
	Prof. dr. D. Bouwmeester	Universiteit Leiden
	Prof. dr. G. Nienhuis	Universiteit Leiden
	Dr. M. J. A. de Dood	Universiteit Leiden
	Prof. dr. A. Lagendijk	Universiteit van Amsterdam en Universiteit Twente
	Dr. V. Zwiller	Technische Universiteit Delft

The work reported in this thesis is part of the research program of the Foundation for Fundamental Research on Matter (FOM), which is part of the Netherlands Organization for Scientific Research (NWO).

The research was carried out at the 'Leids Instituut voor Onderzoek in de Natuurkunde' (LION).

An electronic version of this dissertation is available at the Leiden University Repository (<https://openaccess.leidenuniv.nl>).

Casimir PhD series, Delft-Leiden 2011-15

*para os meus pais  
Antônio e Rosângela*



# Contents

<b>1</b>	<b>Introduction</b>	<b>1</b>
1.1	Light . . . . .	1
1.2	Coherence in optics . . . . .	2
1.2.1	Second-order coherence: classical and quantum description . . . . .	3
1.2.2	Fourth-order coherence and the two-photon field . . . . .	5
1.3	Research topics in this thesis . . . . .	7
<b>2</b>	<b>Near-field correlations in the two-photon field: A compact treatment</b>	<b>9</b>
2.1	Introduction . . . . .	10
2.2	Two-photon field in the image plane . . . . .	10
2.3	Experimental results and discussions . . . . .	13
2.4	Conclusion . . . . .	16
<b>3</b>	<b>Near-field correlations in the two-photon field: An extensive treatment</b>	<b>17</b>
3.1	Introduction . . . . .	18
3.2	Theory . . . . .	19
3.2.1	Analysis based on the angular spectrum . . . . .	20
3.2.2	Analysis based on volume integral over detection modes . . . . .	23
3.3	Experiment . . . . .	25
3.3.1	Experimental setup . . . . .	25
3.3.2	Results and discussion . . . . .	27
3.4	Conclusion . . . . .	35
	Appendix A . . . . .	35
	Appendix B . . . . .	36
<b>4</b>	<b>Effect of a strongly focused pump on type-I spontaneous parametric down conversion</b>	<b>39</b>
4.1	Classical equivalent source of parametric down conversion . . . . .	42
4.2	Near-field intensity measurements . . . . .	47
4.3	Near-field two-photon correlations . . . . .	50
4.4	Conclusion . . . . .	52

<b>5</b>	<b>Transverse mode entanglement in the two-photon field</b>	<b>55</b>
5.1	Introduction . . . . .	56
5.2	The Schmidt number: an operational definition . . . . .	56
5.3	Measuring the Schmidt number . . . . .	59
5.4	Conclusion . . . . .	62
	Appendix A . . . . .	63
<b>6</b>	<b>Orbital angular momentum spectrum of entangled two-photon states</b>	<b>65</b>
6.1	Introduction . . . . .	66
6.2	The OAM spectrum of SPDC . . . . .	67
6.3	Experiments and discussions . . . . .	68
6.4	Conclusion . . . . .	72
<b>7</b>	<b>Orbital angular momentum spectrum of partially coherent classical beams</b>	<b>73</b>
7.1	The OAM spectrum of partially coherent beams . . . . .	74
7.2	Experiments and discussions . . . . .	74
7.3	Conclusion . . . . .	79
<b>8</b>	<b>Spatial coherence of partially coherent classical beams with and without orbital angular momentum</b>	<b>81</b>
8.1	Introduction . . . . .	82
8.2	Cross-spectral density . . . . .	83
8.3	Propagation of a partially coherent beam . . . . .	85
8.4	Measurements of the spatial coherence . . . . .	90
8.5	Conclusion . . . . .	96
<b>9</b>	<b>Statistical properties of nonlocal speckles</b>	<b>97</b>
9.1	Introduction . . . . .	98
9.2	Theory . . . . .	98
9.3	Experimental results . . . . .	102
9.4	Conclusion . . . . .	105
	<b>Bibliography</b>	<b>107</b>
	<b>List of publications</b>	<b>121</b>
	<b>Summary</b>	<b>123</b>
	<b>Samenvatting</b>	<b>127</b>
	<b>Acknowledgements</b>	<b>133</b>
	<b>Curriculum vitae</b>	<b>135</b>

# 1

## Introduction

### 1.1 Light

It is quite difficult to introduce the notion of *light* avoiding any philosophical detour. Most of the time, physicists don't even bother to say what the light *is*; they are mainly interested in describing how it behaves. Quantum mechanics provides a very good description of the behavior of light (and matter) in most of its details and, in particular, on an atomic scale. However, as one of the fathers of quantum electrodynamics, Richard Feynman, once expressed [1]:

*At the quantum level things do not behave like waves, they do not behave like particles, they do not behave like clouds, or billiard balls, or weights on springs, or like anything that you have ever seen. Newton thought that light was made up of particles, but then it was discovered that it behaves like a wave. Later, however (in the beginning of the twentieth century), it was found that light did indeed sometimes behave like a particle. Historically, the electron, for example, was thought to behave like a particle, and then it was found that in many respects it behaved like a wave. So it really behaves like neither. Now we have given up. We say : "It is like neither."*

The behavior of the fundamental particles of light\*, known as *photons*, can be quite accurately described by a wave function. Although the photon is neither a particle nor a wave, within the paradigm of the wave-particle duality one is tempted to think that the photon will exhibit either a wave-like *or* a particle-like behavior. An evidence of wave-like properties is the observation of interference fringes in a Young double slit experiment. These fringes are, however, a signature of the *coherence* of light. By modifying this property one can also make the fringes disappear. In this case, the result of a Young's experiment would be very similar

---

\* We refer to any electromagnetic radiation, not only visible light.

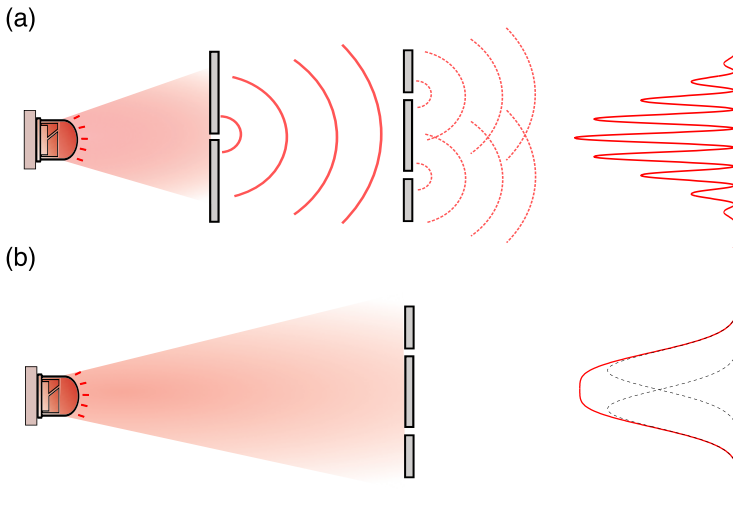


Figure 1.1: (a) Young's double-slit experiment. A monochromatic and incoherent light source is first filtered by a narrow slit and is then transmitted through two slits. An interference pattern is observed on a screen behind the slits; this is a signature of the coherence of the incident field. (b) The first aperture is removed and the interference pattern disappears. Since the incident field is now incoherent, the measured pattern is just the sum of the intensities transmitted by each aperture individually.

to what is expected from a stream of particles. Coherence is thus also one of the most fundamental concepts in both classical and quantum optics. With this notion in mind, let's revisit Young's experiment.

## 1.2 Coherence in optics

Coherence is the property of waves that allow them to interfere. For an ideal sinusoidal wave, if we know the amplitude and phase at a certain point in space, we know how this wave will be oscillating in the entire space. In other words, the swing of the wave at one point is perfectly correlated with all other points.

Figure 1.1(a) shows a schematic realization of the double-slit experiment. First, a thin slit is used to filter a light beam, producing to a good approximation a coherent *wave*<sup>\*</sup>. The light is then transmitted through a plate with two narrow slits and observed at a screen behind the slits. Since the oscillations at the upper and lower slits are perfectly correlated, these two sources will produce a high-contrast interference pattern. By removing the first plate, however, the interference pattern will disappear. As shown in Fig. 1.1(b), the result is now just the sum of the intensities transmitted through each aperture individually. The waves transmit-

\* We are describing the experiment in a classical language.

ted through both apertures don't "feel" each other and no interference occurs. In this situation we say that the two transmitted beams are *incoherent* with respect to each other. The relative phase of the oscillations at the two slits is completely random.

We have discussed the two extreme examples of complete coherence or complete incoherence. However, by changing the width of the first slit, one can continuously change from the situation in Fig. 1.1(a) to the situation in Fig. 1.1(b). The intermediate case corresponds to a *partially coherent* field. The field has both wave-like and particle-like behavior at the same time. Curiously, all these remarks remain true even at the single photon level. The patterns shown in Figs. 1.1(a) and (b) are then interpreted as the probability distribution of measuring the photon at a certain position.

The subject of coherence is extremely broad and rich. Entire books have been written on diverse aspects of coherence in different domains, such as space, time, frequency or polarization [2–4]. In this thesis we present an extensive study of spatial coherence of light, in particular for a field containing two photons, in which the quantum features become even more prominent. We begin by introducing some of the basic mathematical tools necessary to understand one-photon and two-photon spatial coherence.

### 1.2.1 Second-order coherence: classical and quantum description

The ingenuity behind Young's double slit experiment is that it allows the field at two different space-time coordinates to be superposed before measuring the combined intensity. In Fig. 1.1, the field at the position of the upper slit is diffracted and superposed with the field at the position of the lower slit. Other optical experiments can also be designed to allow such superposition, like a Michelson or a Mach-Zehnder interferometer. In general, when the field  $E^{(+)}(\mathbf{r}_1 t_1)$  at position  $\mathbf{r}_1$  and time  $t_1$  is superposed with  $E^{(+)}(\mathbf{r}_2 t_2)$ , the resulting intensity will be

$$\begin{aligned} I &= \left\langle \left| E^{(+)}(\mathbf{r}_1 t_1) + E^{(+)}(\mathbf{r}_2 t_2) \right|^2 \right\rangle, \\ &= I_1 + I_2 + 2\text{Re} \left[ \left\langle E^{(-)}(\mathbf{r}_1 t_1) E^{(+)}(\mathbf{r}_2 t_2) \right\rangle \right], \end{aligned} \quad (1.1)$$

with the understanding that  $E^{(+)}$  is the positive-frequency component of the complex representation of the electric field. The first two terms are the contributions of the intensities of each field individually, whereas the last term represents the interference effect of the superposed fields\*. The brackets  $\langle \dots \rangle$  denote time averaging<sup>†</sup>, as the measurement time is usually much longer than the period of

\* To be more precise, the fields should be physically superposed at the same point  $\mathbf{r}t$ . The interference term can then be written as  $\left\langle E_1^{(-)}(\mathbf{r}t) E_2^{(+)}(\mathbf{r}t) \right\rangle$ , where  $E_i$  is the transformation or propagation of the field at point  $\mathbf{r}_i t_i$  to the observation coordinate  $\mathbf{r}t$ .

† We assume a stationary stochastic process. In this situation, time averaging equals *ensemble* averaging.

the oscillation.

The coherence properties of the field is thus completely described by the correlation function

$$\Gamma(\mathbf{r}_1 t_1, \mathbf{r}_2 t_2) = \left\langle E^{(-)}(\mathbf{r}_1 t_1) E^{(+)}(\mathbf{r}_2 t_2) \right\rangle. \quad (1.2)$$

The field is said to be completely coherent if the correlation function factorizes in the form

$$\Gamma(\mathbf{r}_1 t_1, \mathbf{r}_2 t_2) = \mathcal{E}^*(\mathbf{r}_1 t_1) \mathcal{E}(\mathbf{r}_2 t_2). \quad (1.3)$$

This implies that there is a fixed phase relationship between  $\mathcal{E}(\mathbf{r}_1 t_1)$  and  $\mathcal{E}(\mathbf{r}_2 t_2)$  and the contrast of the interference fringes will be maximum. This is precisely the definition of coherence that optics has traditionally used.

In the quantum theory, measurable quantities, like the electric field, are no longer associated with a complex number  $E^{(+)}$ , but with an operator  $\hat{E}^{(+)}$ . The state of the system is represented by a vector or ket  $|\psi\rangle$ . The electric field operator  $\hat{E}^{(+)}$  is an annihilation operator in the sense that it lowers the number of quanta present in the field by one. Likewise, the Hermitian conjugate  $\hat{E}^{(-)} = [\hat{E}^{(+)}]^\dagger$  raises the number of quanta by one. If the field is in the pure state  $|\psi\rangle$ , the second-order coherence\* in quantum language is defined by

$$\Gamma(\mathbf{r}_1 t_1, \mathbf{r}_2 t_2) = \langle \psi | \hat{E}^{(-)}(\mathbf{r}_1 t_1) \hat{E}^{(+)}(\mathbf{r}_2 t_2) | \psi \rangle. \quad (1.4)$$

However, most light sources don't produce pure states. We should then consider the state  $|\psi\rangle$  as depending on some random and uncontrollable parameters of the source, for instance, the fluctuating relative phases between the fields at the two slits in Fig. 1.1(b). Partially-coherent fields in classical optics are represented by mixed states in the quantum language and are described by the density operator

$$\varrho = \{ |\psi\rangle \langle \psi| \}_{\text{av}}, \quad (1.5)$$

where we consider a statistical average over the fluctuating parameters. The most general quantum-theoretical form of the correlation function is

$$\begin{aligned} \Gamma(\mathbf{r}_1 t_1, \mathbf{r}_2 t_2) &= \left\{ \langle \psi | \hat{E}^{(-)}(\mathbf{r}_1 t_1) \hat{E}^{(+)}(\mathbf{r}_2 t_2) | \psi \rangle \right\}_{\text{av}}, \\ &= \text{Trace} \left\{ \varrho \hat{E}^{(-)}(\mathbf{r}_1 t_1) \hat{E}^{(+)}(\mathbf{r}_2 t_2) \right\}. \end{aligned} \quad (1.6)$$

For stationary fields, the correlation function depends per definition only on the time difference  $\tau = t_1 - t_2$ . For many applications, especially when monochromatic fields are involved, it is advantageous to work in the space-frequency domain. In this domain, one defines the *cross-spectral density*  $W$  as the Fourier

---

\* Second order on the electric field operators.

transform of the coherence function

$$W(\mathbf{r}_1, \mathbf{r}_2; \omega) = \int_{-\infty}^{+\infty} \Gamma(\mathbf{r}_1, \mathbf{r}_2; \tau) e^{i\omega\tau} d\tau. \quad (1.7)$$

Although the quantum treatment of coherence is generally carried out in the space-time domain, recent studies have provided a more exact formulation in the space-frequency domain. This quantum description can be made more comprehensible with the following notation. Let's consider a single photon with frequency  $\omega$  that can be in one of a set of orthogonal states  $\{|\psi_i\rangle\}$  with probabilities  $\{P_i\}$ . The density operator of this photon is then\*

$$\varrho = \sum_i P_i |\psi_i\rangle \langle \psi_i|. \quad (1.8)$$

The cross-spectral density is the spatial-coordinate representation of the density operator (Eq. 4.7-61 of Ref. [2]),

$$W(\mathbf{r}_1, \mathbf{r}_2; \omega) = \langle \mathbf{r}_1 | \varrho | \mathbf{r}_2 \rangle = \sum_i P_i(\omega) \psi^*(\mathbf{r}_1, \omega) \psi(\mathbf{r}_2, \omega). \quad (1.9)$$

This decomposition is known classically as the *coherent-mode representation*. It represents the field generated by the source as a linear combination of completely coherent fields; each of them can be found with probability  $P_i$ . The degree of coherence of the field is related to the number of terms in this modal decomposition. A completely coherent field has just one mode, whereas a completely incoherent field has infinite terms.

The description presented here is sufficient to understand earlier experiments on spatial coherence, in which single detectors were used to measure optical intensities or counting rates. In the 1950's, however, new experiments were developed that involved intensities or counts correlations between *two* detectors [5-7]. A more general theoretical approach was then necessary to explain, for instance, unexpected results on the correlations in the arrival times of photons. Such a generalization was introduced by Glauber, in his prestigious paper "quantum theory of optical coherence" [8]. In the next section we introduce the next higher-order correlation function.

### 1.2.2 Fourth-order coherence and the two-photon field

In order to elucidate coherence phenomena when correlations between multiple detectors are involved, Glauber defined higher order correlation functions  $\Gamma^{(2N)}$ . The previous section discussed the case  $N = 1$  of one detector. When two detec-

---

\* By a proper change of basis, the density matrix can always be written in a diagonal form.

tors are involved, the relevant function is

$$\Gamma^{(4)}(\mathbf{r}_1 t_1, \mathbf{r}_2 t_2, \mathbf{r}_3 t_3, \mathbf{r}_4 t_4) = \text{Trace} \left\{ \rho \hat{E}^{(-)}(\mathbf{r}_1 t_1) \hat{E}^{(-)}(\mathbf{r}_2 t_2) \hat{E}^{(+)}(\mathbf{r}_3 t_3) \hat{E}^{(+)}(\mathbf{r}_4 t_4) \right\}, \quad (1.10)$$

which is known as the fourth-order correlation function.

When only one detector is used, the measured light intensity is  $I(\mathbf{r}t) \propto \Gamma^{(2)}(\mathbf{r}t, \mathbf{r}t)$ . Similarly, when two detectors are used, the coincidences rate is given by  $R_c(\mathbf{r}_1 t_1, \mathbf{r}_2 t_2) \propto \Gamma^{(4)}(\mathbf{r}_1 t_1, \mathbf{r}_2 t_2, \mathbf{r}_2 t_2, \mathbf{r}_1 t_1)$ . Let's now focus our attention on a light field containing exactly two photons that are in a pure state  $|\psi\rangle$ . Since each of the electric field operators  $\hat{E}^{(\pm)}$  "annihilates" one photon from the field, the coincidence rate is [9–11]

$$\begin{aligned} R_c(\mathbf{r}_1 t_1, \mathbf{r}_2 t_2) &= \langle \psi | \hat{E}^{(-)}(\mathbf{r}_1 t_1) \hat{E}^{(-)}(\mathbf{r}_2 t_2) \hat{E}^{(+)}(\mathbf{r}_2 t_2) \hat{E}^{(+)}(\mathbf{r}_1 t_1) | \psi \rangle, \\ &= \left| \langle 0 | \hat{E}^{(+)}(\mathbf{r}_2 t_2) \hat{E}^{(+)}(\mathbf{r}_1 t_1) | \psi \rangle \right|^2, \\ &= |\mathcal{A}(\mathbf{r}_1 t_1, \mathbf{r}_2 t_2)|^2. \end{aligned} \quad (1.11)$$

The coincidence rate can thus be written as the modulus squared of a field  $\mathcal{A}(\mathbf{r}_1 t_1, \mathbf{r}_2 t_2)$ , which is known as the two-photon field. It gives the probability amplitude of detecting one photon at position  $\mathbf{r}_1$  and time  $t_1$  and the other photon at  $\mathbf{r}_2 t_2$ . Similarly to the cross-spectral density, one can also write the two-photon field in the frequency domain,  $A(\mathbf{r}_1 \omega_1, \mathbf{r}_2 \omega_2)$ , as the double Fourier transform of  $\mathcal{A}(\mathbf{r}_1 t_1, \mathbf{r}_2 t_2)$ . Much of this thesis is dedicated to investigate many of the very intriguing properties of the two-photon field, especially when both photons have the same frequency  $\omega$ , i.e., when they are frequency degenerate. This can be achieved experimentally by using narrow-band frequency filters. Under these conditions, the frequency dependence of the field is trivial, being determined by the filters only and will be omitted from the description from now on\*.

The function  $A(\mathbf{r}_1, \mathbf{r}_2)$  is the spatial-coordinate representation of the state  $|\psi\rangle$  and, like  $W$ , it can also be represented in a natural set of biorthogonal mode pairs as [12,13]

$$A(\mathbf{r}_1, \mathbf{r}_2) = \sum_i \sqrt{\lambda_i} f_i(\mathbf{r}_1) g_i(\mathbf{r}_2), \quad (1.12)$$

where  $f_i$  and  $g_i$  are the eigenstates and  $\lambda_i$  the respective eigenvalues. This representation is known as the Schmidt decomposition and it is closely related to the concept of *entanglement*.

Entanglement is an extraordinary quantum property that allows two or more particles (or degrees of freedom) to be strongly correlated. These correlations cannot be explained by any classical (local) model. Consider Eq. (1.12), for instance, which describes spatial entanglement between two photons. If we determine that one photon is in the state  $|f_i\rangle$ , we know for sure that the other photon will be in

---

\* The coincidences rate is given by a convolution of the two-photon field with the transmission functions of the filters,  $R_c = \int |A(\mathbf{r}_1 \omega_1, \mathbf{r}_2 \omega_2)|^2 T_1(\omega_1) T_2(\omega_2) d\omega_1 d\omega_2$ . We can only write  $R_c \propto |A|^2$  when the filters are sufficiently narrow-banded.

the state  $|g_i\rangle$ , even if these photons are separated by great distances. This property alone does not yet characterize spatial entanglement, as such correlations could in principle be classical\*. However, when measurements are made in different bases, the strong correlations persist. This persistence of correlations has no classical analogous. Entanglement is an old concept in quantum mechanics that has long challenged our understanding of nature, as it violates the philosophical principles of realism and locality. More recently, however, physicists have recognized that entanglement is also an important *resource*, with various applications in the now established field of quantum information. The amount of this resource present in the state (1.12) is related to the number of terms in the decomposition. A very common measurement of the effective number of entangled modes is the Schmidt number, defined by

$$K = \frac{1}{\sum_i \lambda_i^2}. \quad (1.13)$$

In the next chapters we will see how this number can be measured and manipulated.

There is certainly much more to be told about coherence, but the concepts introduced so far should be sufficient and indispensable in order to follow the remaining of this thesis. I wish you a pleasant reading!

### 1.3 Research topics in this thesis

In this thesis we investigate diverse aspects of spatial coherence of light. Non-classical fields containing two photons can be generated by a nonlinear optical process known as spontaneous parametric down conversion (SPDC), which will be described in more details in the coming chapters. Among the questions we consider are: What is so special about spatial entanglement? How is it revealed in the fourth-order correlations? What are the differences between a highly entangled and a classically correlated state? How can the number of modes be manipulated and measured? For a two-photon system, we measure both intensities and two-photon correlations. Therefore both second-order and fourth-order coherence are relevant. To get deeper insights into how coherence affects interference, we also investigate completely classical sources. The chapters are organized as follows:

- **Chapters 2 and 3** investigate the spatial properties of the two-photon field. Contrary to the far-field (i.e. momentum) properties, which are widely known, the near-field correlations in the two-photon field have hardly been studied. We find extremely rich structures and many interesting parallels with other fields of optics. Chapter 2 presents a short overview of the experiment and the most important results, while Chapter 3 provides a more

---

\* i.e., the mixed state  $\varrho = \sum_i \lambda_i^2 |f_i\rangle \langle f_i| \otimes |g_i\rangle \langle g_i|$ , which is completely classical, also exhibits the correlations just described.

complete theoretical description and extensive discussions on the consequences of the near-field structures.

- **Chapter 4** describes how the two-photon field is affected when the pump laser that generates entangled photons is strongly focused. We generate a state that is almost separable (i.e., non entangled) and investigate intensities and two-photon correlations. We also propose a semi-classical model of SPDC that explains the classical measurements made with a CCD.
- **Chapter 5** shows how the full dimensionality of the spatial entanglement can be manipulated and measured. We exploit a very interesting connection between second-order and fourth-order coherence in order to provide the first operational definition of the Schmidt number.
- **Chapter 6** investigates entanglement in orbital angular momentum (OAM) of light. Similar to the Schmidt decomposition introduced in Sec. 1.2.2, entanglement in OAM implies, in our geometry, that if one photon has an orbital angular momentum  $\ell\hbar$ , the other photon will have  $-\ell\hbar$ . We implement an interferometric method that allows the full probability distribution  $P_\ell$  of finding  $(\ell, -\ell)$  pairs to be measured.
- **Chapter 7** studies the orbital angular momentum spectrum of partially coherent light. Although most partially coherent fields do not carry an overall OAM, the statistical nature of the field implies that there is still a probability that the photon will have an angular momentum  $\ell\hbar$ . We show how the interferometric method and the theoretical framework of Chapter 6 can be used to investigate this OAM modal decomposition of partially coherent light. Contrary to the previous chapters, which focus on the quantum properties, this Chapter investigates completely classical beams.
- **Chapter 8** studies partially coherent classical light *with* an overall OAM. In particular, we address the question: “How does a spiral phase plate affect a partially coherent field?” Spiral phase plates are usually employed to transform a completely coherent beam into an approximate Laguerre-Gauss mode carrying OAM. When a partially coherent beam is used instead, the effect of the phase plate is shown to be much less visible in the intensity and much more dramatic in the coherence function, which now acquires a ring singularity.
- **Chapter 9** investigates the statistical properties of non-local speckle patterns that are obtained when entangled light is scattered through a random medium. In this Chapter, the connection between second-order coherence and fourth-order coherence is very prominent, as the statistics measured by a single detector and by two detectors are deeply linked. The differences between an entangled state and a separable state are very appealing. Finally, we use the statistics of the observed speckles as an alternative method to measure the Schmidt number. In this Chapter, many of the concepts discussed in the previous chapters are put together in a single context.

# 2

## Near-field correlations in the two-photon field: A compact treatment

We experimentally demonstrate how the two-photon field generated by spontaneous parametric down-conversion contains an intriguing fine structure associated with the positional spread within the photon pair. The obtained results provide a three-dimensional picture of the near-field correlations, which are determined by the phase-matching conditions. These correlations are compared with previous results on second-harmonic generation, spatial antibunching, and transverse entanglement in parametric down-conversion.

This Chapter presents a short overview of the experiment and the most important results, while the next chapter provides a more complete theoretical description and discussions on some consequences of the near-field structures. Both chapters are self-contained and can be read independently.

H. Di Lorenzo Pires and M. P. van Exter, *Observation of near-field correlations in spontaneous parametric down-conversion*, Phys. Rev. A **79**, 041801(R) (2009).

## 2.1 Introduction

Spatial entanglement between photons can be easily generated in spontaneous parametric down-conversion (SPDC), where a single pump photon splits into a pair of down-converted photons [14]. These nonclassical correlations have been essential in many landmark experiments on quantum entanglement, such as ghost interference [15], quantum lithography [16,17], and a recent demonstration of Bell inequalities with spatially-entangled modes [18]. Having a wide range of applications full knowledge of the spatial properties of the SPDC field is highly desirable.

Spatial correlations in any coherent two-photon field naturally occur on two length scales, being the spread in the “center of mass” of the photon pair and the “positional spread” within each pair. Most experiments operate in a regime where the first length scale, which is set by the width of the pump laser, is much larger than the structure that originates from the phase matching condition of the pair creation. This “fine structure” is then generally removed and conveniently replaced by a  $\delta$ -function in position and a uniform angular emission [19]. In this so-called thin-crystal limit, spatial entanglement boils down to the statement that the two-photon field contains a copy of the pump profile. We will go beyond this simplified approach.

This Chapter describes the experimental observation of a rich structure in the two-photon field that is associated with the spatial correlations originated from the phase-matching conditions. Apart from its intrinsic value, the obtained results provide a new link with prior experiments on second-harmonic generation (SHG) [20,21], spatial antibunching of photons [22,23] and measurements on two-photon position-momenta correlations [24,25]. Furthermore, some consequences of the observed structures to the spatial entanglement will be addressed.

## 2.2 Two-photon field in the image plane

In the absence of walk-off, the two-photon wavefunction in momentum representation has a special form, factorizing in two functions of the sum and difference transverse momenta as [19,26]

$$\tilde{A}(\mathbf{q}_1, \mathbf{q}_2) = \tilde{E}_p(\mathbf{q}_1 + \mathbf{q}_2) \tilde{V}(\mathbf{q}_1 - \mathbf{q}_2), \quad (2.1)$$

where  $\tilde{E}_p(\mathbf{q})$  is the angular spectrum of the pump beam and  $\tilde{V}(\mathbf{q}) = \text{sinc}(b^2|\mathbf{q}|^2 + \varphi)$  derives from the phase-matching conditions, with  $b^2 = L/8n_o k$ .  $L$  is the crystal thickness,  $k$  is the down-converted field wavevector,  $n_o$  is the refractive index at the down-converted frequency and  $\varphi$  is the phase mismatch parameter, which accounts for operation outside perfect phase matching. These momentum correlations can be measured in the far field, where each plane wave in the angular spectrum contributes to the field at a defined point. In that regime the “sinc” function, originated from the phase-matching conditions, is generally

much wider than the pump profile  $\tilde{E}_p$  and is often neglected in the analysis. We are interested, instead, in the near-field regime. There the opposite is true and the spatial representation of the phase-matching function shapes the position correlations within the photon pairs.

The problem can be analyzed considering the ideal imaging system (with unity magnification) depicted in the inset of Fig. 2.1. The probability amplitude of detecting two-photon coincidences at the image plane ( $z = 0$ ) is given by the Fourier transform of Eq. (2.1), which links transverse momenta  $\mathbf{q}$  to transverse coordinates  $\boldsymbol{\rho}$ . In the vicinity of  $z = 0$ , which corresponds to an image of the center of the crystal, the two-photon correlation assumes the form

$$A(\boldsymbol{\rho}_1, \boldsymbol{\rho}_2; z) = \iint_{-\infty}^{+\infty} d\mathbf{q}_1 d\mathbf{q}_2 \tilde{A}(\mathbf{q}_1, \mathbf{q}_2) \times \exp\left(-i\frac{q_1^2 + q_2^2}{2k}z\right) \exp(-i\mathbf{q}_1 \cdot \boldsymbol{\rho}_1 - i\mathbf{q}_2 \cdot \boldsymbol{\rho}_2), \quad (2.2)$$

where the first exponential accounts for the field propagation around the image plane and the second one is the Fourier kernel. It should be stressed that the plane  $z = 0$  contains contribution from all points inside the crystal and behaves as a secondary light source. Equation (2.2) also factorizes in two functions of the sum and difference coordinates  $A(\boldsymbol{\rho}_1, \boldsymbol{\rho}_2; z) = E_p(\frac{\boldsymbol{\rho}_1 + \boldsymbol{\rho}_2}{2}; z)V(\boldsymbol{\rho}_1 - \boldsymbol{\rho}_2; z)$ . It is straightforward to show that for a wide pump beam the two-photon field depends dominantly on the difference coordinate  $\boldsymbol{\rho}_- = \boldsymbol{\rho}_1 - \boldsymbol{\rho}_2$  in the image plane,

$$V(\boldsymbol{\rho}_-; z) \propto \int_{-\infty}^{+\infty} d\mathbf{q} \tilde{V}(2\mathbf{q}) \exp\left(-i\frac{|\mathbf{q}|^2}{k}z - i\mathbf{q} \cdot \boldsymbol{\rho}_-\right). \quad (2.3)$$

The coincidence counting rate measured by point-like detectors placed in transverse positions  $\boldsymbol{\rho}_1$  and  $\boldsymbol{\rho}_2$  at plane  $z$  is then  $R_{cc} \propto |V(\boldsymbol{\rho}_-; z)|^2$ .

A more realistic description must take into account the finite resolution of the detectors. Working with single-mode (fiber-coupled) detectors centered at  $\boldsymbol{\rho}_1$  and  $\boldsymbol{\rho}_2$ , the measured two-photon field will then be given by an overlap integral of the generated field and the Gaussian profile  $\phi$  of the detection modes

$$V_{project}(\boldsymbol{\rho}_-; z) \propto V * \phi(\boldsymbol{\rho}_1) * \phi(\boldsymbol{\rho}_2), \quad (2.4)$$

where  $*$  denotes the convolution integral. Using compact detection modes, the thus-obtained projected two-photon field will closely resemble the generated field  $V(\boldsymbol{\rho}_-; z)$  and can be regarded as a smoothed version thereof.

Figure 2.1 shows the experimental setup used to observe the near-field structure in the two-photon field. In our experimental implementation we use a magnified (instead of a 1:1) imaging system. Entangled photon pairs of equal polarization are generated by mildly focusing ( $w_p = 157 \mu\text{m}$ ) a laser beam ( $\lambda_p = 413.1 \text{ nm}$ )

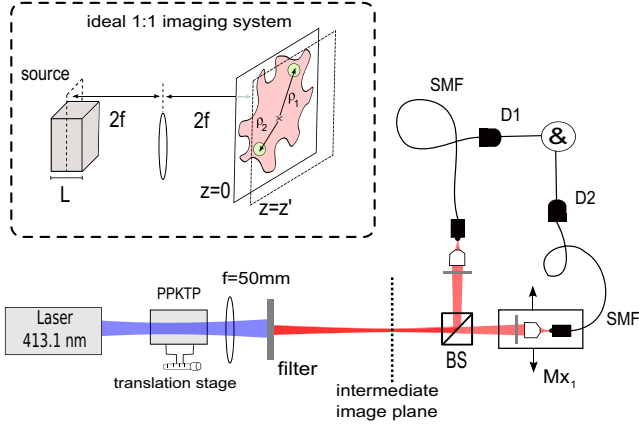


Figure 2.1: Experimental setup for measuring the near-field correlations in the two-photon field. The inset shows an ideal 1:1 imaging system, where  $z = 0$  is defined as the image plane with respect to the center of the crystal. We are interested in probing the spatial correlations in the vicinity of the image plane. The inset also illustrates how the finite resolution of the detectors should be included in the description. In our experimental implementation we use a  $13\times$  magnified imaging system. Spatially-entangled photon pairs generated in PPKTP are separated at a beam splitter, selected with filters (spectral width  $5\text{nm}$  @  $826\text{nm}$ ) and detected by photon counters and coincidence electronics ( $D1, D2$ ). Only coincidence counts within a time window of  $1.4\text{ ns}$  are considered. The crystal position can be adjusted by a translation stage. A  $f=50\text{ mm}$  lens is used to make a  $13\times$  magnified image of the near field onto an intermediate plane, which is then imaged onto single-mode optical fibers by objective lenses. It is important to remark that all transverse planes inside the crystal contribute coherently to this “image”.

on a  $L = 5\text{ mm}$ -thick PPKTP crystal, whose transverse dimensions are much larger than the pump width. The refractive index  $n = 1.843$  for PPKTP at  $\lambda_0 = 826.2\text{ nm}$  and  $T \approx 60^\circ\text{C}$ . A  $f=50\text{ mm}$  lens makes a  $M = 13\times$  magnified image of the near-field onto an intermediate plane, which is then demagnified by a factor  $1/28\times$  by imaging it with objectives onto the input tips of two optical fibers. The transverse correlations are measured by keeping detector 2 centered at  $M\rho_2 = 0$  and moving detector 1 horizontally over  $Mx_1 = M|\rho_1|$ . To measure the longitudinal ( $z$ ) dependence of the correlations, we move the crystal with a translation stage around the “object plane” of the lens. This will displace the near-field structure in the vicinity of the image plane. The on-axis phase mismatch  $\varphi(T)$  can be adjusted by setting the temperature of the crystal. The derivative  $d\varphi/dT \approx 1.04\text{ K}^{-1}$  was calculated and checked experimentally [27]. The waist of the Gaussian detection modes,  $w_d = 80\text{ }\mu\text{m}$  at the image plane and  $6.7\text{ }\mu\text{m}$  at the crystal, was chosen to provide a good trade-off between resolution and detection efficiency.

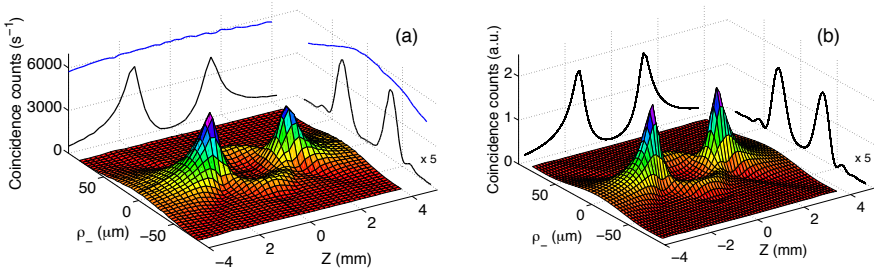


Figure 2.2: (a) Measured coincidence rate  $R_{cc}(\rho_-, z) \propto |V_{\text{project}}(\rho_-; z)|^2$  at a phase mismatch  $\varphi = 2.0 \pm 0.1$ . The intersections with the  $\rho_- = 0$  and  $z = 0$  planes are projected on the back and lateral side of the plot. The transverse correlations for  $z = 0$  are amplified 5 times on the lateral plane. The upper (blue) curves represent similar projections of the single count rate of the scanning detector (not in scale; full intensity distribution not shown). (b) Theoretical results as predicted by Eq. (2.4). No fitting parameters are necessary.

## 2.3 Experimental results and discussions

Figure 2.2(a) shows the full spatial dependence of the coincidence counting rate  $R_{cc}(\rho_-, z) \propto |V_{\text{project}}(\rho_-; z)|^2$  for the interesting phase mismatch  $\varphi = +2.0 \pm 0.1$ . The projections of the  $\rho_- = 0$  and  $z = 0$  curves are shown on the back and lateral planes, respectively. The single count rate ( $\propto$  optical intensity) is practically constant over this scan, as indicated by the upper curves in the two projections (the full intensity surface is not shown). The experimental results are in perfect agreement with the theoretical prediction obtained from Eq. (2.4) and depicted as Fig. 2.2(b).

The three-dimensional reconstruction of the coincidence counting rate displays intriguing structures. For positive phase mismatch, as in Fig. 2.2, there are two well pronounced peaks in the coincidence profile which are separated by the imaging optical thickness of the crystal  $L/n \approx 2.7$  mm. The physical origin of this structure can be understood as follows. The crystal acts as a longitudinally extended source of photon pairs. The phase matching conditions determine the relative phase of photon pairs born at different planes within the pumped region. The final probability amplitude of detection is given by the sum of all contributions from many creation sites inside the crystal and propagated to the image plane. A fourth-order interference effect will lead then to the observed result. The change of an on-axis interference peak to an interference valley after free-space propagation also appears in the context of Fresnel diffraction. However, one must emphasize that the observed peculiar interference structure is only present in the fourth-order correlation function, as the single count rates remain approximately constant during the scans.

It is possible to show that for points on-axis ( $\rho_- = 0$ ) our mathematical description becomes identical to a classical expression used in non-linear optics for the efficiency of second harmonic generation in a medium pumped by a

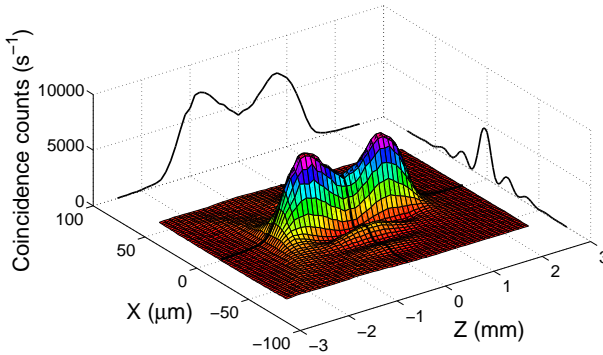


Figure 2.3: Measured coincidence rate  $R_{cc}(\boldsymbol{\rho}_-, z) \propto |V_{\text{project}}(\boldsymbol{\rho}_-, z)|^2$  at a phase mismatch  $\varphi = -5.2 \pm 0.1$ . The intersections with the  $\boldsymbol{\rho}_- = \mathbf{0}$  and  $z = 0$  planes are projected on the back and lateral side of the plot.

tightly focused Gaussian beam. The classical counterpart of our results has been predicted and observed a long time ago [20,21]. However, to the best of our knowledge, this is the first experimental observation of a similar effect in the context of SPDC. By properly setting the phase-mismatch parameter  $\varphi$  many of the longitudinal correlations presented in [20] can also be obtained with SPDC light.

The central part of Fig. 2.2 exhibits an almost total suppression of coincidence counts (but not of singles) for points on-axis. The observation of this on-axis minimum is an experimental proof of the quantum nature of the field and the presence of spatial antibunching. This statement is based on the work by Nogueira *et al.* [22], who have shown that the fourth-order correlation function of any classical homogeneous field, where  $\langle I(\boldsymbol{\rho}_1)I(\boldsymbol{\rho}_2) \rangle \propto R_{cc}(\boldsymbol{\rho}_1, \boldsymbol{\rho}_2)$  is a function of  $\boldsymbol{\rho}_- = \boldsymbol{\rho}_1 - \boldsymbol{\rho}_2$  only, should obey a Cauchy-Schwarz type inequality. For our correlations, which is homogenous as  $V(\boldsymbol{\rho}_-)$  depends only on  $\boldsymbol{\rho}_-$ , this classical inequality reads

$$|V(\boldsymbol{\rho}_-)|^2 \leq |V(\mathbf{0})|^2. \quad (2.5)$$

The violation of inequality (2.5) observed in Fig. 2.2 therefore implies that the generated two-photon field is non-classical and spatially antibunched; the field is at the same time homogeneous and reveals destructive fourth-order interference for  $\boldsymbol{\rho}_- = \mathbf{0}$  in the image plane. This is perhaps the simplest and most direct method up to date to observe spatial antibunching in the two-photon field.

By varying the phase mismatch  $\varphi$  many different three-dimensional profiles can be obtained. As another example, Fig. 2.3 shows the spatial correlations measured for  $\varphi = -5.2 \pm 0.1$ . Notice the prominent ripples in the transverse correlations observed in the  $z = 0$  plane. Both coincidences profiles in Fig. 2.2 and Fig. 2.3 are symmetric with respect to the  $z = 0$  plane, as predicted by

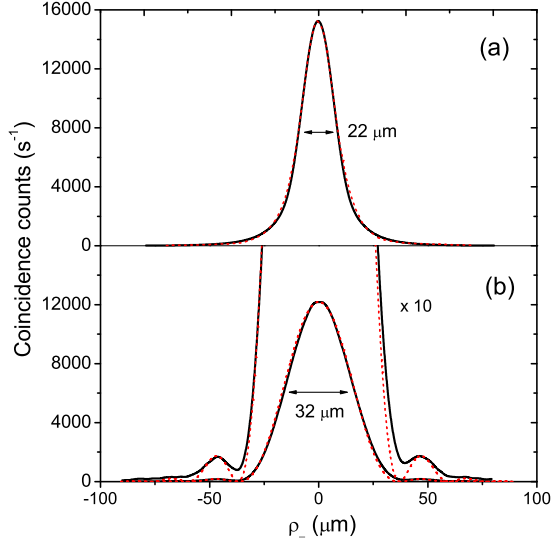


Figure 2.4: Transverse correlations close to perfect phase-matching ( $\varphi = 0.0 \pm 0.2$ ) for the crystal facet imaged on the detection plane (a) and the center of the crystal imaged (b). The solid curves are the experimental data while the dashed curves are theoretical predictions. The  $10\times$  magnified plot shows the agreement between theory and experiment also at the side bumps. The indicated FWHM of the curves varies with the focused plane. The ratio between the peak heights  $\approx 1.25$ .

Eq. (2.3).

Since we have now a complete understanding of the structure of the two-photon field in the near-field regime, we can revisit previous works that were analyzed under certain approximations. In a recent experiment of Howell *et al.* [25] measurements of position correlations were used to violate separability criteria in a realization of the EPR paradox. One of the key results was the measured conditional variance  $(\Delta x_1|_{x_2})^2$ , which was taken at a single plane in the near field. In Fig. 2.4 we show the measured transverse correlations at perfect phase matching ( $\varphi = 0$ ), with the crystal facet imaged at the detection plane (4a) and at the center of the crystal (4b). The calculated variance  $(\Delta x_1|_{x_2})^2$  for these two plots differs by 35%, implying that the variance product used to quantify the EPR paradox is not unique. On the other hand, it is well known that the amount of entanglement cannot change under free-space propagation. These differences are due to the fact that the considered uncertainty relations are based on intensity measurements, whereas entanglement can also exist in the phase of the two-photon field. In this way we provide experimental support to the proposed migration of entanglement in Hilbert space between amplitude and phase [30].

Note that one cannot interpret the results shown in Fig. 2.4 as the probability distribution of the “relative birthplace” of the photons [25], as the correlations obtained are a consequence of interference of photons generated at all possible sites in the crystal. This point can be strengthened by considering the observed spatial antibunching in Fig. 2.2, which is not in contradiction with the assumption of localized emission.

## 2.4 Conclusion

In conclusion, we have reported the first complete experimental observation of the near field structure in the two-photon field. Contrary to the predominant view in literature, the exact form of the phase-matching function leads to striking observable effects, such as many complex and intriguing structures in the transverse correlations, longitudinal correlations that resemble those observed in SHG with tightly-focused beams and a new way of producing spatial antibunching. The fact that these correlations can be easily measured may open a new window on experimental studies of continuous-variable entanglement. First, it allows one to corroborate and compare different proposed entanglement measures [13, 28, 29] in the near-field regime. Additionally, issues like the behavior of entanglement under propagation can be addressed. Finally, previous works that were analyzed under approximations regarding the near field correlations in SPDC, e.g., realization of the EPR paradox [25], quantum optical lithography [16, 17], and entanglement migration in Hilbert space [30], can now be revisited.

# 3

## Near-field correlations in the two-photon field: An extensive treatment

In experiments with spontaneous parametric down conversion the near-field plane is usually defined as the output facet of the generating crystal. Experimentally, however, the spatial correlations are accessed via an imaging system and observed in a region around the image of the output facet. We show that the imaged two-photon field has a very rich transverse and longitudinal structure, which is determined by the phase-matching conditions. We observe many intriguing three-dimensional structures that demonstrate the presence of spatial antibunching, an extreme localization of twin photons, and spatial correlations that resemble Bessel beams in propagation. We link these observations with previous results in second harmonic generation and predict the presence of fourth-order phase singularities. Both experiments and theory are presented, yielding further insight into the nature of the two-photon field.

H. Di Lorenzo Pires and M. P. van Exter, *Near-field correlations in the two-photon field*, Phys. Rev. A **80**, 053820 (2009).

### 3.1 Introduction

Observations of multifold photon count statistics have played a major role in both classical and quantum optics since the seminal paper of Hanbury Brown and Twiss [5]. A prominent example of a field that displays intriguing higher-order correlations is the two-photon field generated by spontaneous parametric down conversion (SPDC) [9,31]. In this process a laser beam pumps a dielectric nonlinear crystal, generating highly correlated pairs of down-converted photons. These so called “twin photons” or “biphotons” have been employed in several landmark experiments on fundamental concepts of quantum mechanics, such as violation of Bell’s inequalities [18,32], quantum teleportation [33], quantum cryptography [34], and a realization of the EPR paradox using momentum and position entangled photons [25]. SPDC light still stands out as the most versatile sources of entangled photon pairs.

Having a wide range of applications, full knowledge of the spatial properties of the two-photon field generated by SPDC is highly desirable. The quantum aspects of the spatial correlations are revealed not in the lowest-order correlation function, associated with the “one-photon” spatial coherence, but in the next higher order, which can be probed in the lab by performing two-photon coincidence measurements. These non-classical correlations are a signature of the spatial (mode) entanglement, which makes SPDC interesting for the field of quantum information.

The complete wave-function of the two-photon field generated by SPDC is well known from theory [13,25,35,36]. It contains two essential ingredients, being the shape of the pump beam and the phase matching conditions associated with the crystal geometry. The *angular* representation of this two-photon field has been studied extensively. Its contains a substructure that includes the full spatial information of the pump beam [19] and that shows up only in the fourth-order field correlations, but not in the second-order ones. As such, these angular correlations have formed the basis of many quantum experiments with entangled photon pairs. On the other hand, the *spatial* representation of the generated two-photon field has been hardly studied and many intriguing aspects of this field have gone unnoticed up to now. These spatial aspects, which we will denote as “near-field correlations” or “fine structure” of the two-photon field, form the heart of this Chapter. They are associated with the phase matching of the SPDC process [26,35,37]. Their theoretical description requires one to go beyond the Gaussian approximation of phase matching [38], or the delta-type approximation applicable to thin crystals, but use the proper phase-matching condition instead [13,25,35,36].

Experimentally, the near-field correlations are measured by imaging the output facet of the generating crystal on the detection plane. For instance, a single plane measurement at perfect phase matching has been used in a realization of the Einstein-Podolsky-Rosen paradox [25]. This measurement was then interpreted as an image of the relative birthplace of down-converted photons. One

must realize, however, that SPDC is a coherent process in which light generated at all transverse planes inside the crystal contributes to the measured field in the image plane. In other words, an image of the output facet of the crystal does not simply provide information about the relative birthplace of the photon pairs, but is a consequence of a fourth-order interference effect. As we will show, the symmetry of the process is such that an “image” of the input facet of the crystal provides exactly the same transverse correlations as one from the output facet. However, strong differences arise if one images the center of the crystal. Contrary to what is usually believed, the transverse and longitudinal correlations in the vicinity of the image plane are nontrivial and reveal a very rich structure.

In this Chapter we will show experimentally how the finite thickness of the crystal results in a rich set of spatial correlations in the image plane of the crystal. The complete spatial dependence, both in transverse and longitudinal coordinates, is presented. Operation under phase mismatch leads to many intriguing effects and will be extensively discussed. A few results were already introduced in Chapter 2 (Ref. [39]). Here we will present the theoretical framework, new experimental results, and discussions about many physical consequences of the near-field structure. Among them, the presence of spatial antibunching, the observation of extreme localization of twin photons, a link with previous results in second harmonic generation, the observation of correlations that resemble Bessel beams in propagation, and the prediction of fourth-order phase singularities. Section 3.2 contains the theoretical basis of our work, section 3.3 lists the experimental results, and section 3.4 the conclusions and discussion of future perspectives.

## 3.2 Theory

Spatially-entangled photon pairs can be generated by the nonlinear optical process of spontaneous parametric down conversion, where a single pump photon “splits” into two lower-energy photons, which are traditionally called signal and idler. We can think of the crystal as being a thick and extended source of very many elementary “radiators”. The SPDC light behaves as a low-coherence light source as long as the emitted photons are detected individually [40–42]. Most interesting effects are only revealed when one looks at the correlations between the positions of the detected photons.

From the quantum theory of optical coherence and according to the remarks in Chapter 1, the probability of detecting two-fold coincidences is given by  $|A(\mathbf{r}_1, \mathbf{r}_2)|^2$ , where  $\mathbf{r}_i$  is the position of the photon detector  $i = 1, 2$ . The two-photon probability amplitude  $A(\mathbf{r}_1, \mathbf{r}_2)$  is sometimes referred to as the wavefunction of the state. From now on we will restrict ourselves to coincidence detection in a single  $z$ -plane and denote  $A(\boldsymbol{\rho}_1, \boldsymbol{\rho}_2; z)$  as the SPDC probability amplitude. Throughout the Chapter we use a cylindrical coordinate system with the  $z$  axis coinciding with the pump beam axis and with  $\mathbf{r} = (\boldsymbol{\rho}, z)$  being the position vector, with transverse  $\boldsymbol{\rho}$  and longitudinal  $z$  components. A crucial element in our discussion is the assumption that the pump laser is relatively wide as compared to the near-field correlations under study. The two-photon field will then depend

dominantly on the difference coordinate  $\rho_- = \rho_1 - \rho_2$  in the near-field, making  $A(\rho_1, \rho_2; z) \approx V(\rho_-; z)$  (see Sec. 3.2.1 and 3.2.2 for details). The thin-crystal limit consists in approximating  $V(\rho_-; z)$  by a  $\delta$  function. This Chapter discusses specifically how the fine-structure function  $V(\rho_-; z)$  looks like beyond this  $\delta$ -limit.

The near field is usually defined in optics as the field distribution at the source. For a thick (= longitudinally extended) source this concept is ill-defined and, as we will show later, the results depend strongly on which  $z$ -plane of our thick source is imaged. Whatever the imaging geometry, photon pairs emitted from all planes within the crystal will always contribute coherently to the two-photon field in the image plane. Throughout the Chapter we will use the term “near field” to denote the field in a certain  $z$  plane around the image plane of the center of the generating crystal, which we define as  $z = 0$ . In contrast, the far field is defined as the amplitude distribution in a very distant transverse  $z$ -plane. The transition from the near field to the far field can be done by either propagating the generated field or by performing a (fractional) Fourier transformation [43–46].

In the next subsections we will present two different models to calculate the amplitude function  $V(\rho_-; z)$ . The first approach (Sec. 3.2.1) starts from the angular spectrum of the generated field, which is then Fourier transformed to the spatial domain. The detection process is included afterwards. The second approach (Sec. 3.2.2) is formulated directly in spatial coordinates and treats the generation and detection processes on equal footing. While the first approach can be easily compared to results already presented in the literature, the second approach is less common and permits more insight into the nature of the two-photon field. Naturally, both approaches lead to the same predictions.

The main differences between our approach and other equations presented in the literature [47–49] are the following. First, we treat the transverse plane in two dimensions. Assuming a one-dimensional system does lead to loss of generality in our case. Second, we use a generalized “Klyshko picture” in order to account for the non-thin crystal assumption. And third, the detection geometry must be included in the description in order to obtain the correct working equations.

### 3.2.1 Analysis based on the angular spectrum

The momentum representation of the two-photon field generated by SPDC is [19,31]:

$$\tilde{A}(\mathbf{q}_s, \mathbf{q}_i) = \tilde{E}(\mathbf{q}_s + \mathbf{q}_i) \operatorname{sinc}\left(\frac{1}{2}\Delta k_z L\right), \quad (3.1)$$

where  $\tilde{E}(\mathbf{q})$  is the angular spectrum of the pump beam and  $\operatorname{sinc}\left(\frac{1}{2}\Delta k_z L\right)$  is the phase-matching function, with  $\operatorname{sinc}(x) = \sin(x)/x$ , and crystal thickness  $L$ . Phase matching plays a crucial role in all non-linear optical process. The conversion efficiency is maximum if the interacting optical waves retain a fixed phase relation over the full length of the nonlinear crystal. This is expressed mathematically by the dependence of the “sinc” function on the longitudinal wavevector mismatch

$\Delta k_z = k_{p,z} - k_{s,z} - k_{i,z}$ , where the indices refers to the pump ( $p$ ), signal ( $s$ ), and idler ( $i$ ) photons, respectively.

We will concentrate now on our particular case of SPDC emission. We consider noncritical type I phase matching, where all polarizations are equal and all beams propagate close to a principal crystal axis in a periodically-poled crystal. These crystals offer the advantage of having a high conversion efficiency, when compared to bulk crystals. Additionally, the photon pairs do not suffer Poyinting vector walk-off. With regard to the generated wavefunction, i.e., the spatial correlations, SPDC light produced in a periodically-poled crystal behave exactly the same as in a bulk crystal [27, 50]. A second-order Taylor expansion of the quasi wave-vector mismatch  $\Delta k_z$  in the considered geometry yields [51]

$$\frac{1}{2}\Delta k_z L \approx \frac{L}{8nk_0} \left[ |\mathbf{q}_s - \mathbf{q}_i|^2 + \left( \frac{n_p - n}{n_p} \right) |\mathbf{q}_s + \mathbf{q}_i|^2 \right] + \varphi(T, \Omega), \quad (3.2)$$

where  $k_0 = 2\pi/\lambda_0$  is the vacuum wave vector of the generated light,  $n_p$  and  $n$  are the refractive indices at the pump and generated wavelength, respectively, and  $\mathbf{q}_{s,i}$  are the transverse components of the signal and idler wavevectors  $\mathbf{k}_{s,i}$ ; the angular dependence of  $n_p$  and  $n$  has been neglected. In our further analysis we will neglect the minor dependence of the phase mismatch on the sum momentum because (i) typically the ratio  $(n_p - n)/n_p \ll 1$ , being 0.058 for our periodically-poled KTP, and (ii) the spread in the sum momentum  $\mathbf{q}_s + \mathbf{q}_i$ , as set by the pump divergence, is generally much smaller than the spread in the difference momentum  $\mathbf{q}_s - \mathbf{q}_i$ , anyhow.

Under the conditions stated above, the angular spectrum of the generated two-photon field thus factorizes in the special form [19, 36]

$$\tilde{A}(\mathbf{q}_s, \mathbf{q}_i) = \tilde{E}_p(\mathbf{q}_s + \mathbf{q}_i) \tilde{V}(\mathbf{q}_s - \mathbf{q}_i), \quad (3.3)$$

where the phase-matching function  $\tilde{V}(\mathbf{q}_s - \mathbf{q}_i) = \text{sinc}(\frac{1}{2}\Delta k_z L)$  depends only on the difference momentum. This function also contains the collinear phase mismatch  $\varphi$  as an adjustable parameter that depends on the crystal temperature  $T$  and a possible frequency detuning  $\Omega \ll \omega_0$  from frequency degeneracy as [27]

$$\varphi(T, \Omega) = \alpha(T - T_0) - \beta\Omega^2. \quad (3.4)$$

The two-photon field in real-space coordinates  $A(\boldsymbol{\rho}_s, \boldsymbol{\rho}_i; z)$  can be obtained from a Fourier transformation that links the transverse momentum  $\mathbf{q}$  with the transverse position  $\boldsymbol{\rho}$  for both signal and idler photons. Based on Eq. (3.3), it is straightforward to show that the spatial representation of the two-photon field can also be factorized as

$$A(\boldsymbol{\rho}_s, \boldsymbol{\rho}_i; z) = E_p(\boldsymbol{\rho}_+; z) V(\boldsymbol{\rho}_-; z). \quad (3.5)$$

The factor  $E_p(\boldsymbol{\rho}_+; z)$  quantifies the well-known observation that the two-photon field retains a ‘‘copy of the pump profile’’ [19] in its dependence on the average

coordinate  $\boldsymbol{\rho}_+ \equiv \frac{1}{2}(\boldsymbol{\rho}_s + \boldsymbol{\rho}_i)$ . The factor  $V(\boldsymbol{\rho}_-; z)$  quantifies the fine structure in the two-photon field via its dependence on the difference coordinate  $\boldsymbol{\rho}_- \equiv (\boldsymbol{\rho}_s - \boldsymbol{\rho}_i)$ . Note that Eq. (3.5) describes the total two-photon field as observed around an image plane of the generating crystal. In the  $z = 0$  image plane, associated with the center of the crystal, Eq. (3.3) contains no extra phase factors. For points in the vicinity of this plane (at  $z \neq 0$ ) the angular spectrum must be multiplied by the free space propagator  $\exp[-i|\mathbf{q}|^2 z / (2k)]$  for both the signal and idler photons.

Experimentally, the fine structure described by the function  $V(\boldsymbol{\rho}_-, z)$  can be most easily observed if it exists on a scale much smaller than the pump profile, making  $A(\boldsymbol{\rho}_s, \boldsymbol{\rho}_i; z) = E_p(\boldsymbol{\rho}_+; z)V(\boldsymbol{\rho}_-; z) \approx V(\boldsymbol{\rho}_-; z)$ . This condition is satisfied in the near field if the pump laser is sufficiently well collimated, i.e., if the Rayleigh range of the pump laser is much larger than the thickness of the crystal. Based on Eqs. (3.1) and (3.2) we write  $\tilde{V}(\mathbf{q}_s - \mathbf{q}_i) = \text{sinc}[(L/8nk_0)|\mathbf{q}_s - \mathbf{q}_i|^2 + \varphi]$ , which after Fourier transformation yields

$$V(\boldsymbol{\rho}_-; z) \propto \int_{-\infty}^{+\infty} d\mathbf{q} \text{sinc}\left(\frac{L|\mathbf{q}|^2}{2nk_0} + \varphi\right) \exp\left[-i\frac{|\mathbf{q}|^2}{k_0}z - i\mathbf{q} \cdot \boldsymbol{\rho}_-\right]. \quad (3.6)$$

We experimentally measure the fine structure in the generated two-photon field with two photon counting modules that are coupled to moveable single-mode fibers. Mathematically, this detection geometry is described by a projection of the two-photon amplitude onto the mode profiles of the two detectors. This yields the projected amplitude

$$V_{\text{proj}}(\boldsymbol{\rho}_s - \boldsymbol{\rho}_i; z) \propto \iint_{-\infty}^{+\infty} d\boldsymbol{\rho}'_s d\boldsymbol{\rho}'_i V(\boldsymbol{\rho}'_s - \boldsymbol{\rho}'_i; z) \phi_s^*(\boldsymbol{\rho}'_s - \boldsymbol{\rho}_s; z) \phi_i^*(\boldsymbol{\rho}'_i - \boldsymbol{\rho}_i; z), \quad (3.7)$$

where  $\phi_j(\boldsymbol{\rho}_j; z)$  is the mode profile of either detector mode ( $j = \{s, i\}$ ) and  $\boldsymbol{\rho}_j$  is now the adjustable displacement of this detector. The integration over the transverse coordinates can be taken in any  $z$  plane because the propagation of the two-photon field is described by the product of the same single-mode propagators that determine the propagation of the detector modes. The coincidence count rate  $R_{cc} \propto |V_{\text{proj}}(\boldsymbol{\rho}_s - \boldsymbol{\rho}_i; z)|^2$ . This function is rotationally symmetric, as it depends only on  $|\boldsymbol{\rho}_s - \boldsymbol{\rho}_i|$ , and possesses mirror symmetry with respect to the  $z = 0$  plane, since  $V_{\text{proj}}(\boldsymbol{\rho}_-; z) = V_{\text{proj}}^*(\boldsymbol{\rho}_-; -z)$ . Further simplifications of Eq. (3.7) will be provided in the Appendix 3.A, which includes an analytical expression for the on-axis correlations at perfect phase matching ( $\varphi = 0$ ).

Although the above discussion started from noncritical type I phase matching conditions, it also applies to general type I phase matching, where the beams are not necessarily aligned with the crystal axes, and even works partially for general type II phase matching. The argument goes as follows. For any type of phase

matching, we can always rewrite the general Eq. (3.1) in the form

$$\tilde{A}(\mathbf{q}_s, \mathbf{q}_i) = \tilde{E}(\mathbf{q}_s + \mathbf{q}_i) \hat{V}(\mathbf{q}_s + \mathbf{q}_i, \mathbf{q}_s - \mathbf{q}_i), \quad (3.8)$$

where the new phase-matching function  $\hat{V}$  now depends both on the sum and difference coordinate. As essential ingredient, we again assume that the pump profile is sufficiently wide in real space in order to make  $\tilde{E}(\mathbf{q}_s + \mathbf{q}_i)$  compact enough in momentum space to dominate over a possible dependence of  $\hat{V}$  on  $\mathbf{q}_s + \mathbf{q}_i$ . This allows us to approximate  $\tilde{A}(\mathbf{q}_s, \mathbf{q}_i) \approx \hat{V}(\mathbf{0}, \mathbf{q}_s - \mathbf{q}_i) \equiv \tilde{V}(\mathbf{q}_s - \mathbf{q}_i)$ , although the precise expression for  $\tilde{V}$  depends on the type of phase matching (see Appendix of ref. [52]). For general type I phase matching we again obtain  $\tilde{V}(\mathbf{q}_s - \mathbf{q}_i) = \text{sinc} [(L/8nk_0)|\mathbf{q}_s - \mathbf{q}_i|^2 + \varphi]$ , but the assumption “sufficiently wide pump”, now also requires that the pump beam is wider than the transverse walk-off between the pump beam and SPDC beams. For type II SPDC, the walk-off between the (orthogonally-polarized) signal and idler photons introduces an extra linear form in the phase-matching function, which now becomes  $\tilde{V}(\mathbf{q}_s - \mathbf{q}_i) = \text{sinc} [(L/8nk_0)|\mathbf{q}_s - \mathbf{q}_i|^2 + \gamma(q_{s,y} - q_{i,y}) + \varphi]$ . After Fourier transformation, the spatial correlation observable in the fine structure function  $V(\boldsymbol{\rho}_-; z)$  are found to have lost their rotation symmetry; the correlations in the  $x$  direction, i.e, orthogonal to the walk-off direction, are as before but the correlations in the  $y$  direction are naturally modified by the transverse walk-off in that direction.

### 3.2.2 Analysis based on volume integral over detection modes

In this subsection we will present an alternative approach to calculate the projected field  $A_{\text{project}}(\boldsymbol{\rho}_s, \boldsymbol{\rho}_i; z)$  directly in real space, without the detour via its angular spectrum. This approach is based on a three-dimensional integration over the production sites of photon pairs within the generating crystal.

In SPDC, the probability amplitude for the pump photon to split into two lower-energy photons is proportional to the complex electric field at the generating site. As the photon pairs are always emitted “from the same point”, one can write [53]

$$A_{\text{source}}(\mathbf{r}'_s, \mathbf{r}'_i) \propto E_p(\mathbf{r}'_s) \delta(\mathbf{r}'_s - \mathbf{r}'_i) \quad (3.9)$$

where  $E_p(\mathbf{r}'_s)$  is the electric field profile of the pump beam. The probability amplitude of finding two photons at positions  $\mathbf{r}_s$  and  $\mathbf{r}_i$  outside the crystal is obtained by summation over all possible generating sites and propagation to the observation points. This leads to the following integral:

$$A_{\text{gen}}(\boldsymbol{\rho}_s, \boldsymbol{\rho}_i; z) = \int_{\text{crystal}} d\boldsymbol{\rho}' dz' E_p(\boldsymbol{\rho}', z') h(\boldsymbol{\rho}_s, z; \boldsymbol{\rho}', z') h(\boldsymbol{\rho}_i, z; \boldsymbol{\rho}', z'), \quad (3.10)$$

where  $h(\boldsymbol{\rho}, z; \boldsymbol{\rho}', z')$  is the Green function that describes the propagation of the field from the plane  $z$  to the plane  $z'$ . Equation (3.10) can be considered as a generalization of the result presented in Ref. [53], the major difference being the

inclusion of the  $z$  integration to account for the finite crystal thickness. Since our crystal is a longitudinally extended source and the propagators  $h(\boldsymbol{\rho}, z; \boldsymbol{\rho}', z')$  links the field between any two planes, Eq. (3.10) basically integrates the contributions of all different generating planes to the observation plane. This generalization is sufficient to explain *all* results presented in this Chapter.

In our experimental scheme the down-converted beams are detected by single-mode optical fibers. One can then use both propagators  $h$  to propagate the well-defined detection modes *back* to the crystal, instead of using the *forward* propagation of the generated two-photon field towards the detectors. We will denominate this point of view as the “double Klyshko picture”, in analogy with the Klyshko picture of SPDC where only one beam is propagated backwards from the detector to the generating crystal, where it is effectively “reflected” towards the other detector. The double Klyshko picture considerably simplifies the description, since the Gaussian profiles of the detection modes can be easily propagated.

For a crystal of thickness  $L$  in the  $z$  direction and infinite width in the transverse directions we may thus write the projected two-photon field as

$$A_{\text{proj}}(\boldsymbol{\rho}_s, \boldsymbol{\rho}_i; z) \propto \int_{-L/2}^{+L/2} dz' \int_{-\infty}^{+\infty} d\boldsymbol{\rho}' E_p(\boldsymbol{\rho}'; z') \phi_s^*(\boldsymbol{\rho}' - \boldsymbol{\rho}_s; z' - z) \phi_i^*(\boldsymbol{\rho}' - \boldsymbol{\rho}_i; z' - z), \quad (3.11)$$

where  $\boldsymbol{\rho}_s$  and  $\boldsymbol{\rho}_i$  again denote the transverse displacement of the detection modes. In the “double Klyshko picture” we can also consider  $z$  as the position of the detection modes foci *inside the crystal*, as shown in the inset of Fig. 3.1. The mode profile of each fundamental Gaussian detecting modes is

$$\begin{aligned} \phi(\boldsymbol{\rho}; z) &\propto \frac{\exp(ikz)}{z - iz_n} \exp\left(i \frac{k|\boldsymbol{\rho}|^2}{2(z - iz_n)}\right) = \\ &= \frac{\exp(i[kz - \phi_{\text{Gouy}}(z)])}{\sqrt{z^2 + z_n^2}} \exp\left(-\frac{|\boldsymbol{\rho}|^2}{w(z)^2}\right) \exp\left(i \frac{k|\boldsymbol{\rho}|^2}{2R(z)}\right), \end{aligned} \quad (3.12)$$

where  $z_n = \frac{1}{2}nk_0w_d^2$  is the Rayleigh range,  $\phi_{\text{Gouy}}(z) = \arctan(z/z_n)$  is the Gouy phase,  $w(z) = w_d\sqrt{1 + z^2/z_n^2}$  is the beam diameter, and  $R(z) = z + z_n^2/z$  is the radius of curvature of the detection mode. Upon entering a dielectric medium, the Gaussian detection mode retains its waist  $w_d$  but is stretched in the longitudinal direction; this effect has been accounted for by introducing  $z_n$  and  $k = nk_0$ .

Finally, we substitute the mode profiles of Eq. (3.12) in Eq. (3.11) and consider a very wide pump beam. A Gaussian integration over the transverse coordinates allows us to express the projected field in terms of a single integral over the

thickness of the crystal

$$V_{\text{proj}}(\boldsymbol{\rho}_s - \boldsymbol{\rho}_i; z) \propto \int_{-L/2-nz}^{+L/2-nz} dz' \frac{\exp(-i\Delta k_z^0 z')}{z' - iz_n} \exp\left(\frac{ik}{z' - iz_n} \frac{|\boldsymbol{\rho}_s - \boldsymbol{\rho}_i|^2}{4}\right), \quad (3.13)$$

where  $\Delta k_z^0$  is the on-axis phase mismatch ( $\mathbf{q}_s = \mathbf{q}_i = 0$ ). If we use compact detection modes, the projected two-photon field in Eq. (3.13) will closely resemble the generated field. It should be stressed, however, that both fields contain contribution from all points inside the crystal. The main result in this section, in the form of Eq. (3.13), is mathematically equivalent to Eq. (3.7), despite their differing functional forms. One can use either one to calculate the theoretical fine structure; the answers should be the same. The explicit equivalence between the two approaches is presented in Appendix 3.B.

### 3.3 Experiment

#### 3.3.1 Experimental setup

The experimental setup used for our experiments is depicted in Fig. 3.1. We aim at obtaining high resolution images of the near-field correlations present in the two-photon field. This is realized experimentally by using two tightly-focused detection modes that can be laterally displaced with respect to each other and by mounting the crystal on a translation stage that permits adjusting its longitudinal position. In the inset of Fig. 3.1 we illustrate how the back-propagated Gaussian detection modes look like if focused in a certain plane inside the crystal. The waist width  $w_d = 7 \mu\text{m}$  was chosen to provide an optimal tradeoff between the desired resolution and detection efficiency.

The idea behind this setup is similar to the strategy used in confocal microscopy or two-photon microscopy [54], namely, to eliminate most of the out-of-focus light in order to achieve high lateral and longitudinal resolution. The major difference is that the incoherent nature of the confocal imaging assures that mostly one plane is visualized. In our case both the generation and detection process are coherent, which means that there is a precise phase relationship between light emitted from all different planes. This leads to interesting fourth-order interference effects, to be described below.

Spatially entangled photon pairs are generated by pumping a 5.06-mm-thick periodically-poled  $\text{KTiOPO}_4$  crystal (PPKTP) with a 180-mW krypton-ion laser beam operating at 413.1 nm. The crystal is positioned close to the focus of a  $f=50$  mm lens and is mounted on a translation stage. The laser beam is blocked by a coated GaP wafer, while the down-converted photons are transmitted and then separated by a beam splitter. The detection stages comprise objective lenses and computer-controlled actuators that permit positioning and scanning the detectors in the transverse plane. Single counts are registered by two single photon counting modules; coincidence counts are obtained from a fast AND gate with a

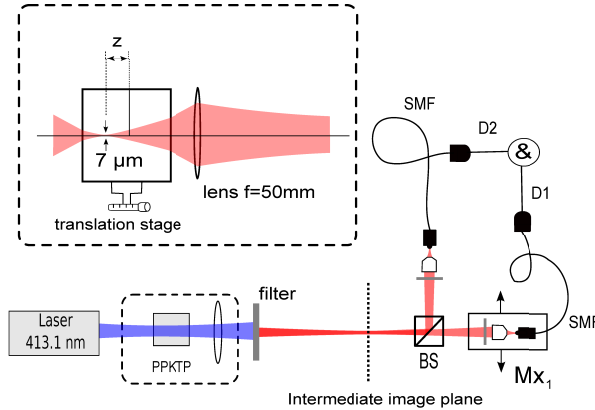


Figure 3.1: Experimental setup for observing the near-field correlations in the two-photon field. A PPKTP crystal is pumped by a laser beam operating at 413.1 nm, generating photon pairs by SPDC. A  $f=50$  mm lens creates a  $13\times$  magnified image of the near-field in a intermediate plane. The two-photon field is then separated at a beam splitter, projected onto two single-mode optical fibers by objective lenses, and detected by photon counters and coincidence electronics. Interference filters are used to block the pump wavelength after the crystal and to select photons close to frequency degeneracy in front of the detectors (spectral width 5 nm at 826 nm). The transverse correlations within the photon pairs are measured by moving detector 1 horizontally; the longitudinal correlations are obtained by adjusting the crystal  $z$  position with a translation stage. The inset shows how the detection modes would behave inside the crystal if back-propagated through the imaging system. The detection waist of  $7\ \mu\text{m}$  was chosen to provide an optimal tradeoff between resolution and detection efficiency.

time window of 1.4 ns. Narrow band interference filters (spectral width 5 nm at 826 nm) placed in front of the detectors assure “quasi-monochromatic” operation.

The effect of the on-axis phase mismatch  $\varphi$  is investigated by setting the temperature of the crystal. Based on the temperature dependence of the refractive indexes at the pump and SPDC wavelengths, the derivative  $d\varphi/dT \approx 1.04\ \text{K}^{-1}$  was calculated and checked experimentally [27].

The imaging system is set up as follows. The focusing lens of  $f = 50$  mm produces a  $M = 13\times$  magnification of the SPDC generated light onto an intermediate image plane. The two objective lenses ( $f=11$  mm) then image desired regions of the intermediate image plane onto the input tips of two optical fibers with a demagnification factor of  $1/28\times$ . In order to adjust the proper width of the detection modes we back-propagate a diode laser, operating at the same wavelength of the down-converted modes, through the same single-mode optical fibers used for detection. Adjusting the position of the objective lenses we minimize the detection modes width at the image plane to  $(w_d)_{\text{image}} = 85\ \mu\text{m}$ , as checked with a beam profiler CCD camera. This corresponds to  $w_d \approx 7\ \mu\text{m}$  inside the crystal.

The spatial reconstruction of the fourth-order correlation function  $V_{\text{proj}}(\rho_-; z)$

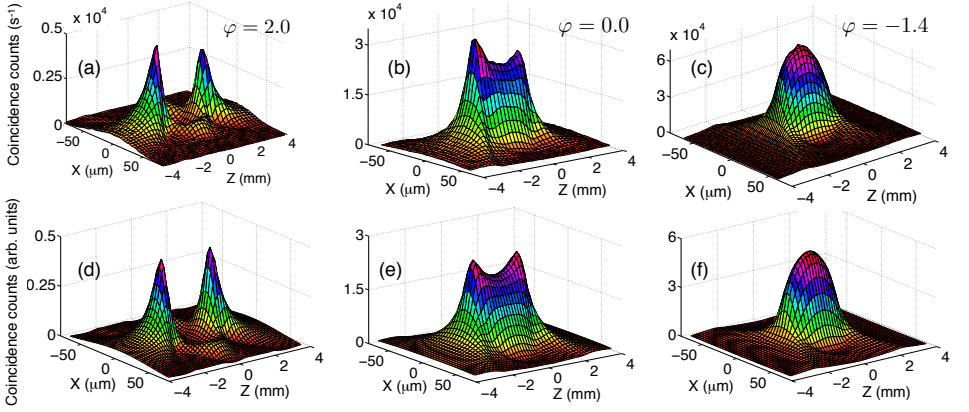


Figure 3.2: Full spatial dependence of the near-field correlations for different phase-mismatches. Figures (a), (b), and (c) show the experimental results for  $\varphi = 2.0$ ,  $\varphi = 0.0$ , and  $\varphi = -1.4$ , respectively. Figures (d), (e), and (f) show the theoretical results, calculated using either Eq. (3.13) or Eq. (3.17). The relative strength (=vertical scale) between the three experimental and the three theoretical plots is determined by a single scaling parameter.

is obtained by combining a longitudinal translation of the crystal with transverse scans of the detection stages. By moving the nonlinear crystal towards or away from the lens we can image different slices in the vicinity of the crystal. For each imaged plane we measure the transverse dependence of the coincidence count rate by fixing one detector mode centered at  $\rho = \mathbf{0}$  and scanning the other one in the horizontal direction. Since the near-field correlations depend only on the difference coordinate  $|\rho_s - \rho_i|$ , we are effectively reconstructing  $V_{\text{proj}}(\rho_-; z)$ . Two remarks are important: due to the magnification factor, moving one detector stage by  $M\rho$  causes the detection mode inside the crystal to move by  $\rho$ , as sketched in Fig. 3.1. Furthermore, refractive effects stretch the Gaussian detection mode longitudinally; therefore, in order to move the focus from the front facet to the back facet, the crystal needs to be displaced only by a distant  $L/n$ . All the presented experimental data are scaled to account for both magnification and refractive effects, i.e., the transverse displacement of the detector stage has been divided by  $M = 13\times$  and the longitudinal displacement of the crystal has been multiplied by  $n$  ( $n = 1.843$  for PPKTP at 826.2 nm and  $T \approx 60^\circ\text{C}$ ). All count rates are corrected for accidental counts.

### 3.3.2 Results and discussion

Our goal is to verify experimentally the main features present in the near-field correlations of the two-photon field, including the full spatial dependence in both transverse and longitudinal coordinates as well as the behavior under phase mismatch. We can calculate the theoretical predictions either from Eq. (3.13) or Eq. (3.17) presented in the Appendix 3.B.

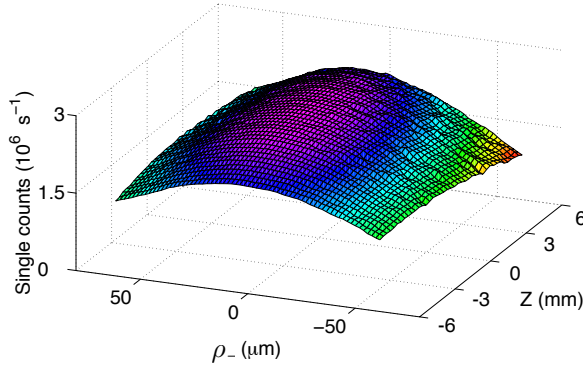


Figure 3.3: Single counts recorded by the scanning detector while obtaining the correlations in Fig. 3.2(b). The intensity varies less than 10% in the central region of the scan ( $\rho_- < 25 \mu\text{m}$ ). The small residual variations are due to the finite width of the pump beam.

Figure 3.2 gives an overview of three complete characterizations. The experimental results for  $\varphi = 2.0$ ,  $\varphi = 0.0$ , and  $\varphi = -1.4$  are displayed in Figs. 3.2(a), 3.2(b), and 3.2(c) respectively. Figs. 3.2(d), 3.2(e), and 3.2(f) show the corresponding theoretical predictions. Note that the theoretical curves do not contain any fit parameters, being based only on well-known parameters, such as  $L$ ,  $k_0$ ,  $w_d$ , and  $\varphi$ . The qualitative agreement between theory and experiments is evident. The theoretical coincidence counts are displayed in arbitrary units, since the theory only provides a proportionality; the fact that the proportionality factor is  $\approx 10^4$  is just a coincidence. The relative scaling between plots taken at different temperatures is well defined and agrees with the experimental data.

The obtained three-dimensional results are intriguing. For  $\varphi = 2.0$  we observe the presence of two very sharp peaks with a low “crater” in between. The distance between the two peaks in the experimental data is  $(5.3 \pm 0.1)$  mm, while theory predicts a value equal to  $L = 5.06$  mm. Even for perfect phase-matching ( $\varphi = 0$ ), we observe considerably higher counts when the detection modes are focused at either of the crystal facets. The observation of this “surface effect” is limited to observations with compact detection modes ( $w_d \approx 7 \mu\text{m}$  in our setup). For a detection mode width of  $w_d = 10 \mu\text{m}$  the peaks should be hardly visible, being absent for  $w_d = 12 \mu\text{m}$  (and  $\varphi = 0$ ). The effect of the increased detection mode width is to smooth the detected fine structure  $V_{\text{proj}}(\rho_-; z)$ .

We can interpret these results as follows. Suppose we had a non-magnified imaging scheme ( $M = 1$ ). The plane  $z = 2.5$  mm corresponds to an image of the output facet of the crystal and can indeed be interpreted as a “copy” of the field in that position. Although the measured correlations in the other planes ( $z < 2.5$  mm) exist in the vicinity of the image plane, they can no longer be interpreted as an image of the field correlations inside the crystal. The reason is that if one tries to image regions inside the source, light emitted between these regions and the output facet will also contribute, albeit in a “defocused” way.

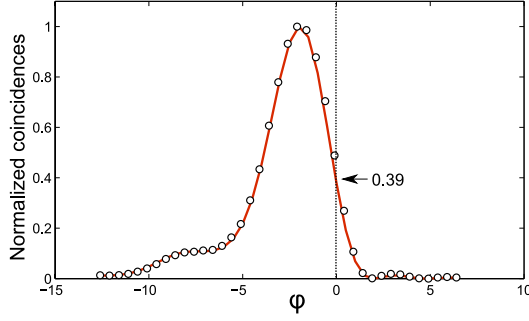


Figure 3.4: Dependence of the coincidence count rate on the phase mismatch  $\varphi$ . When both detection modes are centered ( $\rho_s = \rho_i = \mathbf{0}$ ) and focused at the center of the crystal ( $z = 0$ ). The phase mismatch can be adjusted by changing the temperature of the crystal. The open circles are experimental; the continuous curve the theoretical result. No curve fitting was performed. The asymmetry of the curve depends sensitively on the width of the detection mode (see text). For our experimental realization, the coincidence count rate at  $\varphi = 0.0$  is only 39% of its maximum value, which is achieved at  $\varphi = -2.0$ .

With our measurement we can only describe how the correlations behave in the accessible region around the image plane.

All the peculiar structures shown in Fig. 3.2 are only present in the fourth-order correlation (=coincidences counts) as no interference effect is observed in the single counts. We confirm this statement by plotting in Fig. 3.3 the single counts measured by the scanning detector for  $\varphi = 0$  (perfect phase matching). The single counts behave in the same way for all  $\varphi$  values considered in this work. In the remaining Figs. 3.4-3.9 we will discuss in details some specific features of the near-field correlations.

Figure 3.4 shows how the coincidence rate  $|V_{\text{proj}}(\mathbf{0}; 0)|^2$ , recorded on axis ( $\rho_- = \mathbf{0}$ ) and at  $z = 0$ , varies with phase matching. This figure thus shows the relative scaling between the scans performed at different phase mismatches. Note that Fig. 3.4 is not symmetric with respect to  $\varphi = 0$  and peaks at  $\varphi = -2.0$  rather than at  $\varphi = 0.0$ . Equation (3.13) predicts that the asymmetry of the curve is basically determined by the size of the detection modes. In the limit  $w_d \rightarrow 0$  (or  $z_n \rightarrow 0$ ) the theoretical curve is highly asymmetric, while the curve becomes approximately symmetric under  $\varphi \leftrightarrow -\varphi$  for large  $w_d$ , when the Rayleigh range  $z_n = \frac{1}{2}kw_d^2$  of the detection modes becomes much larger than the crystal thickness. This can be understood physically by noticing that for a very large detection width all the down-converted light is collected; one then effectively measures the overall SPDC efficiency as a function of the phase mismatch, recovering the standard “sinc” curve.

Figure 3.5 shows the dependence of the on-axis  $\rho_- = \mathbf{0}$  coincidence rate on the longitudinal position  $z$  of the detection foci. The experimental  $z$ -scans of  $|V_{\text{proj}}(\mathbf{0}; z)|^2$  are measured for  $\varphi = 2.0$ ,  $\varphi = -1.4$ ,  $\varphi = -8.7$ , and  $\varphi = -11.0$ .

All results are in accord with our expectations (not shown) apart from a small asymmetry in the signal observed when the detected foci are positioned either at the facet closest to the lens ( $z = -L/2$ ) or at the far facet ( $z = +L/2$ ). We attribute the observed asymmetry to spherical aberration in the focused detection modes, induced by their transition through the air-crystal interface; this aberration would make the waist of the detector modes somewhat larger when it is positioned at the far facet as compared to the near facet of the generating crystal.

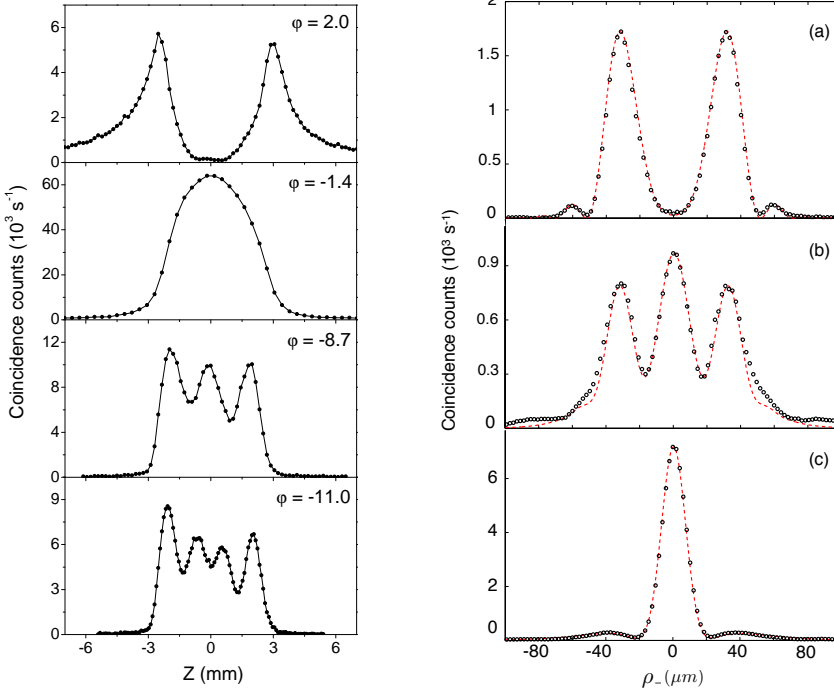
Figure 3.5 shows that the phase mismatch has a dramatic effect on the axial correlations. The range within which the coincidence counts are appreciable is bounded by the crystal thickness  $L = 5.06$  mm, but its precise shape follows from Eq. (3.13), which for  $\rho_- = \mathbf{0}$  translates into

$$|V_{\text{proj}}(\mathbf{0}; z)|^2 \propto \left| \int_{-L/2-z}^{+L/2-z} dz' \frac{\exp(-i\Delta k_z z')}{(z' - iz_n)} \right|^2. \quad (3.14)$$

Equation (3.14) is identical to a classical formula [55] for the intensity of second harmonic generation (SHG) in a medium pumped by a tightly focused Gaussian beam. The shapes presented in Fig. 3.5 are indeed similar to those obtained in the context of SHG [55, 56]. We have thus shown that the strong dependence of the longitudinal ( $z$ ) correlations with phase-mismatch is also present in the two-photon correlation measurements in SPDC. Theoretical studies for axial correlations have been performed before by Nasr et al. [48]. They also concluded that strong axial correlations are only found in a region around the image plane bounded by the thickness of the crystal  $L$  (divided by the refractive index). However, their exact predictions differs from ours due to an assumption that the system could be treated in only one dimension. This point is further discussed in Appendix 3.A, where we also obtain an analytical expression for the axial correlations at perfect phase matching.

Figure 3.6 shows the transverse correlations at  $\varphi = -2.0$  as measured and calculated for three different  $z$ -planes: (a)  $z_a = 0$ , (b)  $z_b = 0.3 \times L/2$ , and (c)  $z_c = L/2$ . That is, the detection modes are focused at the center of the crystal, at an intermediate plane, and at the facet, respectively. These curves are examples of how we can find a rich set of non-bell shaped transverse correlations in the near field that are not yet discussed in the literature. Notice how the transverse profile of the coincidence rate changes with the focusing plane. If one focus the detection modes at either crystal surface there is a maximum probability of finding the two photons “together” at  $\rho = \mathbf{0}$ . If the detection modes are focused in the center ( $z = 0$ ), this probability drops to practically zero, i.e., the two photons are spatially antibunched [57, 58]. This observation of antibunching is sufficient to reveal the quantum nature of the correlations (as long as the field is also homogeneous, which is the case). We have discussed this aspect in [39].

We can also interpret Fig. 3.6 imagining, once again, a scheme with unit magnification. There is a plane before  $z < 0$  where the photon pairs are found



LEFT: Figure 3.5. Axial correlations ( $\rho_s = \rho_i = 0$ ) in the near field for different phase mismatches  $\varphi$ . This figure demonstrates the intriguing dependence of the measured on-axis correlations on the focusing plane  $z$ .

RIGHT: Figure 3.6. Transverse correlations for  $\varphi = 2.0$  in three different  $z$ -planes. These plots correspond to transverse cuts of Fig. 3.2(a) taken at the planes (a)  $z_a = 0$ , (b)  $z_b = 0.3 \times L/2$ , and (c)  $z_c = L/2$ . The open circles are experimental data; the dashed curves are the theoretical predictions. Fig. (a) exhibits spatial antibunching (see text).

predominantly together in the same transverse position. In the plane  $z = 0$  this situation is reversed, and the photons are antibunched, i.e., there is a zero probability of finding them at the same position. The symmetry  $z \leftrightarrow -z$  assures that for  $z > 0$  the photons will be once again bunched. The transition of an axial valley to an axial peak in near-field imaging also appears in the context of Fresnel diffraction. It is solely due to free space propagation of the field. The two-photon field propagate in a similar fashion, but instead of a zero in intensity there is a zero in coincidences counts.

Figure 3.7 shows how the central peak for transverse correlations can get very narrow in certain configurations. We show the results obtained for a transverse scan at  $z = 0$  and  $\varphi = -8.2$ . The full width at half maximum (FWHM) of this peak is only  $10 \mu\text{m}$  as indicated. Quite surprisingly, this narrow width

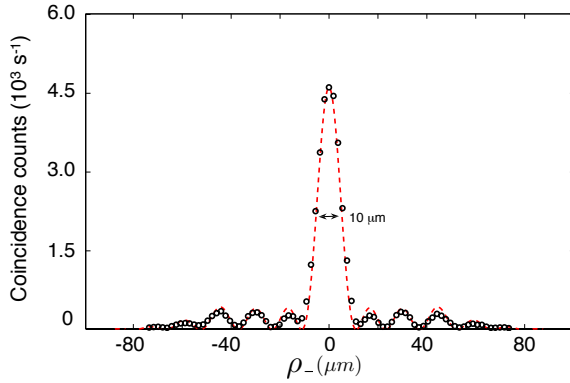


Figure 3.7: Transverse correlations for  $\varphi = -8.2$  and  $z = 0$ . This curve demonstrates that it is possible to achieve very narrow central peaks by adjusting the phase mismatch  $\varphi$ ; the central peak has a FWHM of only  $10 \mu\text{m}$ .

can maintain itself without being diffracted over a  $z$ -range as long as the crystal thickness  $L$ . To stress this point we show in Fig. 3.8 a false color plot of the measured fourth-order correlation over the full  $z$  range. The white dashed curves indicate how a Gaussian beam with the same FWHM at its waist would diffract; the Rayleigh range of this beam is  $z_0 = 274 \mu\text{m}$  at  $\lambda = 826.2 \text{ nm}$ . We can see that the fourth-order correlation pattern retains its narrow width for much longer than the corresponding Gaussian beam. These correlations are also less “diffractive” as compared to a Gaussian beam with the de Broglie wavelength of the biphoton  $\lambda/2 = 413.1 \text{ nm}$ . This behavior is a consequence of the many side peaks that can be clearly identified. In this respect, it resembles the propagation characteristics of Bessel-like beams.

Recently, the possibility of achieving extreme biphoton spatial localization in the near field by resolving the photon pairs temporally, and vice versa, was theoretically proposed [59]. Figure 3.7 experimentally proves that high spatial localization can also be achieved by controlling the phase matching conditions. For thinner crystals and smaller values of  $\varphi$ , peaks as narrow as  $4 \mu\text{m}$  can be produced.

Next we compare the narrow-ranged correlations discussed above with those obtained at the most common experimental setting  $\varphi = 0$  (perfect phase matching). Figure 3.9(a) shows the experimental and theoretical results for a transverse scan at  $z = 0$ . A  $20\times$  magnified plot is also shown in order to highlight the superiority of the correct theoretical expression over gaussian approximations. The FWHM of this curve is  $32 \mu\text{m}$ , thus being about  $3\times$  larger than the curve taken at  $\varphi = -8.2$ . and presented in Fig. 3.7.

Our theoretical formulation also provides the phase structure of the “wave-function” in the near field. Figure 3.9(b) shows a density plot of the theoretical

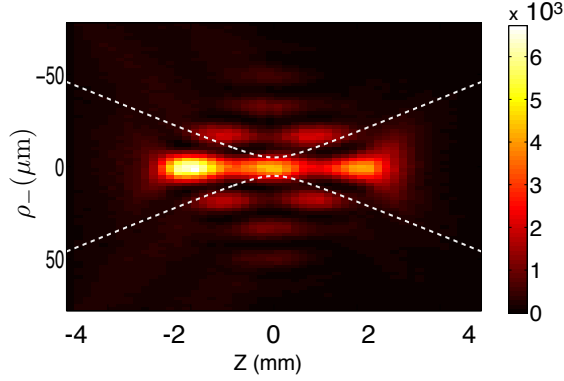


Figure 3.8: Density plot of the fourth-order correlation for a full spatial scan performed at  $\varphi = -8.2$ . The curve shown in Fig. 3.7 retains its width over a relatively long  $z$  range, much longer than if it were a Gaussian beam. The white dashed curve shows how a Gaussian beam with the same waist (FWHM=10  $\mu\text{m}$ ) would diffract; at  $\lambda = 826.2 \text{ nm}$  the Rayleigh range of this beam is  $z_0 = 274 \mu\text{m}$ . The persistence of the narrow structure in the measured coincidence rate is maintained by interference with light from the many side peaks; a similar phenomenon occurs in a Bessel beam.

phase surfaces obtained directly from the complex-valued amplitude  $V_{\text{proj}}(\rho_-; z)$ . The phase is unwrapped in such a way that all phase jumps are related to phase singularities. These phase singularities are associated with the points where we expect a zero for the two-photon correlation. These singularities are thus not of the standard type, related to zeros of field intensities, but are related to zeros of the fourth-order correlation function. It has been shown recently that an optical vortex can be transferred from the pump beam to the biphoton correlation [60]. Here we argue that those “fourth-order phase singularities” also arise due to phase-matching.

A word of caution. Some authors consider the near-field imaging as an imaging of the *birthplace* of the photon pairs [25]. As we have seen, this statement is not very accurate. The physical origin of the observed correlations is always interference of photon pairs generated at all possible sites in the crystal. There is a coherent superposition of localized emissions from all these sites. The combined effect of all production events, propagated to the observation plane, leads to the measured fourth-order interference patterns. The collinear phase mismatch  $\varphi$  is a crucial component in the description since it changes the relative phase of photon pairs generated at different “slices” in the crystal. This strongly modifies the propagation and, therefore, the resulting interference. The presence in Fig. 3.2 of either photon bunching or antibunching, which is not in contradiction with the assumption of (a superposition of) localized emissions, illustrates very well the point.

Finally we would like to discuss the implications of our results to measure-

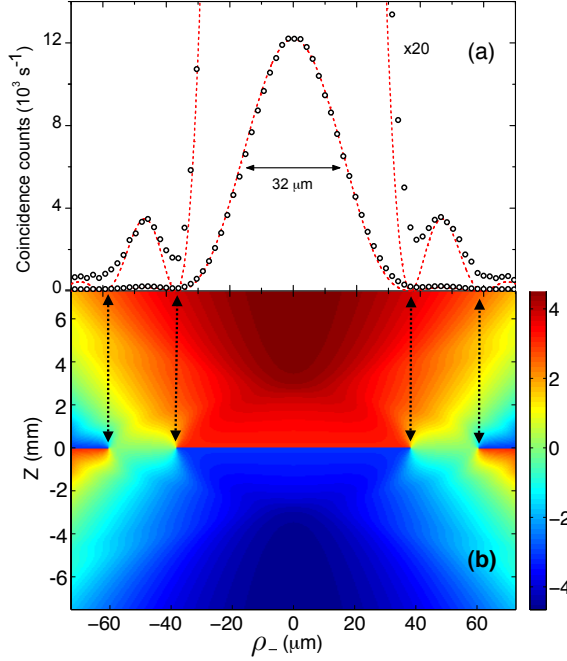


Figure 3.9: (a) Transverse correlations at perfect phase-matching ( $\varphi = 0.0$ ) and  $z = 0$ . The open circles are experimental data; the dashed line is a theoretical prediction. The FWHM of both experimental and theoretical curves is  $32 \mu\text{m}$ . In the  $20\times$  magnified plot small side peaks are visible. (b) False-color plot of the theoretical phase surfaces obtained from the complex valued amplitude  $V_{\text{proj}}(\rho_-; z)$ . The arrows indicate the presence of fourth-order phase singularities at the points where the correlation function is zero valued.

ments of the dimensionality of the spatial entanglement. Recently Howell *et al.* proposed and implemented a realization of the Einstein-Podolsky-Rosen (EPR) paradox, i.e., the violation of a separability criterion in the position-momentum domain, using entangled photon pairs [25]. One of their key measurements is similar to the one presented in Fig. 3.9(a). At that time the existence of a richer structure in the near field was not yet known. We can now revisit their experiment and pose new questions. To obtain the same results the authors could have chosen to image either the back or front facet of the crystal, but not the center. Strangely enough, we find that the violation of the separability criterion depends on which plane is being imaged. The reason is that this criterion depends only on field intensities, while entanglement may also exist in the phase structure, which, as we illustrated, is not trivial. We provide in this way experimental support to proposed entanglement migration between amplitude and phase [30]. Additionally, the existence of more complex non-bell shaped transverse profiles at  $\varphi \neq 0$ , like the ones presented in Fig. 3.6, indicates that a larger number of

modes is necessary to perform a Schmidt decomposition [13] and, consequently, a higher degree of spatial entanglement for non-perfect phase matching is to be expected. We have recently observed this phenomenon [61], which is discussed in Chapter 5 of this thesis.

### 3.4 Conclusion

In this Chapter we have explored the near-field correlations in the two-photon field generated by spontaneous parametric down conversion. Two different theoretical approaches were presented, each one leading to a different integral representation of the field. Numerical simulations can be performed using either formula, both providing the same predictions. In order to experimentally access the correlations in the near field a new regime of operation was introduced, in which the width of the detection modes is determined by an optimal trade-off between resolution and detection efficiency. The detection modes should be small enough to obtain sufficient spatial resolution, but large enough not to lose too many coincidence counts.

The phase-matching condition, imposed by the finite thickness of the crystal, leads to some remarkable features. Among them we highlighted the observation of intriguing three-dimensional structures, the presence of spatial antibunching, a link to previous results on second harmonic generation, the observation of correlations that resemble Bessel beams in propagation, and the prediction of fourth-order phase singularities. Furthermore, operation under phase mismatch reveals a rich set of non-bell shaped spatial correlations. We have already obtained evidence that this higher complexity leads to a higher degree of spatial entanglement [61].

## Appendix A

In this appendix we will present an analytical result for the on-axis correlation  $V(\rho_- = 0; z)$  for perfect phase-matching ( $\varphi = 0$ ). Our starting point is Eq. (3.7). We substitute Eq. (3.6) for  $V(\rho_-; z)$  and consider Gaussian shaped detection modes

$$\phi_j(\rho_j - \rho'_j) \propto \exp\left[-\frac{(\rho_j - \rho'_j)^2}{w_d^2}\right], \quad (3.15)$$

where  $w_d$  is the width of the detection mode in the focused  $z$  plane. After integrating over the transverse coordinates  $\rho'_s$  and  $\rho'_i$  we obtain

$$V_{\text{proj}}(\rho_-; z) \propto \int_{-\infty}^{+\infty} d\mathbf{q} \operatorname{sinc}\left(\frac{L|\mathbf{q}|^2}{2nk_0} + \varphi\right) \exp\left[-\frac{|\mathbf{q}|^2 w_d^2}{2} - i\frac{|\mathbf{q}|^2}{k_0} z - i\mathbf{q} \cdot \rho_-\right]. \quad (3.16)$$

This equation is rotationally symmetric and can be integrated over the azimuthal angle to yield

$$V_{\text{proj}}(\rho_-; z) \propto \int_0^{+\infty} dy \operatorname{sinc}\left(\frac{L}{2nk_0}y + \varphi\right) J_0(\sqrt{y}\rho_-) \exp\left[-\left(\frac{w_d^2}{2} + i\frac{z}{k_0}\right)y\right], \quad (3.17)$$

where  $\rho_- \equiv |\boldsymbol{\rho}_-|$ ,  $y = |\mathbf{q}|^2$ , and  $J_0$  is the 0th order Bessel function. Most of our numerical simulations were performed using this equation.

Next we consider the axial correlations ( $\rho_- = 0$ ) for perfect phase matching ( $\varphi = 0$ ). In this case, Eq. (3.17) has an analytical solution, the square of which is the coincidence counting rate

$$R_{cc}(0; z) \propto |V_{\text{proj}}(0; z)|^2 \propto \left| \arctan\left[\frac{L}{n} \frac{1}{k_0 w_d^2 + 2iz}\right] \right|^2. \quad (3.18)$$

Eq. (3.18) shows how the ratio  $R_{cc}(0; L/2n)/R_{cc}(0; 0)$  between the coincidence rates observed with both detection foci positioned either at the facets or in the center depends sensitively on the size of the detection modes. For our experiments this width is  $w_d = 7 \mu\text{m}$ , which leads to a ratio  $R_{cc}(0; L/2n)/R_{cc}(0; 0) = 1.25$ , both theoretically and experimentally. For smaller  $w_d$  this ratio is expected to increase, leading to a divergence for  $w_d \rightarrow 0$ .

This result differs from the theoretical predictions presented in [48]. The reason is that the authors of Ref. [48] assume that the system can be treated one-dimensionally without loss of generality. The integrated sinc function present in Eq. (3.16), however, behaves quite differently if its argument is a one-dimensional or bi-dimensional vector. Equation (3.18) is the correct expression for a realistic three-dimensional system.

## Appendix B

In this appendix we will show explicitly the equivalence between the key equation (3.7), similar to (3.16), and (3.13). We start with Eq. (3.16) and write the ‘‘sinc’’ function as

$$\operatorname{sinc}\left(\frac{L|\mathbf{q}|^2}{2nk_0} + \frac{L}{2}\Delta k_z^0\right) = \frac{1}{L} \int_{-L/2}^{+L/2} \exp\left(\frac{i|\mathbf{q}|^2}{nk_0}z'' + i\Delta k_z^0 z''\right) dz'', \quad (3.19)$$

where we used the definition of the collinear phase mismatch  $\varphi = \frac{L}{2}\Delta k_z^0$ . Next we make a change of variables  $z' = nz - z''$ . We now recognize the original integral in  $\mathbf{q}$  as the Fourier transform of a complex Gaussian function. It can be

immediately evaluated

$$\int_{-\infty}^{+\infty} (\dots) d\mathbf{q} = \exp\left(\frac{i}{4} \frac{k\rho_-^2}{z' - iz_n}\right) \frac{i\pi k}{z' - iz_n}, \quad (3.20)$$

where  $z_n = \frac{1}{2}nk_0w_d^2$ . We can thus recover Eq. (3.13), which reads

$$V(\rho_-; z) \propto \int_{-L/2-nz}^{+L/2-nz} dz' \frac{\exp(-i\Delta k_z^0 z')}{z' - iz_n} \exp\left(\frac{i}{4} \frac{k\rho_-^2}{z' - iz_n}\right). \quad (3.21)$$



# 4

## Effect of a strongly focused pump on type-I spontaneous parametric down conversion

We experimentally study the spatial properties of the field generated by spontaneous parametric down conversion (SPDC) when the pump laser beam is strongly focused in the nonlinear crystal. Special attention is paid to classical intensity measurements with a CCD camera. We introduce the concept of a classical equivalent source that replicates all the coherence properties of SPDC light and explains all our experimental results. We show that, in contrast with experiments with a well-collimated pump, here both the phase-matching conditions and the position of the focusing plane determine the measured intensity profiles in the image plane of the crystal. The transition from the near-field regime to the far field is investigated. Measurements of two-photon correlations under strong focusing are also presented and the special features thereof are discussed.

H. Di Lorenzo Pires, F. M. G. J. Coppens, and M. P. van Exter, *Type-I spontaneous parametric down conversion with a strongly focused pump*, Phys. Rev. A **38**, 033837 (2011).

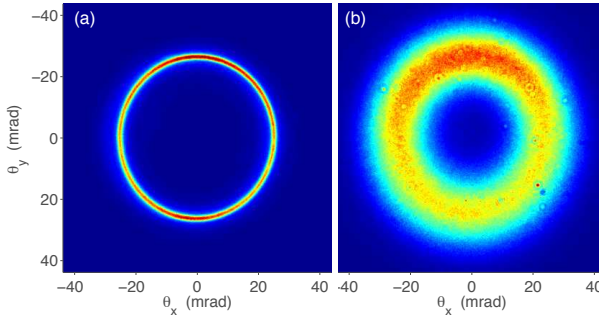


Figure 4.1: Typical far-field intensity profiles for type-I SPDC measured for (a) collimated pump and (b) strongly focused pump.

Spontaneous parametric down-conversion (SPDC) is a non-linear optical process in which some photons from a laser beam can effectively be split into two lower-frequency photons [2, 9, 10, 14, 31, 62]. The theoretical model of down-conversion of light belongs to the domain of quantum optics, which is necessary to explain the highly non-classical photon statistics exhibited by the generated photons. Indeed, if one tries to understand the SPDC process within the classical optics paradigm, one will be stumped by the following observation. A completely coherent laser beam generates, after interacting with a crystal, a highly incoherent beam which still has a very special spatial distribution. Figure 4.1(a) shows a typical measurement of a far-field intensity profile. The so-called SPDC ring is very incoherent, but at the same time seems to be a clear signature of a coherent process. What is then the origin of the resulting randomness? A solution to this difficulty is to admit that coherence should be preserved, but in the form of a high-order coherence. Such a generalization was introduced by Glauber, in his prestigious “quantum theory of optical coherence” [8]. He realized that the classical concept of coherence was no longer adequate to the needs of various experiments at that time. In the context of SPDC, one recognizes nowadays the so-called *two-photon field*, which is endowed with high-order coherence but lacks low-order coherence, i.e., where the two-photon state is pure while the reduced one-photon state is mixed. This observation is closely related to the concept of *entanglement* [13,25,26,36,61]. Had the modes not been entangled, the field would be coherent in all orders.

Naturally, there are many different regimes in which one can produce down-converted light. Both the coherence and the spatial shape of the emitted field depend on the pump shape and on the phase matching conditions. In the most popular configuration, a well-collimated laser beam is used to pump the nonlinear crystal. In this regime, the emission is highly incoherent and both the near-field and far-field intensities have been extensively studied. Figure 4.1(a) shows the far-field intensity pattern observed in this regime. Due to the small momentum spread in the initial beam, the SPDC ring at a fixed emission frequency is very

---

narrow, indicating the conservation of transverse momenta. A near-field image under the same conditions only reveals the spatial profile of the pump laser, in this case a Gaussian. Note that these considerations apply to *classical* intensity measurements with a CCD camera. More interesting structures are revealed in the near field for correlations measured by two scanning detectors, as shown in Chapters 2 and 3 (Refs. [39,63]). For an excellent review on the quantum aspects of the spatial correlations in SPDC, see Ref. [64].

More recently, the effect of strongly focused pumping on SPDC has been considered [65–76]. For type-II down conversion, focusing has been shown to create an asymmetric broadening of the far-field rings [68,70]. For type-I SPDC, the effect is illustrated in Fig. 4.1(b). We see that a large momentum spread in the initial beam causes a broadening of the ring, as a larger set of transverse momenta can now be phase-matched. It has also been demonstrated how the coupling of down converted photons into optical fibers can be enhanced by properly focusing the pump beam [66,74–76]. Not much attention has been paid, however, to the shape of the emission in the near field (or image plane) of the crystal, which is the topic of this Chapter.

In this Chapter, we study the spatial structure of type-I down-converted light generated by a highly focused Gaussian beam. In particular, we explore the rich structures that appear in the image plane of the crystal. Surprisingly, in the transition from plane-wave to focused pumping, the near-field intensity profiles reveal an extremely rich and yet unexplored structure. Most of this Chapter concentrates on the *classical* intensity patterns that can be measured by a CCD camera. Contrary to the far-field, where only the phase-matching conditions and the divergence of the pump determine the intensity patterns, the near-field patterns strongly depend on the exact focusing plane. The use of a focused pump is also interesting because in this regime the down-converted light can be almost coherent. In this way, it will be possible to observe the transition from the near-field to the far-field as would be expected from a Fourier relationship.

Since most of our experiments are classical, it is tempting to describe the results with a theoretical model that is as classical as possible. In this context, we have developed a simple model that allows us to compute the coherence function of the down-converted light. More specifically, we obtain the *classical equivalent source*, which is sufficient to explain our measurements. We also show that these predictions agree with those from the standard SPDC model based on a two-photon field.

This Chapter is organized as follows. In Section 4.1 we present a theoretical formulation of the problem and calculate the coherence function of the generated field. In Section 4.2 we introduce our experimental setup and present results of near-field intensity measurements. For comparison, we present in Section 4.3 measurements of two-photon correlations and discuss our experiments in the context of the well-known two-photon wavefunction. A summary of our results and conclusions are presented in Section 4.4.

## 4.1 Classical equivalent source of parametric down conversion

The standard quantum model of spontaneous parametric down conversion consists in writing the Hamiltonian of the interaction of the pump with the nonlinear crystal and calculating the evolution of the initial state by expanding the time evolution operator in a power series [2, 9, 10, 14, 31, 62]. The initial state is considered to be the vacuum state plus a classical coherent pump. The final state will also contain photon pairs, traditionally called *single* and *idler*, whose spatial and spectral distributions are completely described by the obtained two-photon wavefunction. If one is interested not in two-photon correlations, but in the single-photon properties, one can obtain the reduced one-photon state by a partial trace, i.e., integrating over all possible modes of the other photon.

Many experiments with SPDC do not directly probe the quantum aspects of two-photon correlations, but instead, use single detectors to measure the spatial and spectral properties of the emitted field. Is it possible to explain the outcomes of such measurements without the detour via a two-photon state? In other words, is there a semi-classical model to explain those classical results? It is known that SPDC, within the classical coherence paradigm, can be described as a three-wave mixing process between the pump beam and quantum vacuum fluctuations, which is now the only non-classical element in the description [77,78]. Specially in this context, where one interprets the generated field as a parametric amplification of noise fluctuations, SPDC is also known as *parametric fluorescence*.

The usual route to describe the spatial and spectral pattern formation in parametric fluorescence consists in writing the governing differential equations of the field in the nonlinear medium, including a stochastic term representing the vacuum noise [79,80]. The problem of the origin of coherence in parametric fluorescence has been subject of investigation and the outcome depends crucially on the experimental conditions. For a plane-wave pump, it has been argued that walk-off is the key ingredient for the onset of coherence [81], while in the focused regime, “spatial mode locking” is the responsible mechanism [82]. It has also been shown that, in the spatiotemporal domain, the emission has a special skewed structure [83–85]. Many of the theoretical models behind these phenomena are quite involved and numerical simulations are usually required to illustrate the underlying physics.

Below, we introduce a model that sheds light on the origin of coherence in SPDC for different focusing and phase-matching conditions. Although very simple, it provides the exact working equations, in the sense that it equals those obtained via a partial trace of the complete two-photon field (see Sec. 4.3). We will restrict the analysis to describe our measurements of near-field intensities of frequency-degenerate type-I SPDC generated by a cw-pump, but it can, in principle, be extended to more general cases.

Figure 4.2 shows the geometry considered in the calculations. A Gaussian laser beam is initially focused inside a nonlinear crystal of length  $L$ . The Rayleigh range inside the crystal is  $z_p = \frac{1}{2}k_p w_p^2$ , where  $k_p$  is the pump wave number and  $w_p$  the beam waist. In order to clarify the theoretical description and simplify

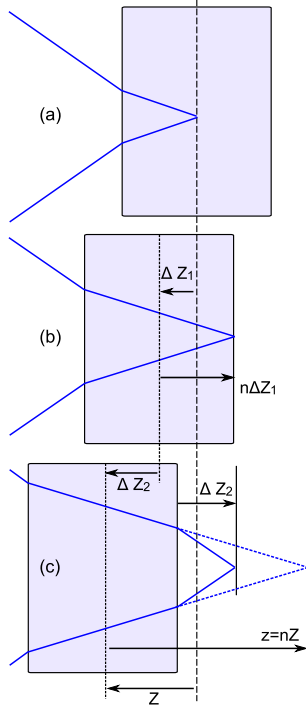


Figure 4.2: Geometry considered in our calculations and measurements. (a) A Gaussian beam is strongly focused in the center of a nonlinear crystal. (b) Pump focused inside the crystal. A crystal displacement  $\Delta Z_1$  corresponds to a focus displacement  $n\Delta Z_1$  with respect to the center of the crystal (we show the extreme case). (c) Pump focused outside the crystal. An extra crystal displacement  $\Delta Z_2$  beyond the point where the pump focus is located at the back facets brings the pump focus the same distance  $\Delta Z_2$  behind this facet. In the theoretical description we assume that the output of the crystal is embedded in a medium of refractive index  $n$ , so that the pump focus is always located at a distance  $z = nZ$  from the center of the crystal, as shown by the dashed lines.

the equations, we will assume first that the right-hand side of the crystal, which is our region of interest, is embedded in a medium with the same refractive index  $n$ , but without nonlinearities. The consequences of refraction for the real experiment will be discussed later on.

The essence of nonlinear optical phenomena is the coupling of two waves, yielding a response at a different frequency. We are interested in down-converted light at a frequency  $\omega$ , for a pump frequency  $\omega_p = 2\omega$ . Our model consists in assuming that each point inside the crystal emits down-converted light driven by the source term  $E_p(\mathbf{r}')\xi^*(\mathbf{r}')$ , which describes the coupling of the pump field to the quantum noise fluctuations at position  $\mathbf{r}'$ . The observed field  $A(\mathbf{r})$  is just the

sum of all contributions propagated to the observation point  $\mathbf{r}$ , namely,

$$A(\mathbf{r}) = \int_{crystal} d\mathbf{r}' E_p(\mathbf{r}') \xi^*(\mathbf{r}') \mathcal{G}(\mathbf{r} - \mathbf{r}'). \quad (4.1)$$

The propagator  $\mathcal{G}(\mathbf{r} - \mathbf{r}')$  is, in our case, the Green function of the paraxial wave equation, which assumes the form [86]

$$\mathcal{G}(\mathbf{r} - \mathbf{r}') = \frac{k e^{ik(z-z')}}{2\pi i(z-z')} \exp \left[ \frac{ik|\boldsymbol{\rho} - \boldsymbol{\rho}'|^2}{2(z-z')} \right], \quad (4.2)$$

where we express the position  $\mathbf{r} = (\boldsymbol{\rho}, z)$  in polar coordinates and  $k = n(\omega)\omega/c$  is the wave number at the desired frequency  $\omega$ .

The coherence properties of the generated field can be obtained by an ensemble average and is described by the coherence function  $W(\mathbf{r}_1, \mathbf{r}_2) = \langle A^*(\mathbf{r}_1)A(\mathbf{r}_2) \rangle$ . The signal (or idler) mode is initially in the vacuum state  $|0\rangle$ . One can show that the expected value of the coherence in the vacuum state is given by

$$\langle \xi^*(\mathbf{r})\xi(\mathbf{r}') \rangle = \mathcal{G}(\mathbf{r} - \mathbf{r}'). \quad (4.3)$$

This crucial result is a consequence of the unequal-time commutation relation of the electric field operator  $[E(\mathbf{r}, t), E^\dagger(\mathbf{r}', t')] = G(\mathbf{r}, \mathbf{r}'; t - t')$ , where  $G$  is the time dependent Green function. It is proven, for instance, in Ref. [87] and implies that  $\langle 0|EE^\dagger|0\rangle = G$ . By expressing the Green function in the frequency domain via a Fourier transform [88,89], we can select the desired spectral component of  $\mathcal{G}$  and obtain Eq. (4.3). With those ingredients, it is easy to show that the coherence of the SPDC field is given by

$$W(\mathbf{r}_1, \mathbf{r}_2) = \iint_{crystal} d\mathbf{r}' d\mathbf{r}'' W_s(\mathbf{r}', \mathbf{r}'') \mathcal{G}^*(\mathbf{r}_1 - \mathbf{r}') \mathcal{G}(\mathbf{r}_2 - \mathbf{r}''), \quad (4.4)$$

where

$$W_s(\mathbf{r}', \mathbf{r}'') = E_p^*(\mathbf{r}') E_p(\mathbf{r}'') \mathcal{G}(\mathbf{r}' - \mathbf{r}''). \quad (4.5)$$

We can interpret these equations as follows. Equation (4.4) is nothing more than the coherence between the points  $\mathbf{r}_1$  and  $\mathbf{r}_2$  due to a volumetric source of partially-coherent light. The source field  $W_s$  is propagated to the observation points using two Green functions  $\mathcal{G}$ . The exact shape of the source is given by Eq. (4.5), which we consider as the *classical equivalent source* of SPDC. It means that a volumetric element with the dimensions of the crystal, emitting light with a initial coherence described by Eq. (4.5), replicates all classical properties of the SPDC light. The appearance of the term  $\mathcal{G}(\mathbf{r}' - \mathbf{r}'')$ , instead of  $\delta(\mathbf{r}' - \mathbf{r}'')$  as one would expect from a pure fluorescent source, is a consequence of the coupling of the pump to the vacuum fluctuations. It is this term that makes parametric fluorescence different.

In order to measure the  $z$  dependence of the field, we will translate the crystal longitudinally. Figure 4.2 shows how refractive effects affect the results. We call  $Z$  the physical displacement of the crystal. In Fig. 4.2(b) we see that, while the pump is still focused inside the crystal, a displacement  $\Delta Z_1$  of the crystal corresponds to a displacement  $n\Delta Z_1$  of the focus with respect to the center of the crystal. The reason is that, upon entering a dielectric medium, a paraxial Gaussian beam retains its waist but is stretched in the longitudinal direction by a factor  $n$ . On the other hand, when the pump is focused outside the crystal, as in Fig. 4.2(c), an extra crystal displacement  $\Delta Z_2$  correspond now to a focus displacement of also  $\Delta Z_2$ . In our simplified model, in which the output of the crystal is embedded in a medium of refractive index  $n$ , the pump focus is always located at a distance  $z = nZ$  from the center of the crystal. Experimentally, the field at the plane  $z$ , which contains the beam waist, is imaged with a lens onto a CCD camera. By moving the nonlinear crystal, we change the relative position of the focus with respect to the center of the crystal, in effect probing the longitudinal dependence of the field. It is important to remark that, whether the pump is focused inside the crystal or outside, the lens will always image the pump focus. In other words, we always have a “sharp” image of the focus plane, independent of the position of the crystal. This holds both for the real experiment and for our simplified theoretical description. The effect of such an imaging scheme can be mathematically described in our model by propagating the source field to the plane  $nZ$ . Considering the explicit form of the pump beam

$$E_p(\boldsymbol{\rho}, z) \propto \frac{e^{ik_p z}}{z - nZ - iz_p} \exp\left[\frac{ik_p \rho^2}{2(z - nZ - iz_p)}\right], \quad (4.6)$$

the SPDC near-field intensity  $I(\mathbf{r}) = W(\mathbf{r}, \mathbf{r})$  can be calculated using Eqs. (4.2) - (4.6). After integrating the Gaussian functions and performing some additional manipulations, we find

$$\begin{aligned} I(\boldsymbol{\rho}, Z) \propto & \int_{-L/2-nZ}^{L/2-nZ} dz' \int_{-L/2-nZ}^{L/2-nZ} dz'' \frac{e^{-i\Delta k(z'-z'')}}{z_p(z'-z'') - 2iz'z''} \\ & \times \exp\left[\frac{-2k\rho^2(z'-z'')}{z_p(z'-z'') - 2iz'z''}\right], \end{aligned} \quad (4.7)$$

where  $\Delta k = k_p - 2k$  is the on-axis wavevector mismatch.  $I(\boldsymbol{\rho}, Z)$  is the intensity that we measure with a CCD camera when the crystal is at position  $Z$ . In order to interpret Eq. (4.7), it is useful to rewrite it in a different form. One can show that

$$I(\boldsymbol{\rho}, Z) \propto \int_{-\infty}^{+\infty} d\boldsymbol{\rho}' |V(\boldsymbol{\rho} - \boldsymbol{\rho}', Z)|^2 e^{-(\boldsymbol{\rho} + \boldsymbol{\rho}')^2 / 2w_p^2}, \quad (4.8)$$

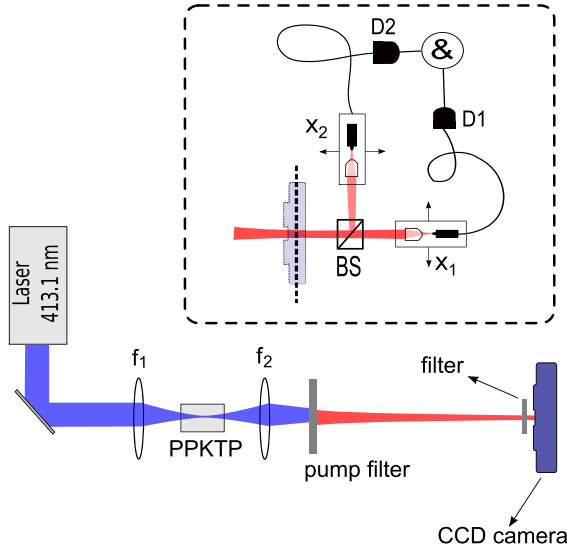


Figure 4.3: Experimental setup used to generate SPDC light and to measure the intensity pattern in the image plane of the crystal. Lens  $f_1 = 100$  mm focuses the pump to a  $w_p = 11 \mu\text{m}$  spot size and lens  $f_2 = 59$  mm makes a  $10\times$  magnified image of the pump focus plane onto a CCD camera. The crystal can be longitudinally translated. The inset shows a modified detection scheme used to measure two-photon correlations, as discussed in Sec. 4.3.

with

$$V(\boldsymbol{\rho}, Z) = \int_{-L/2-nZ}^{L/2-nZ} dz' \frac{e^{-i\Delta kz'}}{z'} e^{ik\rho^2/4z'}. \quad (4.9)$$

From Eq. (4.8) we see that, for a tightly focused pump, the intensity  $I(\boldsymbol{\rho}) \rightarrow |V(2\boldsymbol{\rho}, Z)|^2$ . Equation (4.8) is expressed as a convolution, where the Gaussian profile of the pump beam acts as a smoother. As we will show in Sec. 4.3, Eqs. (4.8) and (4.9) are identical to the equations obtained via the standard approach based on the two-photon field. Here, we have shown that the same results can be obtained without such a detour. We will also demonstrate that Eq. (4.9) is simply the Fourier transform of a propagated sinc-type phase matching function. It is interesting to notice that, for a well collimated pump beam, the *far-field* profile is well described by a 'sinc'. For a strongly focused pump beam, it is the *near-field* intensity that can be describe by (the Fourier transform of) the 'sinc'. In the next section we will present measurements performed in the strongly focused regime.

## 4.2 Near-field intensity measurements

The purpose of our experiments is to explore the near-field intensity profiles of light generated by SPDC under strong focusing and observe the transition between near and far field in the regime of almost coherent emission.

Figure 4.3 shows the experimental setup. A  $L=20$  mm long periodically polled  $\text{KTiOPO}_4$  crystal (PPKTP) is pumped by a 50 mW krypton-ion laser beam operating at 413.1 nm, generating SPDC light. A  $f_1 = 100$  mm lens is used to focus the pump laser to a  $w_p = 11$   $\mu\text{m}$  spot size. These experimental parameters satisfy the paraxial wave approximation assumed in the theoretical description. The crystal is mounted on a translation stage that allows it to be moved longitudinally along the focal region. The distance between the center of the crystal and the beam is depicted in Fig. 4.2. A second lens  $f_2 = 59$  mm is used to make a  $10\times$  magnified image of the plane where the pump beam is focused onto a CCD camera (Apogee Alta U1). A narrow band spectral filter ( $\Delta\lambda = 5$  nm at  $\lambda = 826.2$  nm) is used to select light close to frequency degeneracy.

We first investigate the near-field intensity patterns for different phase matching conditions and different longitudinal positions  $Z$  of the nonlinear crystal. For our type-I PPKTP, the on-axis phase mismatch  $\varphi = \frac{1}{2}\Delta k L$  depends approximately linearly on the crystal temperature and can therefore be conveniently adjusted. The derivative  $d\varphi/dT = (4.0 \pm 0.3) \text{ K}^{-1}$  has been experimentally obtained. For our measurements, we choose a certain phase mismatch  $\varphi$  and scan the longitudinal position of the crystal. For each position we take a picture with the CCD camera. The results shown next are built by taking a horizontal ( $x$ ) cross section of each of these figures and positioning them next to each other. In other words, we show the dependence of the *intensity cross sections*  $I(x, Z)$  versus the  $Z$  position of the crystal. Owing to the rotational symmetry of the images measured by the CCD, we are in effect fully characterizing the near-field intensity  $I(\rho, Z)$ .

Figure 4.4 shows the experimental and theoretical results for four different values of the phase mismatch  $\varphi$ . Different acquisition times were used for these pictures in order to compensate for the change in total power with phase matching. The overall photon flux  $F(\varphi)$  relative to its  $\varphi = 0$  value is given by  $F(\varphi)/F(0) = 1 + (2/\pi)[\varphi \text{sinc}^2\varphi - \text{Si}(2\varphi)]$ , where  $\text{Si}(x) = \int_0^x \text{sinc } x' dx'$  is the sine integral function. This dependence has been checked experimentally. A curve fitting of  $F(\varphi)$  revealed to be a very reliable method to determine the temperature  $T_0 = (60.76 \pm 0.02)^\circ\text{C}$  for perfect phase matching and the aforementioned derivative  $d\varphi/dT$ . The dashed white lines in the theoretical plots show the positions  $Z = \pm L/2n$ , where the pump focus coincides with the crystal facets.

Figures 4.4(a,e) correspond to  $\varphi = -7.0$ , being associated with open far-field SPDC rings and more efficient conversion. Figures 4.4(b,f) correspond to perfect phase matching, i.e.,  $\varphi = 0$ . Figures 4.4(c,g) for  $\varphi = 1.0$  and Figs. 4.4(d,h) for  $\varphi = 2.6$  are associated with closed far-field SPDC rings and inefficient emission.

We can interpret the results as follows. While the pump beam is focused in a plane *inside* the crystal, the intensity profiles are bounded to a limited range  $|x| \lesssim 40$   $\mu\text{m}$ . The dashed lines indicate the facets of the crystal, which are spaced

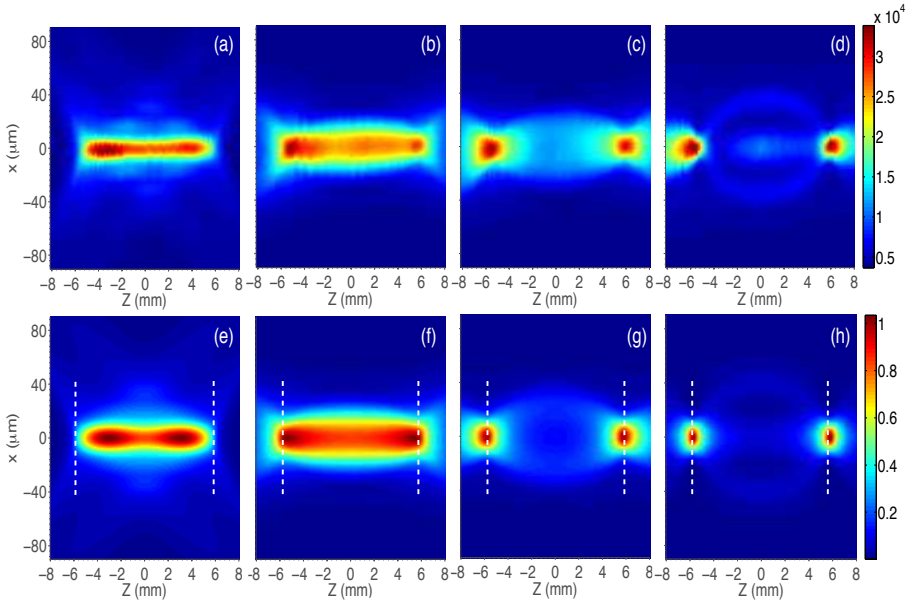


Figure 4.4: Measured (upper row) and calculated (lower row) cross sections of the near-field SPDC intensity patterns as a function of the longitudinal position  $Z$  of the crystal. Results for four different values of the phase mismatch are shown, namely, (a,e)  $\varphi = -7.0$ , (b,f)  $\varphi = 0.0$ , (c,g)  $\varphi = 1.0$ , and (d,h)  $\varphi = 2.6$ . The dashed white lines in the theoretical plots show the positions  $Z = \pm L/2n$ , where the pump focus coincides with the crystal facets.

by  $\Delta Z = L/n = 11.6$  mm. As predicted by Eqs. (4.8) and (4.9), the results are symmetric with respect to the  $Z = 0$  plane; the profiles are thus identical if one focuses the pump on either sides of the crystal. For  $\varphi \leq 0$ , the width of the distribution is approximately constant and depends only slightly on  $Z$ ; the curves are narrower for more negative values of  $\varphi$ . For  $\varphi > 0$  there is a more noticeable position dependence. When the beam waist coincides with either facets of the crystal, the near-field intensity has a very pronounced central peak. All other focusing planes lead to a broader intensity distribution. Figure 4.4(d) shows, for instance, that when the beam is focused in the center of the crystal, three small but wide peaks are observable. This redistribution of energy is such that the total power  $P = \int I(\rho, Z) 2\pi\rho d\rho$  is conserved. The reason is that the total SPDC yield depends only on the divergence of the pump beam, which is constant throughout the experiment. All structures observed in Fig. 4.4 are a consequence of the diffraction integrals, which can be quite interesting, as in Fig. 4.4(d). The transition of an axial valley to an axial peak in near-field imaging also appears, for instance, in the context of Fresnel diffraction. By changing the initial phase structure of the field, many different diffraction patterns can be observed. Here, the phase-matching conditions strongly determine this phase structure.

Figure 4.5 shows the measured cross sections of intensity patterns taken for

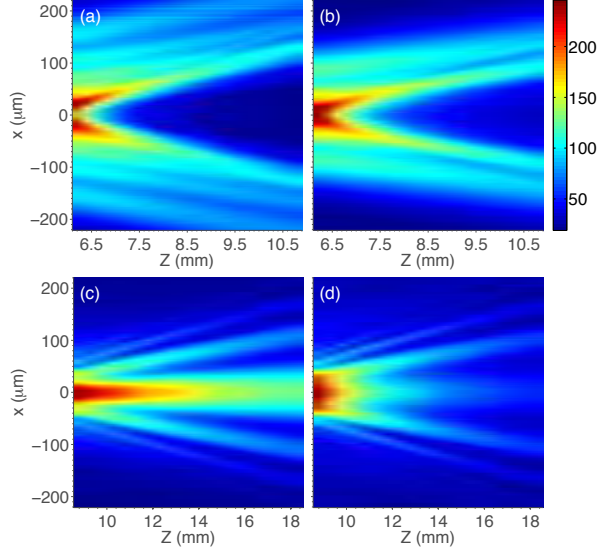


Figure 4.5: Measured cross sections of the intensity patterns in the transition region between the near field and the far field. The square root of the measured intensity is shown in a false color scale. The figures correspond to the following phase-mismatch parameters: (a)  $\varphi = -15.0$ , (b)  $\varphi = -7.0$ , (c)  $\varphi = 3.0$ , and (d)  $\varphi = 9.0$ .

$Z$  values corresponding to the transition from the near to the far field. For clarity, the square root of the measured intensities is shown. The four figures correspond to (a)  $\varphi = -15.0$ , (b)  $\varphi = -7.0$ , (c)  $\varphi = 3.0$ , and (d)  $\varphi = 9.0$ . We made the horizontal axis of Figs. 4.5(a) and (b) different from Figs. 4.5(c) and (d) because for  $\varphi < 0$ , the transition from the near field to the far field occurs for  $Z \approx 6 \text{ mm} \approx L/2n$ , while for  $\varphi > 0$  the far-field begins for  $Z \approx 8 \text{ mm} > L/2n$ . This can also be seen in Fig. 4.4. Since the pump beam is focused outside the crystal, the horizontal axis, which represents the crystal displacement, is now equal to the displacement of the pump focus from the back facet plus  $L/2n$  (see remarks in Sec. 4.1).

We see that all transverse intensity profiles in Fig. 4.5 are clearly a function of angle only, expanding under propagation without gaining new structures. Figures 4.5(a) and (b) correspond to open far-field SPDC rings ( $\varphi < 0$ ); the radius of the ring is proportional to  $\sqrt{|\varphi|}$ . Figures 4.5(c) and (d) correspond to closed rings ( $\varphi > 0$ ), but the typical patterns of non-phase matched SPDC can still be recognized.

The theoretical predictions, calculated with the formalism of Sec. 4.1, agree very well with the experimental results. Those results are, to the best of our knowledge, the first measurements of Eq. (4.8) in the intensity patterns of SPDC. This function has only been measured in the correlations between the two-photons [63] in a weak focusing geometry. We have shown now that by

using a strongly focused pump, these patterns can also be detected with a CCD camera.

It might come as a surprise that we are able to observe detailed spatial structures both in the near-field images (Fig. 4.4) and in the far-field type images obtained after sufficient propagation (Fig. 4.5). This is possible only because our source is not completely incoherent, but instead still contains a considerable degree of coherence. The number of generated modes at perfect phase matching ( $\varphi = 0$ ) and with the pump focused at the center of the crystal ( $Z = 0$ ) depends on a single, dimensionless parameter  $b\sigma = \sqrt{L/2z_p}$ . In both limits  $b\sigma \rightarrow 0$  and  $b\sigma \gg 1$ , the number of generated modes is very large and the emission is almost incoherent [13]. When  $b\sigma \approx 1$ , the number of modes is close to unity and the field is almost coherent. For our experiments,  $b\sigma = 2.5$ , meaning that some coherent effects at the single photon level can still be observed, like the approximate Fourier relation between the near and far field. This can be physically understood as follows. The patterns measured in Fig. 4.4 are described by the Fourier transform  $\mathcal{F}$  of a ‘sinc’ function, propagated and convoluted with a narrow Gaussian. The narrower the pump, the more the profiles approach  $\mathcal{F}(\text{sinc})$ . On the other hand, the far-field patterns shown in Fig. 4.5 are qualitatively described by a ‘sinc’ function. The rings are somewhat thicker, though, due to the divergence of the pump beam. The less divergent the pump is, the more the far-field resembles a ‘sinc’. Only in the intermediate, almost-coherent regime ( $b\sigma \approx 1$ , corresponding to a “narrow, but not too divergent” beam) one will be able to observe the approximate Fourier relation between near and far fields.

### 4.3 Near-field two-photon correlations

The results presented so far can be explained by the semi-classical model of Sec. 4.1. In this section we will show how our measurements can equally well be understood in terms of the well-know entangled two-photon field model of parametric down conversion. Furthermore, we will present experimental evidence of entanglement migration between the amplitude and the phase of the field.

The so-called *two-photon field*  $\tilde{A}(\mathbf{q}_1, \mathbf{q}_2)$  is a complex valued function that gives the probability amplitude of finding one photon with transverse momentum  $\mathbf{q}_1$  and the other photon with transverse momentum  $\mathbf{q}_2$ . In the absence of walk-off, this function has a special form, factorizing in two functions of the sum and difference momenta as [64]

$$\tilde{A}(\mathbf{q}_1, \mathbf{q}_2) = \tilde{E}_p(\mathbf{q}_1 - \mathbf{q}_2) \operatorname{sinc} \left( \frac{L}{4k_p} |\mathbf{q}_1 - \mathbf{q}_2|^2 + \varphi \right), \quad (4.10)$$

where  $\tilde{E}_p$  is the angular spectrum of the pump beam with wavenumber  $k_p$ ,  $L$  is the crystal thickness, and  $\varphi$  is the on-axis phase mismatch, as defined in Sec. 4.1.

In order to describe measurements in the near field, i.e., in the image plane of the crystal, the wavefunction should be written in spatial coordinates, which is obtained by combining a Fourier transform from momenta  $\mathbf{q}$  to positions  $\boldsymbol{\rho}$  with a

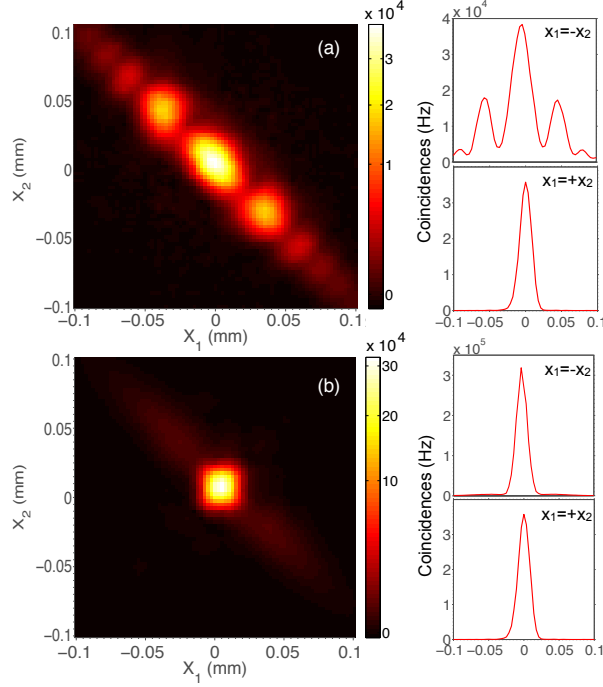


Figure 4.6: Coincidences rate as measured by two scanning detectors with transverse positions  $x_1$  and  $x_2$ . The phase mismatch parameter is set to  $\varphi = 3.2$  and the pump beam is focused (a) at the center of the crystal and (b) at the crystal facet. Diagonal scans for  $x_1 = x_2$  and  $x_1 = -x_2$  are also shown.

propagation to the desired  $z$  plane. One can show that the spatial representation of the two-photon field also factorizes as

$$A(\boldsymbol{\rho}_1, \boldsymbol{\rho}_2; z) = E_p \left( \frac{\boldsymbol{\rho}_1 + \boldsymbol{\rho}_2}{2}, z \right) V(\boldsymbol{\rho}_1 - \boldsymbol{\rho}_2, z). \quad (4.11)$$

The function  $V$  is exactly the same as the one defined by Eq. (4.9) and  $E_p$  is the spatial profile of the pump beam. The coincidence rate measured by two detectors at positions  $\boldsymbol{\rho}_1$  and  $\boldsymbol{\rho}_2$  is  $R_{cc} \propto |A|^2$ . The “classical” intensity measured by one single detector can be obtained by a partial trace, i.e., integrating over all possible positions of the other detector such that  $I(\boldsymbol{\rho}, z) \propto \int |A(\boldsymbol{\rho}, \boldsymbol{\rho}_2; z)|^2 d\boldsymbol{\rho}_2$ . We now recover Eq. (4.8) that describes our experimental results. Again, an extremely focused pump would act as a “delta function”, making the measured intensity  $I(\boldsymbol{\rho}, Z) \propto |V(2\boldsymbol{\rho}, Z)|^2$ .

We have studied so far intensity measurements. In the regime we are operating, however, special features also appear in the two-photon correlations. We will now discuss one particular interesting result. In order to measure those cor-

relations we use the modified setup shown in the inset of Fig. 4.3. The ICCD camera is removed and the image plane is now re-imaged with objectives onto the input tips of two single-mode optical fibers, which are then connected to photon counting modules. A beam splitter is used to separate the two photons; coincidences counts are post selected by an electronic circuit.

Figure 4.6 shows the measured coincidence rate when both detectors are scanned horizontally at a phase mismatch  $\varphi = 3.2$ . Due to the rotational symmetry of Eq. (4.11), we are basically mapping the function  $|A(x_1, x_2; Z_0)|^2$ , where  $x_1$  and  $x_2$  are transverse positions of detectors 1 and 2 respectively. The crystal is placed at two different longitudinal positions (a)  $Z_0 = 0$ , in which the pump is focused at center of the crystal, and (b)  $Z_0 = L/2n$ , in which the focus coincides with the crystal facet.

In Fig. 4.6(a), the two-photon field is clearly non-separable, i.e.,  $A(x_1, x_2) \neq f(x_1)g(x_2)$ . Two distinct patterns can be observed in the sum  $x_1 = x_2$  and difference coordinates  $x_1 = -x_2$ . Those diagonals cross sections are also plotted in the right side of the figure. When  $x_1 = x_2$ , we measure the pump profile, which is non-locally transferred to the correlations in the term  $E_p$ . When  $x_1 = -x_2$  we observe the function  $V$ , which characterizes the phase matching conditions. In the regime of strong focusing, the coincidences are very compact in the diagonal  $x_1 = x_2$  and extended in the diagonal  $x_1 = -x_2$ . Note that these combinations are opposite to those observed in the weak focusing regime. As we have argued, measurements with a CCD camera show nothing more than a horizontal projection of this pattern.

Observing now Fig. 4.6(b), where the pump is focused at the crystal facet, one might erroneously conclude that the two photon field is separable, i.e., non-entangled. The pattern is almost circular and the cross sections in the sum and difference coordinates have approximately the same width. However, when the pump is focused at the facet the amount of entanglement, as measured by the Schmidt number  $K$  [13], is actually predicted to be higher. The dependence of the number of entangled modes with the focusing plane is nontrivial and has not yet been extensively studied. By following a procedure similar to the one proposed in [13, 90] we can verify, however, that  $K$  increases when the pump is focused at the crystal facet. The reason of this apparent discrepancy is that correlations exist not only between the amplitude of the two photons, but also between their phases. When the amplitude correlations are minimal, all the entanglement has migrated to the phase of the field [30]. This illustrates the importance of phase entanglement.

## 4.4 Conclusion

In this Chapter we have experimentally studied how strongly focusing of the pump beam shapes the field generated by spontaneous parametric down conversion. Special attention was paid to yet unexplored near-field intensity measurements. We have shown that the collinear phase mismatch and the pump focusing plane are the most important variables in determining the measured intensity pro-

files. We developed a semi-classical model that can explain our measurements via the parametric amplification of vacuum fluctuations. In this way, we obtained a classical equivalent source that is able to mimic all the coherence properties of SPDC light. The equations are in agreement with those obtained via the standard quantum model of SPDC. We have experimentally studied the transition of the intensity distributions from the near field to the far field. The near-field regime extends to a range of the length of the nonlinear crystal, from this point on the SPDC rings start to acquire shape. Finally, we have presented measurements of two-photon correlations under strong focusing. Signatures of amplitude and phase entanglement were discussed. Our results provide new insights into the nature of SPDC emission under strong focusing and have potential applications in experiments where spatial aspects of down conversion are relevant.



# 5

## Transverse mode entanglement in the two-photon field

We introduce and experimentally demonstrate a method to measure the Schmidt number of pure two-photon states entangled in transverse-mode structure. Our method is based on the connection between the Schmidt decomposition in quantum theory and the coherent-mode decomposition in classical coherence theory. We apply the method to two-photon states generated by spontaneous parametric down conversion and show that our results are in excellent agreement with numerical calculations based on the Schmidt decomposition.

The supplementary material, in Appendix 5.A, is unpublished and shows how the results can also be derived in the Wigner function formalism.

H. Di Lorenzo Pires, C. H. Monken, and M. P. van Exter, *Direct measurement of transverse mode entanglement in two-photon states*, Phys. Rev. A **80**, 022307 (2009).

## 5.1 Introduction

Entanglement is an old concept in quantum mechanics that has only recently been recognized as a key resource in quantum information science. In order to take full advantage of the capabilities of a given quantum system for quantum information processing, it is crucial to thoroughly characterize its entanglement and to measure the amount of this resource that is available, a measurement that goes beyond the detection of entanglement signatures.

In the last years, there has been a significant effort to design and implement strategies to measure entanglement without prior state reconstruction [91]. With the increasing dimension of the system, techniques such as quantum state tomography become more and more involved and should, therefore, be avoided. Most of the progress so far has been achieved for simple two-qubit systems. For instance, in Ref. [92] Walborn *et al.* reported the first experimental measurement of concurrence for pure two-qubit states. An estimation of the concurrence for mixed states was also realized [93]. Furthermore, many new theoretical proposals to experimentally quantify the entanglement in low dimensional bipartite systems are being introduced [94–97].

Though the majority of the analyses focuses on realizations with two qubits, there is a growing interest in the high dimensional entanglement of continuous-variable systems. In fact, many existing quantum processing protocols could be boosted by employing larger alphabets [98]. For these intrinsically more complex spaces, the question of whether the amount of entanglement can be obtained without a full state tomography becomes particularly appealing.

## 5.2 The Schmidt number: an operational definition

The most convenient parameter to quantify the amount of entanglement in a continuous variable pure bipartite state  $|\Psi\rangle$  is the Schmidt number  $K$ , defined as the “average” or “effective” number of nonzero coefficients in the Schmidt decomposition [13]

$$|\Psi\rangle = \sum_{n=0}^{\infty} \sqrt{\lambda_n} |\phi_n\rangle \otimes |\psi_n\rangle. \quad (5.1)$$

Equivalently, the Schmidt number  $K$  is the inverse of the purity of the reduced density operator  $\varrho_1$  (or  $\varrho_2$ )

$$\varrho_1 = \text{Tr}_2 [|\Psi\rangle\langle\Psi|] = \sum_{n=0}^{\infty} \lambda_n |\phi_n\rangle\langle\phi_n|. \quad (5.2)$$

Thus,

$$K = \frac{(\sum_{n=0}^{\infty} \lambda_n)^2}{\sum_{n=0}^{\infty} \lambda_n^2} = \frac{(\text{Tr } \varrho_1)^2}{\text{Tr } \varrho_1^2} = \frac{(\text{Tr } \varrho_2)^2}{\text{Tr } \varrho_2^2}. \quad (5.3)$$

Other appropriate quantifiers, such as the I-concurrence [99], can be written in terms of the Schmidt number. For global pure states, each part carries all the information about the amount of entanglement present, as one can conclude by comparing Eqs. (5.1) and (5.2). The more entangled are the parts, the more mixed are the reduced states. The above definition, though mathematically simple, does not provide a clear way for the experimental measurement of the Schmidt number [100]. Due to the high number of terms involved in (5.1), even a numerical calculation of  $K$  may be difficult and time demanding. In view of these difficulties, new “experimentally friendly” parameters were introduced, such as the ratio of widths of single-particle and coincidence distributions [101], in an attempt to directly quantify entanglement.

In this Chapter we show that it is possible to give an operational meaning to the Schmidt number in the framework of coherence theory and present a new method to evaluate and measure, with the least experimental effort, the amount of entanglement associated with the spatial degrees of freedom of an entangled photon pair. For this method to work, we only need to assume that the global state is pure and the reduced states have a sufficiently homogeneous statistics.

In photonic states, the notion of “mixedness” is related to coherence. In fact, the transverse coordinate ( $\mathbf{x}$ ) representation of the reduced density operator in Eq. (5.2) is proportional to the cross-spectral density function of the source  $W_s(\mathbf{x}, \mathbf{x}') \propto \langle \mathbf{x} | \rho_1 | \mathbf{x}' \rangle$ , introduced and analyzed by Wolf [3]. The fields are assumed to be monochromatic. A more appealing, operationally-defined function, is the cross-spectral degree of coherence, obtained by normalizing  $W_s$  by the intensities, i.e.,  $\mu_s(\mathbf{x}, \mathbf{x}') = W_s(\mathbf{x}, \mathbf{x}') / \sqrt{I_s(\mathbf{x})I_s(\mathbf{x}')}$ , where  $I(\mathbf{x}) = W_s(\mathbf{x}, \mathbf{x})$ . If the considered two-photon state is entangled, the reduced one-photon state can never be fully coherent. The more entangled the two-photon state is, the more incoherent is each one of its one-photon components. The average transverse spectral degree of coherence of the one-photon states can be quantified by the *overall degree of coherence* [102], defined by

$$\bar{\mu}^2 = \frac{\iint |W_s(\mathbf{x}, \mathbf{x}')|^2 d\mathbf{x}d\mathbf{x}'}{[\int |W_s(\mathbf{x}, \mathbf{x})|^2 d\mathbf{x}]^2}. \quad (5.4)$$

It can also be seen as an average of the cross-spectral degree of coherence as  $\bar{\mu}^2 = \iint P(\mathbf{x}, \mathbf{x}') |\mu_s(\mathbf{x}, \mathbf{x}')|^2 d\mathbf{x}d\mathbf{x}'$ , where  $P(\mathbf{x}, \mathbf{x}') = I_s(\mathbf{x})I_s(\mathbf{x}') / [\int I_s(\mathbf{x})d\mathbf{x}]^2$ .

It is well known from the classical theory of coherence that the cross spectral density function admits a coherent-mode representation, [3]

$$W_s(\mathbf{x}, \mathbf{x}') = \sum_{n=0}^{\infty} c_n \phi_n^*(\mathbf{x}) \phi_n(\mathbf{x}'), \quad (5.5)$$

where the functions  $\phi_n$  form an orthonormal set and the coefficients  $c_n$  are all positive. Although derived in different contexts, Eqs. (5.2) and (5.5) refer to the same physical property of the source. Therefore, using Eqs. (5.2), (5.4) and (5.5)

one can see that the Schmidt number  $K$  is

$$K = \frac{1}{\bar{\mu}^2}. \quad (5.6)$$

This is our first key result. We introduce another physical meaning to the Schmidt number of two-photon entangled states: it is the inverse of the overall degree of coherence of the reduced state. Although Eq (5.6) is always valid and provides a path to the direct measurement of  $K$ , the experimental determination of  $\bar{\mu}^2$  may require an enormous experimental effort. However, in some important practical situations this effort is considerably reduced, as we will now show.

Depending on the characteristics of the two-photon source, especially if it is highly entangled, its reduced (one-photon) state may describe a *quasi-homogeneous source*. For this class of sources [3], the cross spectral degree of coherence  $\mu_s(\mathbf{x}, \mathbf{x}')$  depends locally only on the difference  $\mathbf{x} - \mathbf{x}'$  and decays to zero if  $|\mathbf{x} - \mathbf{x}'|$  is greater than the transverse coherence length of the source, within which the positional intensity profile  $I_s(\mathbf{x})$  is smoothly varying, that is,  $I(\mathbf{x})I(\mathbf{x}') \approx I^2[\frac{1}{2}(\mathbf{x} + \mathbf{x}')]$ . In this case, the cross spectral density function may be approximated by  $W_s(\mathbf{x}, \mathbf{x}') \approx I[\frac{1}{2}(\mathbf{x} + \mathbf{x}')] g_s(\mathbf{x} - \mathbf{x}')$ . This factorization is exact for Gaussian sources. Defining  $\tilde{g}_s(\mathbf{q})$  as the Fourier transform of  $g_s(\mathbf{x})$ , it can be shown [3] that  $\tilde{g}_s(\mathbf{q})$  is proportional to the far field intensity  $I_{FF}(\boldsymbol{\theta})$ , where  $\boldsymbol{\theta} = \mathbf{q}/k$ ,  $k$  being the wave number. Using the facts just mentioned, and Eqs. (5.4) and (5.6), the Schmidt number can be written as

$$K \approx \frac{1}{\lambda^2} \frac{[\int I_s(\mathbf{x})d\mathbf{x}]^2}{\int I_s^2(\mathbf{x})d\mathbf{x}} \times \frac{[\int I_{FF}(\boldsymbol{\theta})d\boldsymbol{\theta}]^2}{\int I_{FF}^2(\boldsymbol{\theta})d\boldsymbol{\theta}}, \quad (5.7)$$

where  $I_s$  and  $I_{FF}$  are the intensities measured on the source (near field) and on the far field, respectively, and  $\lambda$  is the wavelength. We see that, with two intensity profile measurements (in near and far fields), it is possible to obtain the Schmidt number  $K$  directly, without the need of a full state tomography. This is our second key result, which forms the basis of our experimental analysis.

It is worth mentioning that Eq. (5.7) can also be derived in another elegant way, based on the Wigner function representation. This alternative derivation is shown in Appendix 5.A.

We now illustrate the use of the proposed method to estimate the Schmidt number associated with the transverse mode entanglement in the two-photon field generated by spontaneous parametric down-conversion (SPDC) in a periodically poled crystal. The two-photon state generated by quasi-monochromatic type I SPDC is pure and its wave function in momentum representation assumes the form [19]

$$\Phi(\mathbf{q}_1, \mathbf{q}_2) = \mathcal{N} \mathcal{E}_p(\mathbf{q}_1 + \mathbf{q}_2) \text{sinc}(b^2|\mathbf{q}_1 - \mathbf{q}_2|^2 + \varphi), \quad (5.8)$$

where  $\mathcal{N}$  is a normalization constant,  $\mathcal{E}_p(\mathbf{q})$  is the plane wave spectrum of the pump beam, assumed to have the Gaussian profile  $\exp(-|\mathbf{q}|^2/\sigma^2)$ . The sinc func-

tion arises from phase matching,  $b^2 = L/4nk_p$ ,  $L$  is the crystal thickness,  $k_p$  is the wave number of the pump beam,  $n$  is the refractive index for the down-converted field, and  $\varphi$  is the collinear phase mismatch parameter. The adequacy of Eq. (5.8) to represent the two-photon state generated by type I SPDC has been confirmed in a number of published works. In particular, the assumption about its purity in the quasi-monochromatic regime (when narrow band frequency filters are used) is supported by the high visibilities exhibited in fourth-order interference experiments in a wide range of conditions [18, 39, 52]. In order to compare with the results published in Ref. [13], we use the notation of Law and Eberly, where  $w_p = 2/\sigma$  is the width of the Gaussian pump beam. It is not difficult to show that if  $b\sigma \ll 1$  the SPDC reduced density matrix  $\langle \mathbf{q}' | \rho_1 | \mathbf{q} \rangle = \int \Phi^*(\mathbf{q}', \mathbf{q}_2) \Phi(\mathbf{q}, \mathbf{q}_2) d\mathbf{q}_2$  leads to the factorized expression for  $\bar{\mu}^2$  characteristic of a quasi-homogeneous source, so that Eq. (5.7) holds.

The predictions of Eq. (5.7) are confirmed by a numerical calculation of the Schmidt number for SPDC based on the Schmidt decomposition of the two-photon state described by Eq. (5.8), that is,  $\Phi(\mathbf{q}_1, \mathbf{q}_2) = \sum_n \sqrt{\lambda_n} u_n(\mathbf{q}_1) v_n(\mathbf{q}_2)$ . One can show that  $K$  depends only on two parameters: the product  $b\sigma$  and the phase mismatch  $\varphi$ . We follow [13] and obtain  $K$  for different values of  $b\sigma$ . In addition, we investigate for the first time how the entanglement depends on the phase mismatch parameter  $\varphi$ . This calculation is lengthy and requires some computational power. Alternatively, we use Eq. (5.7) and immediately obtain a good approximation for the Schmidt number.

In Fig. 5.1 we compare the exact and approximated results. In Fig. 5.1(a) we keep  $\varphi = 0$  and vary  $b\sigma$  from 0.05 to 0.5. The smaller the value of  $b\sigma$ , the more the two-photon field approximates the maximally entangled state  $\delta(\mathbf{x}_1 - \mathbf{x}_2)$  and the higher is the Schmidt number. It is known that changes in the phase mismatch parameter  $\varphi$  lead to dramatic effects in the far-field intensities without any change in the near field. The Schmidt number predicted by Eq. (5.7) should change accordingly. In Fig. 5.1(b) we compare the exact and approximated results for  $K$  calculated at a fixed  $b\sigma = 0.1$  and for a wide range of the phase mismatch parameter  $\varphi$ . We conclude that Eq. (5.7) indeed provides a very good approximation to  $K$ , especially in the regime  $b\sigma \ll 1$ .

### 5.3 Measuring the Schmidt number

We demonstrate next that under the conditions assumed (pure two-photon state and quasi-homogeneous reduced one-photon state) the Schmidt number can be measured in a simple experiment. For this purpose we use the setup depicted in Fig. 5.2. Spatially entangled photon pairs are produced by type I SPDC in a 5.06 mm-thick periodically-poled  $\text{KTiOPO}_4$  crystal (PPKTP) pumped by a mildly focused Krypton laser beam ( $\lambda = 413\text{nm}$ ,  $w_p = 162\mu\text{m}$ ). After the crystal, the laser light is blocked by a filter ( $F_1$ ) and the intensity profile of the down-converted light is measured with an intensified charge coupled device (ICCD) camera. A spectral filter ( $F_2$ ) is used to select the degenerate frequency component. The detection bandwidth (5nm at 826nm) is small enough to limit spatial-spectral

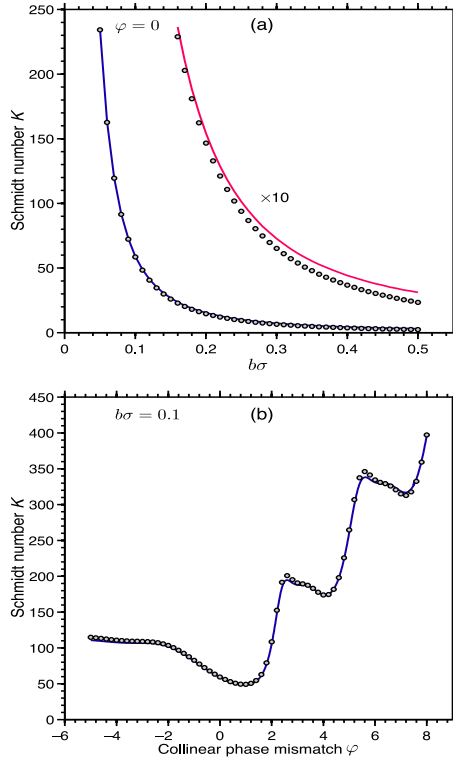


Figure 5.1: Schmidt number  $K$  obtained from Eq. (5.7) (solid line) and calculated via mode decomposition (circles). The top graph (a) shows  $K$  as a function of  $b\sigma$ , for  $\varphi = 0$ . The  $\times 10$  magnified curve shows that the approximation of Eq. (5.7) is correct to within a few percent even for  $K$  as low as 10. The bottom graph (b) shows  $K$  as a function of  $\varphi$  for  $b\sigma = 0.1$ .

correlations to an undetectable level (mismatch parameter  $\varphi$  varies  $< 0.1$  over this bandwidth [27]). Since our camera is not sensitive to photon correlations, there is no need to split the photon pairs. To measure the near field intensity, a  $12\times$  magnified image of the transverse plane at the center of the crystal is created on the detection area with a 59-mm focal-length lens ( $L_1$ ). For the far-field intensity, a f-f configuration is set up with a 100-mm focal-length lens ( $L_2$ ). The phase mismatch parameter  $\varphi$  can be adjusted by changing the temperature of the crystal. Based on the temperature dependence of the refractive indices at the pump and SPDC wavelengths, the derivative  $d\varphi/dT \approx 1.04 \text{ K}^{-1}$  around the collinear phase matching temperature  $T_0 \approx 60^\circ\text{C}$  was calculated and checked experimentally [27]. To subtract the background noise, we record, along with each measurement, a background image, taken when the polarization of the pump is rotated by  $90^\circ$ , suppressing down-conversion. The intensities in the near field and far field are measured for many different values of  $\varphi$ . After subtracting the background, we use Eq. (5.7) to estimate the Schmidt number of the two-photon

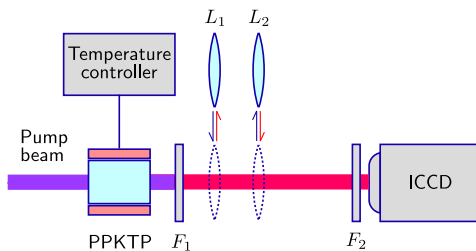


Figure 5.2: Experimental setup comprising a pumped crystal (PPKTP) and optics to create images of either the near field or the far field profile onto an intensified CCD camera (ICCD).

state.

The key experimental result of this work is depicted in Fig. 5.3. The circles represent the Schmidt number  $K$  experimentally obtained. The solid line is the theoretical prediction based on Eqs. (5.7) and (5.8) with  $b\sigma = 0.077$ . This value for  $b\sigma$  was obtained by curve fitting the near and far field intensity profiles for  $\varphi = 0$ . We observe that there is a good qualitative and quantitative agreement between theory and experiment. Even the peculiar details of the curve are reproduced experimentally. Some examples of how the angular emission pattern changes with  $\varphi$  are also shown. For larger values of  $\varphi$ , as the effective width of the transverse structure of the down-converted fields rapidly increases, the finite extent of the detection area becomes important. This finite detection area sets practical limits to the integration domains in Eq. (5.7), leading to a reduction of the detected values of  $K$ . With this correction taken into account, the theoretical prediction for the detected Schmidt number is represented by the dashed line. It should be noticed that while  $K$  may achieve very high values for  $\varphi > 0$ , the down-conversion efficiency drops significantly, due to the lack of phase matching. More precisely, the overall photon flux  $F(\varphi)$  relative to its  $\varphi = 0$  value is given by  $F(\varphi)/F(0) = 1 + (2/\pi)[\varphi \operatorname{sinc}^2\varphi - \operatorname{Si}(2\varphi)]$ , where  $\operatorname{Si}(x) = \int_0^x \operatorname{sinc} x' dx$  is the sine integral function. For example,  $F(4)/F(0) \approx 0.09$  and  $F(8)/F(0) \approx 0.04$ .

The results in Fig. 5.3 can be qualitatively explained as follows. For negative phase mismatch ( $\varphi < 0$ ) the amount of entanglement does not depend strongly on  $\varphi$ . This is because the SPDC far-field is concentrated in a “ring” whose area is practically independent of the radius. Around  $\varphi = 0$ , the ring collapses into a central spot of smaller area, reducing the ratio in Eq. (5.7). At  $\varphi \approx 1$  the central peak resembles a Gaussian and  $K$  reaches its minimum value. For  $\varphi > 1$ , the main ring completely disappears, and the weaker, secondary peaks of the sinc function lead to a more spread intensity distribution, rapidly increasing the value of  $K$ . As  $\varphi$  increases, the effective width of the far-field intensity profile keeps increasing, oscillating with  $\varphi$  due to rearrangements in the rings structure, thus leading to oscillations in the value of  $K$ .

Finally, we interpret the product of the ratios in Eq. (5.7) taken at the near and far field, as the product of an effective “object” area  $A_{\text{eff}}$  (near field) and an

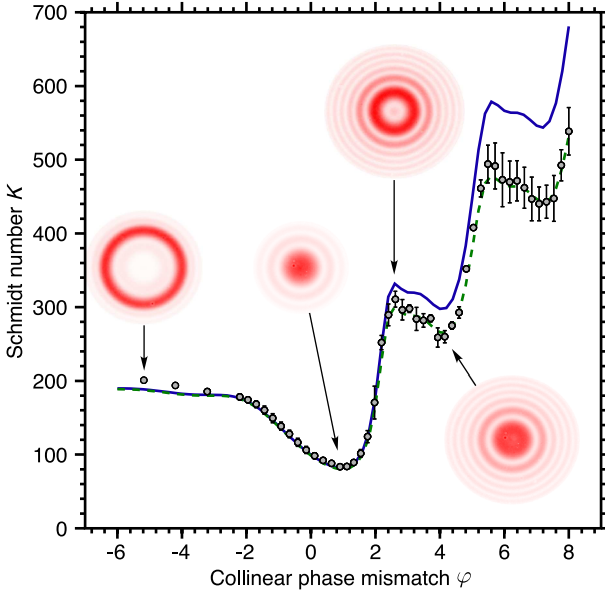


Figure 5.3: Experimental results (circles), theoretical prediction for infinite detection area (solid line), and theoretical prediction corrected for the finite size of the detection area (dashed line). Some of the measured far-field intensity profiles are shown.

effective emission angle  $\Omega_{\text{eff}}$  (far field) via

$$K = \frac{1}{\lambda^2} A_{\text{eff}} \Omega_{\text{eff}}. \quad (5.9)$$

The same formula is known in classical optics as the *optical étendue* or the *Shannon number* of an image or imaging system. The product  $A_{\text{eff}} \Omega_{\text{eff}} / \lambda^2$  defines the number of independent classical communication channels available to the optical system. We provide, in this way, support to the recently proposed relation between two-photon spatial entanglement and the Shannon dimensionality of quantum channels [103]. Needless to say, this association is valid for the conditions assumed here: pure two-photon states with quasi-homogeneous reduced one-photon states.

## 5.4 Conclusion

In conclusion, we reported the first measurement of entanglement in an infinite-dimensional space. We proved that the Schmidt number of the transverse-mode entanglement of a two-photon field is identical to the inverse of the overall degree of coherence of the source. The theoretical framework based on the coherence theory indicates, contrary to what is usually assumed, that the amount of spatial

entanglement can be experimentally estimated in a straightforward way.

## Appendix A: Approach based on the Wigner function formalism

The coherence properties of the partially coherent one-photon field can be alternatively represented in the phase space. The Wigner distribution function provides a way of describing the spatial (near field) and directional (far field) representations simultaneously [102]. This is closely related to the ray concept in optics, in which the position and direction of a ray are simultaneously given. The Wigner function of a stochastic field is defined in terms of the coherence function by

$$F(\boldsymbol{\rho}, \mathbf{u}) = \int W \left( \boldsymbol{\rho} + \frac{1}{2}\boldsymbol{\rho}', \boldsymbol{\rho} - \frac{1}{2}\boldsymbol{\rho}' \right) \exp(-i\mathbf{u} \cdot \boldsymbol{\rho}') d\boldsymbol{\rho}'. \quad (5.10)$$

The positional intensity (near field) can be directly obtained by integrating the Wigner distribution over all directions,

$$I(\boldsymbol{\rho}) = \frac{1}{(2\pi)^2} \int F(\boldsymbol{\rho}, \mathbf{u}) d\mathbf{u}, \quad (5.11)$$

while the directional intensity (far field) can be obtained by integrating the Wigner distribution over all positions,

$$J(\mathbf{u}) = \int F(\boldsymbol{\rho}, \mathbf{u}) d\boldsymbol{\rho}. \quad (5.12)$$

One advantage of making use of this representation is that both the sum of the eigenvalues  $\lambda_i$  and the sum of the squared eigenvalues  $\lambda_i^2$  are given by simple integrals over  $F(\boldsymbol{\rho}, \mathbf{u})$ , namely,

$$\frac{1}{(2\pi)^2} \iint F(\boldsymbol{\rho}, \mathbf{u}) d\boldsymbol{\rho} d\mathbf{u} = \sum_i \lambda_i, \quad (5.13)$$

$$\frac{1}{(2\pi)^2} \iint F^2(\boldsymbol{\rho}, \mathbf{u}) d\boldsymbol{\rho} d\mathbf{u} = \sum_i \lambda_i^2. \quad (5.14)$$

As we have seen, the two-photon field generated by SPDC has a special form, factorizing in two functions of the sum and difference coordinate

$$A(\boldsymbol{\rho}_1, \boldsymbol{\rho}_2) = \xi \left( \frac{\boldsymbol{\rho}_1 + \boldsymbol{\rho}_2}{2} \right) V \left( \frac{\boldsymbol{\rho}_1 - \boldsymbol{\rho}_2}{2} \right), \quad (5.15)$$

where  $\xi(\boldsymbol{\rho})$  is the transverse field profile of the pump beam and  $V(\boldsymbol{\rho})$  is the spatial representation of the phase-matching function. Both functions are circularly symmetric, i.e., depend only on  $|\boldsymbol{\rho}|$ . The one-photon coherence function can be

obtained by taking the partial trace with respect to the other photon, yielding

$$W(\boldsymbol{\rho}_1, \boldsymbol{\rho}_2) = \int A^*(\boldsymbol{\rho}_1, \boldsymbol{\rho}) A(\boldsymbol{\rho}, \boldsymbol{\rho}_2) d\boldsymbol{\rho}. \quad (5.16)$$

The coordinates  $\boldsymbol{\rho}_1$  and  $\boldsymbol{\rho}_2$  represent now the two transverse spatial positions in which the one-photon coherence function is being considered. By substituting Eq. (5.15) in Eq. (5.16), and then into Eq. (5.10), one can show, after a suitable change of variables, that the Wigner distribution function for the one-photon field is

$$F(\boldsymbol{\rho}, \mathbf{u}) = \left| \int \xi \left( \frac{\boldsymbol{\rho}'}{2} \right) V \left( \frac{\boldsymbol{\rho}'}{2} - \boldsymbol{\rho} \right) \exp(-i\boldsymbol{\rho}' \cdot \mathbf{u}) d\boldsymbol{\rho}' \right|^2. \quad (5.17)$$

In the vast majority of experimental realizations the phase-matching profile  $V$  is much narrower than the pump profile  $\xi$  in the near field. Since the pump profile  $\xi$  varies slowly around  $\boldsymbol{\rho}'/2 = \boldsymbol{\rho}$ , where  $V$  is centered, we can bring the contribution of  $\xi$  out of the integral\*. The Wigner distribution simplifies to

$$F(\boldsymbol{\rho}, \mathbf{u}) = |\xi(\boldsymbol{\rho})|^2 \times \left| \int V \left( \frac{\boldsymbol{\rho}'}{2} \right) \exp(-i\boldsymbol{\rho}' \cdot \mathbf{u}) d\boldsymbol{\rho}' \right|^2. \quad (5.18)$$

The second term is nothing more than the Fourier transform of the spatial representation of the phase-matching conditions, which is the 'sinc'-type angular spectrum. The Wigner function is thus separated in a product of near-field and far field-intensities as

$$F(\boldsymbol{\rho}, \mathbf{u}) = 16 |\xi(\boldsymbol{\rho})|^2 \times \left| \tilde{V}(2\mathbf{u}) \right|^2. \quad (5.19)$$

This result is consistent with what one would expect: in the near field the single-photon intensity reproduces the pump profile, while in the far field it reveals the well known SPDC rings. Using Eqs. (5.13), (5.14), and (5.19), the Schmidt number can then be estimated by

$$K = \frac{1}{(2\pi)^2} \frac{\left[ \int |\xi(\boldsymbol{\rho})|^2 d\boldsymbol{\rho} \right]^2}{\int |\xi(\boldsymbol{\rho})|^4 d\boldsymbol{\rho}} \times \frac{\left[ \int |\tilde{V}(2\mathbf{u})|^2 d\mathbf{u} \right]^2}{\int |\tilde{V}(2\mathbf{u})|^4 d\mathbf{u}}. \quad (5.20)$$

The transverse wave vector  $\mathbf{u}$  is related to the far-field angles via  $\mathbf{u} = \frac{2\pi}{\lambda} \boldsymbol{\theta}$ . Eq. (5.20) can be rewritten as a function of the measured intensities, recovering Eq. (5.7)

$$K = \frac{1}{\lambda^2} \frac{\left[ \int I_s(\boldsymbol{\rho}) d\boldsymbol{\rho} \right]^2}{\int I_s^2(\boldsymbol{\rho}) d\boldsymbol{\rho}} \times \frac{\left[ \int I_{FF}(\boldsymbol{\theta}) d\boldsymbol{\theta} \right]^2}{\int I_{FF}^2(\boldsymbol{\theta}) d\boldsymbol{\theta}}. \quad (5.21)$$

\* We consider the "near-field" as the region *close to* the exit facet of the crystal. As we have seen in Chapters 2 and 3, the phase-matching function is always narrow peaked at the crystal facet, what justifies this passage even for non-zero phase mismatch.

# 6

## Orbital angular momentum spectrum of entangled two-photon states

We implement an interferometric method to measure the orbital angular momentum (OAM) spectrum of photon pairs generated by spontaneous parametric down-conversion. In contrast to previous experiments, which were all limited by the modal capacity of the detection system, our method operates on the entire down-conversion cone and reveals the complete distribution of the generated OAM. In this geometry, new features can be studied. We show that the phase-matching conditions can be used as a tool to enhance the azimuthal Schmidt number and to flatten the spectral profile, allowing the efficient production of high-quality multidimensional entangled states.

H. Di Lorenzo Pires, H. C. B. Florijn, and M. P. van Exter, *Measurement of the Spiral Spectrum of Entangled Two-Photon States*, Phys. Rev. Lett. **104**, 020505 (2010).

## 6.1 Introduction

It is now recognized that the use of larger alphabets in quantum information processing brings possible advantages over multiple qubit schemes [104]. However, from the experimental point of view, the generation of quantum states exhibiting controllable and detectable multidimensional entanglement is still in its first stages of development. Of particular interest is the generation of photon pairs entangled in orbital angular momentum (OAM). The discrete nature of the underlying infinite dimensional Hilbert space and the limited sensitivity of photonic states to environmental noise make them strong candidates as carriers of quantum information. Experimentally, two-photon states entangled in OAM can be generated via the nonlinear process of spontaneous parametric down conversion (SPDC). Since the existence of quantum OAM correlations between photon pairs was first demonstrated [105], an increasing effort is being devoted to manipulate and measure these states. This includes violations of bipartite Bell inequalities [106,107], the enhancement of OAM entanglement via concentration [108], and an implementation of a quantum coin-tossing protocol [109].

In this context, a full characterization of the OAM correlations is essential. The main question we want to address experimentally is: what is the precise form of the OAM spectra of down-converted photons? In other words: what are the relative weights  $P_l$  of different  $l$  modes, where  $l$  represents the photon topological winding number? The width of such modal expansion, denominated by Torres *et al.* [110,111] as *quantum spiral bandwidth*, is directly related to the amount of entanglement. Full knowledge of the OAM spectra allows one to inspect the quality of the entangled state and to determine whether the distribution of  $l$  modes is broad enough as compared to the channel capacity, which is essential to some protocols [103].

It is important to note that all previous experiments on OAM analysis [105,112,113] were limited by the modal capacity of the detection geometry and did not measure the true spectrum of the *generated* two-photon states. For instance, in Ref. [112] an azimuthal Schmidt number of  $K_{az} = 7.3$  was measured, while one would expect  $K_{az} = 51.7$  based on the experimental parameters. The reason for this discrepancy is that only light within small angular sections around diametrically opposed regions of the SPDC cone were collected. This scheme not only discards most of the wavefunction, but also conceals the importance of the phase-matching conditions to the OAM spectrum. Furthermore, as we will argue, it is also fundamentally impossible to measure pure OAM correlations by using mode projections with holograms or phase plates and single mode fibers, as this configuration is also sensitive to radial field distributions of source and detectors (related to the mode number  $p$ ). These are the main reasons why the outcome of previous works could not be directly compared with predictions of the well-known SPDC wavefunction. It has been recognized in the literature that [114,115] “an experiment aimed at detecting the *global* OAM of the down-converted photons is a significant challenge that it is yet to be solved”. In this Chapter we will present such an experiment. We measure, for the first time, the complete

OAM spectrum of the source. Additionally, we show how to efficiently extend the range of entangled modes via phase matching.

## 6.2 The OAM spectrum of SPDC

We consider SPDC emission along a principal axis of a birefringent non-linear crystal pumped by a Gaussian beam. In this so-called non-critical phase-matching geometry, transverse walk-off can be neglected. Generalizations to other geometries will be given at the end of this Chapter. For non-critical (type I and type II) SPDC the two-photon wave function in momentum representation is well known and assumes the form [19,31]

$$A(\mathbf{q}_s, \mathbf{q}_i) = \tilde{E}(\mathbf{q}_s + \mathbf{q}_i) \operatorname{sinc} \left( \frac{L}{8k} |\mathbf{q}_s - \mathbf{q}_i|^2 + \varphi \right), \quad (6.1)$$

where  $\tilde{E}(\mathbf{q})$  is the angular spectrum of the (Gaussian) pump beam,  $L$  is the crystal thickness,  $k = 2\pi/\lambda$  is the wave vector of the generated light in the crystal, and  $\mathbf{q}_{s,i}$  are the transverse components of the signal and idler wavevectors. Additionally, this function contains the collinear phase mismatch  $\varphi$ , which is also relevant in the forthcoming analysis. We can make use of polar coordinates  $\mathbf{q}_\alpha = (q_\alpha \cos \theta_\alpha, q_\alpha \sin \theta_\alpha)$ , with  $\alpha = s, i$ , in order to separate the azimuthal and radial contributions. The rotation symmetry of Eq. (6.1) allows one to decompose the two-photon amplitude in the form [13]  $A(\mathbf{q}_s, \mathbf{q}_i) = \sum_l \sqrt{P_l} e^{il(\theta_s - \theta_i)} F_l(q_s, q_i)/2\pi$ . In order to access exclusively the azimuthal dependence of the field two requirements should be met. First, all the light must be collected by the detection scheme and second, one must use *bucket*, i.e., mode insensitive, detectors. This assures that the radial dependence will be completely integrated out as  $\iint |F_l(q_s, q_i)|^2 q_s q_i dq_s dq_i = 1$ . Naturally, this requirement is not satisfied when the state is spatially filtered or when a coherent detection scheme is used. Considering only the azimuthal dependence, the nature of the OAM correlations can thus be expressed in the entangled state  $|\psi\rangle = \sum_{l=-\infty}^{+\infty} \sqrt{P_l} |l\rangle_s |-l\rangle_i$ , where  $P_l$  is the probability of finding a *signal* photon with orbital angular momentum  $l$  and an *idler* photon with  $-l$ . It is important to stress once again that this decomposition refers to the whole generated state. The distribution of  $P_l$ , which we call the OAM spectrum of the two-photon field, is precisely the quantity we want to measure.

Fig. 6.1 illustrates our experimental setup. It consists basically of a Mach-Zehnder interferometer with an image rotator inserted in one of its arms. It has been theoretically shown that such arrangement can be used to measure the OAM spectrum of an *one-photon* field in a superposition of  $l$  modes [116,117]. We will generalize the concept and argue that it can also be used to reveal the OAM spectrum of entangled two-photon states. Here, the visibility of a Hong-Ou-Mandel (HOM) interference as a function of the angle of rotation, in a collection geometry that does not constrain the photon wave vectors [118], will provide the necessary information.

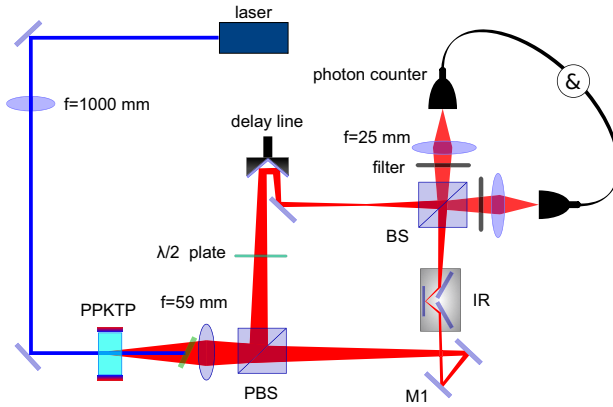


Figure 6.1: Experimental setup used to generate entangled two-photon pairs and to measure its OAM spectrum. See details in the text.

The effect of the interferometer on the state  $|\psi\rangle$  can be summarized as follows: The two photons (generated with orthogonal polarizations in type-II SPDC) are separated at a polarizing beam splitter (PBS). The transmitted photon acquires an extra phase  $e^{il\theta}$  due to the presence of an image rotator (IR). This home-made device is similar to a Dove prism, but consists of three mirrors instead. It offers the advantage that it can be more precisely aligned, so that the output beam moves less than  $30 \mu\text{m}$  in position and less than  $150 \mu\text{rad}$  in angle (see Ref. [112] for more information about our device). It is essential that one photon is reflected an even number of times and the other an odd number of times. If the interferometer is balanced, its output state, post-selected on coincidences, is  $|\psi_{out}\rangle \propto \sum_l \sqrt{P_l} (e^{il\theta} - e^{-il\theta}) |l\rangle_1 |l\rangle_2$ . Notice that due to the uneven number of reflections, both photons have the same OAM index  $l$  at the output. The measured coincidence counts is given by  $R_{cc} \propto \langle \psi_{out} | \psi_{out} \rangle$ . The corresponding visibility of the HOM-like interference will depend on the rotation angle  $\theta$  and is given by  $V(\theta) = 1 - R_{cc}^{\tau=0} / R_{cc}^{\tau=\infty}$ , where  $\tau$  denotes the time delay between the two arms of the interferometer. One can show that

$$V(\theta) = \sum_{l=-\infty}^{+\infty} P_l \cos(2l\theta). \quad (6.2)$$

By measuring this visibility as a function of  $\theta$  we can recover the weights  $P_l$  via inverse Fourier transform.

### 6.3 Experiments and discussions

Entangled photon pairs are obtained via type-II SPDC by pumping a 2-mm thick periodically poled KTP crystal (PPKTP) with a krypton-ion laser beam ( $\lambda_p =$

413.1 nm,  $w_p = 150 \mu\text{m}$ ). The pump is blocked by an AR-coated GaP wafer. A  $f = 59 \text{ mm}$  lens is used to make a  $13\times$  magnified image of the SPDC light in the center of the image rotator; this image is then demagnified by  $1/19\times$  and focused by two  $f = 25 \text{ mm}$  lenses onto the active area of two photon counting modules. The polarization of the photon reflected by the PBS is rotated by a  $\lambda/2$  plate in order to allow interference at the second beam splitter (BS). Spectral filters (2 nm at 826.2 nm) are used to select photons close to frequency degeneracy.

The experiment consists of measuring the HOM visibility for various angles  $\theta$ . We do this by measuring, for each angle, the coincidence counts inside the HOM dip and then the coincidence counts outside the HOM dip, by imposing a time delay  $\tau = 1.7 \text{ ps}$ . The setup is fully automated. When  $\theta = 0^\circ$  we expect a visibility  $V = 100\%$ , but measure at most  $V = 80\%$ . This discrepancy occurs because for type-II SPDC with 2 nm bandwidth filters, the combined spatial-spectral profile of the photons still contains some “which-path” information. In the presented data we will compensate for it by normalizing the maximum measured visibility to 1. This renormalization is allowed because the combined spatial-spectral labeling involves only the radial coordinates of the field, and not the azimuthal. The use of even narrower band interference filters would eliminate this effect.

Figure 6.2(a) shows the measured (normalized) visibility obtained with the 2-mm PPKTP at perfect phase matching ( $\varphi = 0$ ). The dots are the experimental results and the curve the theoretical prediction. Notice the excellent agreement between the two curves; no fitting parameters are needed. The curve is obtained by substituting the theoretical probabilities  $P_l^{th}$  in Eq. (6.2). These probabilities can be numerically obtained by performing a Schmidt decomposition [13,110] of the two-photon amplitude of Eq. (6.1).

Figure 6.2(b) shows the measured OAM spectrum of the two-photon field. The bars are the experimental values, obtained via a discrete Fourier transform of the visibility in Fig. 6.2(a), and the dashed curve is the theoretical  $P_l^{th}$ . Predictions for the mode distributions are also present in Ref. [110] as a function of the parameter  $\bar{w}_p = w_p/\sqrt{\lambda_p L}$ . We experimentally confirm the predictions therein, at an experimental value of  $\bar{w}_p = 5.2$ .

Having the OAM spectral distribution, we can quantify the amount of entanglement present using the azimuthal Schmidt number  $K_{az}$ , defined as  $K_{az} = 1/\sum_l P_l^2$ . We obtain  $K_{az}^{ex} = 21.4 \pm 0.5$ , while the theoretical value is  $K_{az}^{th} = 21.6$ . In both computations we included  $l$  modes up to  $|l| = 70$ , where  $P_l < 10^{-4}$ .

It has been predicted in the literature that using pump beams with more complex spatial structures [119] or engineering the transverse structure of periodically-poled crystals [120] may lead to an increased Schmidt number. Here we will take an alternative route and show how the manipulation of the phase-matching conditions may lead to the efficient generation of high-quality entangled states. The phase-mismatch parameter  $\varphi$  can be controlled experimentally by simply changing the temperature of the crystal. To further explore this effect we will switch to type-I SPDC, because our type-II crystals otherwise had to be operated below  $T=0^\circ\text{C}$ . We change the PBS by a BS, remove the  $\lambda/2$  plate, and change mirror M1 to a piezo-driven mirror. The latter allows us to remove during

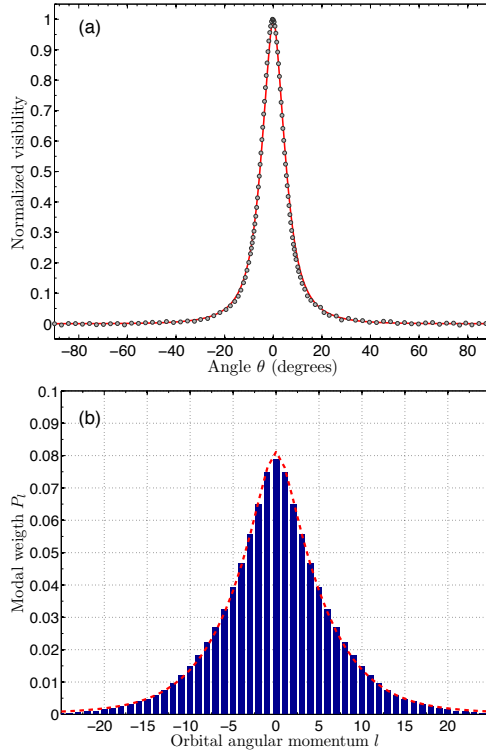


Figure 6.2: (a) Normalized visibility of the HOM interference as a function of the rotation angle for a 2-mm crystal. The dots are experimental results and the curve the theoretical calculation. (b) Corresponding OAM spectrum obtained via Fourier transform. The bars are the experimental results and the curve is the theoretical expectation. Notice the excellent agreement, where no fitting parameters are used.

the measurements the additional interference fringes, on top of the HOM dip, that would otherwise be present (see Ref. [121] for details). All other parameters are unchanged, except for the thickness of the crystal. We now use a 5-mm type-I PPKTP. Repeating the measurements at perfect phase matching ( $\varphi=0$ ) we obtain an azimuthal Schmidt number of  $K_{az}^{ex} = 13.8 \pm 0.5$ , while the theoretical  $K_{az}^{th} = 13.9$ , in agreement with the expected scaling  $K_{az} \propto 1/\sqrt{L}$ .

Next, we explore the effect of phase mismatch on the Schmidt number, especially for  $\varphi < 0$ , where the SPDC rings are open and the pair-generation process is almost twice as efficient. For this crystal  $\varphi = 1.04 \times (T - T_0)$ , where  $T_0$  is the crystal temperature for perfect phase matching.

Figure 6.3 shows both the experimental values and the theoretical curve for  $K_{az}$  as a function of  $\varphi$ . The error bars are obtained by repeating the experiment, including realignment of the setup. We have thus demonstrated that the phase matching conditions can be used to boost the Schmidt number. But what is the

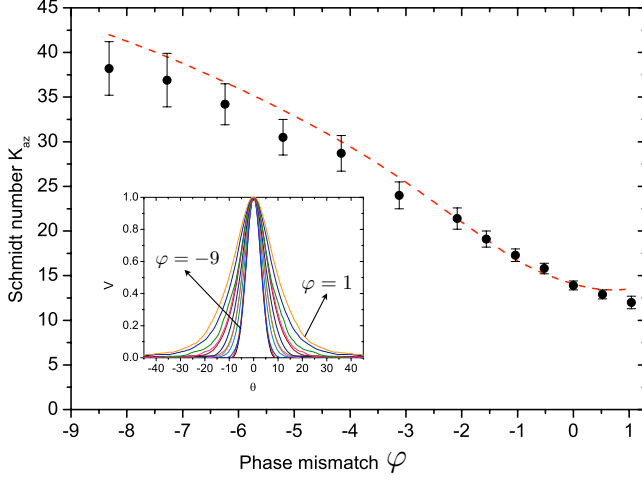


Figure 6.3: Dependence of the azimuthal Schmidt number  $K_{az}$  on the phase mismatch parameter  $\varphi$  for a 5-mm crystal. The inset shows the measured visibilities, where the inner curve (at  $\varphi = -9$ ) corresponds to the highest  $K_{az}$ .

effect on the OAM spectrum?

Figure 6.4 shows how the modal decomposition changes for four values of  $\varphi$ . We see that for more negative values of  $\varphi$  the spectral profile tends to flatten, which leads to higher values of  $K_{az}$ . In the range considered ( $|l| \leq 10$ ), the quality of the entangled state is such that it virtually eliminates the need for an entanglement *concentration* protocol [108,122]. This is important because most of the potential applications of quantum entanglement work best for maximally-entangled states. Phase mismatch therefore not only extends the range of useful  $l$  modes in practical applications, allowing larger alphabets, but can also increase the conversion efficiency.

Finally, we would like to discuss two possible extensions of our approach, which applied to a rotationally symmetric pump in a non-critical geometry. First, one could use also a pump beam with  $l_p \neq 0$ , for which the down-converted state assumes the form  $\sum_l \sqrt{P_l} |l\rangle |l_p - l\rangle$ , where  $P_l = P_{l_p - l}$ . The complete OAM spectrum can again be determined from the measured visibility  $V(\theta) = \sum_l P_l \cos[(l_p - 2l)\theta]$ . Alternatively, one could also generate SPDC light in configurations where the OAM is not necessarily conserved [123–125]. If one wants to probe the most general state  $\sum_{l,k} \sqrt{C_{l,k}} |l\rangle |k\rangle$ , modifications of the setup are necessary. One now first needs to separate the two-photons in a PBS before sending each photon to its own (one-photon) Mach-Zehnder interferometer with IR [117]. Measurements of coincidences between the output ports of the two interferometers will now provide the visibility  $V(\theta_1, \theta_2)$ . A double Fourier transformation is enough to recover  $C_{l,k}$ .

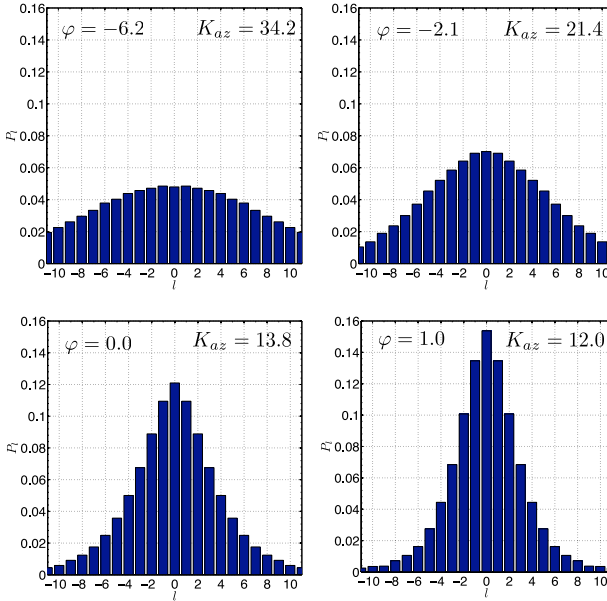


Figure 6.4: The effect of phase mismatch on the modal decomposition  $P_l$ . For negative  $\varphi$  the SPDC rings are open and the pair generation is more efficient. By adjusting the phase-matching conditions we can increase the Schmidt number and flatten the spectral profile, producing high-quality entangled states in a larger  $l$  range.

## 6.4 Conclusion

In conclusion, we have reported measurements of OAM spectra of entangled photon pairs generated by SPDC. This is, to the best of our knowledge, the first experiment where the entire down-converted cone is considered and where the detection geometry does not shape the spectrum nor limits its dimensionality  $K_{az}$ . By combining an interferometric technique with bucket detectors our method can access the pure OAM correlations, i.e., without coupling azimuthal  $l$  with radial  $p$  modes. Our results can be directly confronted with the theoretical predictions for the generated state in SPDC. We found an excellent agreement between our experimental results and the predicted Schmidt decomposition. Furthermore, we have shown how the phase-matching conditions can be used as a tool to efficiently boost the Schmidt number, flatten the spectral profile, and virtually eliminate the need of entanglement concentration operations. Our experimental implementation can be generalized to measure OAM correlations of pure bipartite states of the most general form.

# 7

## Orbital angular momentum spectrum of partially coherent classical beams

In this work we implement a Mach-Zehnder interferometer with an image rotator in one of its arms to measure the orbital angular momentum (OAM) spectrum of a partially coherent beam. By measuring the visibility of the interference as a function of the angle of rotation, the OAM distribution can be recovered via a Fourier transform. Theoretical calculations based on the coherent mode decomposition of the cross-spectral density are in excellent agreement with the experimental data.

H. Di Lorenzo Pires, J. Woudenberg, and M. P. van Exter, *Measurement of the orbital angular momentum spectrum of partially coherent beams*, *Opt. Lett.* **35**, 889 (2010).

## 7.1 The OAM spectrum of partially coherent beams

It is well known that light can carry orbital angular momentum (OAM). In particular, coherent beams with an azimuthal phase dependence in the form  $e^{il\phi}$ , have an OAM of  $l\hbar$  per photon [126]. Recently, the concept of OAM was generalized in order to encompass partially coherent light as well [127–131]. One can consider, for instance, beams that can be constructed from an incoherent superposition of Laguerre-Gaussian modes of arbitrary order, but with the same azimuthal index [127, 128]. Serna and Movilla [129] extended the considerations to a more general family of fields, and the relation between the twist of the beam and the OAM was analyzed. However, even in the more typical case of a partially coherent beam that does not transport an overall OAM, we can describe it statistically as a sum of completely coherent beams with a well defined OAM. This description can be formalized by means of the coherent mode decomposition (or Mercer expansion) [3] of the cross-spectral density function  $W(\boldsymbol{\rho}_1, \boldsymbol{\rho}_2)$  that completely describes the source. For a rotationally symmetric geometry, this decomposition reads

$$W(\boldsymbol{\rho}_1, \boldsymbol{\rho}_2) = \sum_{l=-\infty}^{+\infty} \sum_{p=0}^{\infty} \lambda_{l,p} f_{l,p}(\boldsymbol{\rho}_1) f_{l,p}^*(\boldsymbol{\rho}_2) \frac{e^{il(\phi_1 - \phi_2)}}{2\pi}, \quad (7.1)$$

where the transverse position vector  $\boldsymbol{\rho} = (\rho \cos \phi, \rho \sin \phi)$  is written in polar coordinates. This representation is very fundamental, being equivalent to a matrix diagonalization or the search for the eigenvalues  $\lambda_{l,p}$  and the eigenfunctions  $f_{l,p}(\boldsymbol{\rho})$ . Physically, it reveals the modal structure of the source and  $\lambda_{l,p}$  can be interpreted as the probability of finding a coherent mode  $f_{l,p}$ . The larger the number of modes present, the more incoherent is the source. This implies that Eq. (7.1) would contain only one term for a completely coherent (e.g. a laser) beam. This decomposition is also crucial to OAM analysis of partially coherent light [129, 132] and allows us to assign a probability  $P_l = \sum_p \lambda_{l,p}$  of having a mode with OAM  $l\hbar$ .

The distribution of the probabilities  $P_l$  is known as the OAM spectrum of the beam. To the best of our knowledge, no measurements of this spectrum for partially coherent light have been reported so far. In this Chapter we will present such an experiment. We will implement an approximately quasi-homogeneous light source [133], justifying the expansion in Eq. (7.1). The intrinsic symmetry  $P_l = P_{-l}$  implies that the beam carries no overall OAM. Generalizations will be discussed at the end of this Chapter.

## 7.2 Experiments and discussions

Figure 7.1 shows the experimental setup used to generate a partially coherent beam and to measure its OAM spectrum. A  $15\times$  magnified image of a light emitting diode (LED) is made on an adjustable circular aperture of diameter  $d_1$ , after being filtered by a polarizer. We can regard this aperture as an incoherent, circular source of uniform intensity. The light propagates a distance  $L$  to a second

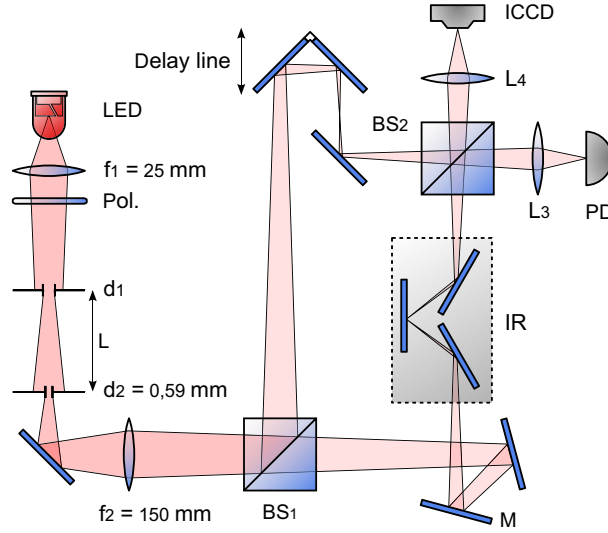


Figure 7.1: Experimental setup used to create a partially coherent beam and to measure its OAM spectrum. See details in the text.

circular aperture of fixed diameter  $d_2$ . Using the van Cittert-Zernike theorem [2], the cross-spectral density of the beam just after the second aperture is given by

$$W(\boldsymbol{\rho}_1, \boldsymbol{\rho}_2) = T(\boldsymbol{\rho}_1)T(\boldsymbol{\rho}_2) \frac{J_1(\alpha|\boldsymbol{\rho}_1 - \boldsymbol{\rho}_2|)}{\alpha|\boldsymbol{\rho}_1 - \boldsymbol{\rho}_2|} e^{\frac{i\pi}{\lambda L}(\rho_1^2 - \rho_2^2)}, \quad (7.2)$$

where  $T(\rho)$  is the transmission function of the second aperture,  $J_1(\rho)$  is a Bessel function of the first kind, and  $\alpha = \pi d_1 / \lambda L$ . The wavelength  $\lambda$  is defined by spectral filters in front of our detection units, which are centered at 826 nm and have 2 nm bandwidth.

From Eq. (7.2), the  $P_l$  distribution can be analytically calculated. The Gegenbauer theorem [134] can be used to separate the radial and angular dependence of the term containing the Bessel function in Eq. (7.2), which can then be written in a series of functions of  $\rho_1$  and  $\rho_2$  times  $e^{il(\phi_1 - \phi_2)}$ . Omitting the details, we can integrate out the modulus squared of the radial dependence and express the OAM spectrum, apart from a global normalization factor, as

$$P_l = \sum_{i=0}^k \sum_{j=0}^k (1 + |l| + 2i)(1 + |l| + 2j) \times [\mathbb{H}(\alpha d_2/2, 1 + |l| + 2i, 1 + |l| + 2j)]^2, \quad (7.3)$$

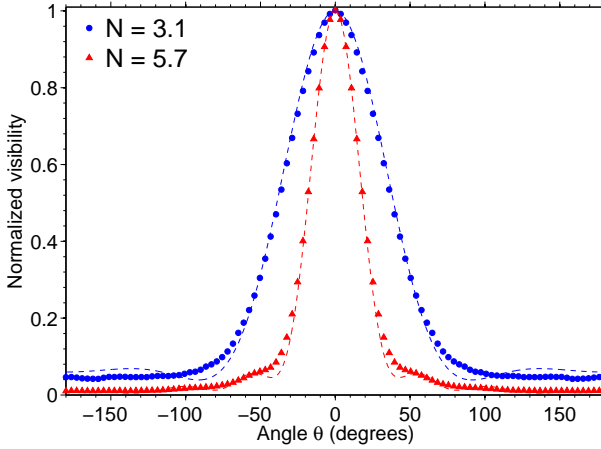


Figure 7.2: Measured visibility  $V(\theta)$  for two different circular apertures. The circles corresponds to a diameter  $d_1 = 1.2$  mm ( $N = 3.1$ ) and the triangles to  $d_1 = 2.2$  mm ( $N = 5.7$ ). The dashed lines are the theoretical curves, calculated by substituting  $P_l$  from Eq. (7.3) in Eq. (7.5).

where the function  $\mathbb{H}$  is defined as

$$\mathbb{H}(\gamma, m, n) = \frac{2^{-m-n}\gamma^{m+n}}{m!n!(m+n)} {}_2F_3 \left[ \left\{ \frac{m+n}{2}, \frac{m+n+1}{2} \right\}, \{1+m, 1+n, 1+m+n\}, -\gamma^2 \right], \quad (7.4)$$

and  ${}_2F_3$  is a generalized hypergeometric function [135]. The summations in Eq. (7.3), which are associated with the radial mode index  $p$ , go in principle up to  $k = +\infty$ , but numerically, using  $k = 5$  gives an error less than 0.5% for our particular values. We see from Eq. (7.3) that the generated sources can be conveniently characterized by a single, dimensionless Fresnel-type number  $N = \pi d_1 d_2 / 4\lambda L$ . For our geometry with  $L = 21$  cm,  $\lambda = 826$  nm, and fixed  $d_2 = 0.59$  mm, the investigated apertures  $d_1 = 1.2$  mm and  $d_1 = 2.2$  mm correspond to  $N = 3.1$  and  $N = 5.7$ .

In order to measure the  $P_l$  distribution, we implement an apparatus similar to the one theoretically proposed by Zambrini and Barnett [136]. The generated beam is sent through a Mach-Zehnder interferometer, where it is initially split in beam splitter BS1 and then recombined at BS2. In one of the arms of this interferometer there is an image rotator (IR), which rotates the input image by  $\theta$  degrees around its axis. A  $f = 150$  mm lens makes a  $4\times$  magnified image of the second aperture in the center of the IR. A delay line allows us to set both arms of the interferometer to the same length. All the light in one of output ports of BS2 is collected with lens L3 and focused on the active area of a photodiode (PD).

We can summarize the effect of the interferometer as follows. Consider first a pure (coherent) beam with OAM =  $l\hbar$ . Light that goes through the lower arm of the interferometer will acquire a phase  $e^{il\theta}$  due to an image ro-

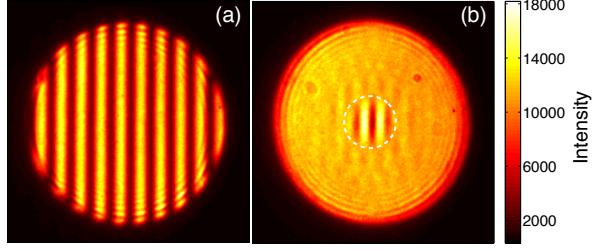


Figure 7.3: Measured interference pattern for (a)  $\theta = 0^\circ$  and (b)  $\theta = 180^\circ$ . Beam splitter BS2 was on purpose misaligned in order to allow the visualization of vertical fringes. The dashed line delimits the theoretical coherence area.

tation of  $\theta$  and  $e^{i\delta}$  due to a small displacement of the piezo-controlled mirror  $M$ . The intensity of the recombined beams as measured by the PD is then  $I \propto |e^{i\phi} + e^{i(\phi+l\theta+\delta)}|^2 \propto 1 + \cos(l\theta + \delta)$ . For an incoherent superposition of beams with OAM= $l\hbar$  with probability  $P_l$  (satisfying  $P_l = P_{-l}$ ), the intensity measured is then  $I \propto 1 + V(\theta) \cos \delta$ , where the visibility of the total interference

$$V(\theta) = \sum_{l=-\infty}^{l=+\infty} P_l \cos(l\theta) \quad (7.5)$$

can be measured in the standard way, by producing small displacements with mirror  $M$  and calculating  $V = (I_{max} - I_{min}) / (I_{max} + I_{min})$ . The OAM spectrum  $P_l$  can thus be recovered by measuring  $V(\theta)$  and numerically performing an inverse Fourier transform. For  $\theta = 0^\circ$ , the visibility should be theoretically  $V = 100\%$ . Experimentally we obtain  $V = 90\%$ . We attribute this discrepancy to an almost unavoidable non-perfect overlap of the phase fronts at the BS2. All our results will be normalized to account for this effect.

Figure 7.2 shows the measured visibility  $V(\theta)$  for two different diameters  $d_1$  of the first aperture. We see that a smaller aperture leads to a broader visibility curve, in agreement with the theoretical curves.

The physical reason why the visibility decreases with rotation can be visualized in Fig. 7.3. We now misalign BS2, so that fringes can be observed, and record the interference pattern with an intensified CCD camera (ICCD). Figure 7.3(a) shows the measured pattern for  $\theta = 0^\circ$  and Fig. 7.3(b) for  $\theta = 180^\circ$ . When we superpose the rotated field, points with a larger radius suffer also a larger linear displacement  $|\rho_1 - \rho_2| = 2\rho \sin(\theta/2)$ . The lack of spatial coherence between these points leads to a decreased fringe visibility. We see that the visibility of the interference remains high within a certain radius, which is related to the coherence length of the field. This is confirmed by plotting in Fig. 7.3(b) the theoretical boundaries of the coherence area, as defined by the first zero of Eq. (7.2). Figure 7.3(b) thus provides a direct visualization of the spatial coherence of the source.

Figure 7.4 shows the OAM spectrum obtained by numerically Fourier trans-

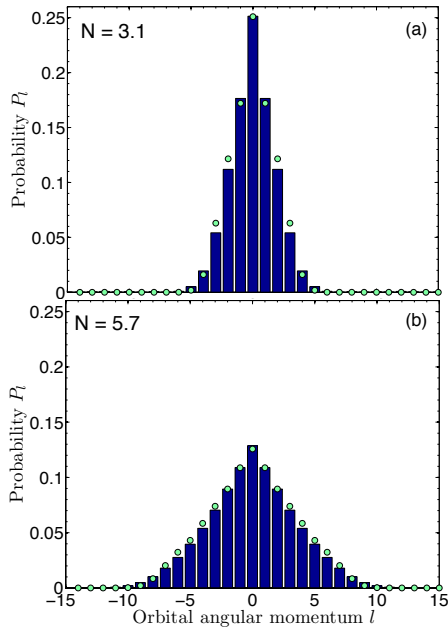


Figure 7.4: OAM spectrum obtained for two different circular apertures (a)  $d_1 = 1.2$  mm ( $N = 3.1$ ) and (b)  $d_1 = 2.2$  mm ( $N = 5.7$ ). The bars represent the experimental results and the circles the theoretical predictions, according to Eqs. (7.3) and (7.4).

forming the visibilities in Fig. 7.2. The bars represent the experimental results and the circles the theoretical predictions according to Eqs. (7.3) and (7.4). The weights  $P_l$  represent, as before, the probability of having a mode in an OAM eigenstate with azimuthal number  $l$ . Notice the very good agreement between theory and experiment. We can see that the  $P_l$  distributions have an approximately triangular shape and a well defined cutoff, associated with the sharp edges of the two apertures. This cutoff is higher for a system with a larger aperture; for an aperture with diameter  $d_1 = 1.2$  mm, we have  $|l_{max}| = 5$  while for  $d_1 = 2.2$  mm, the number of modes is limited by  $|l_{max}| = 10$ .

It is a well known result in classical optics that the number of available spatial channels in a certain optical system can be (approximately) quantified by the “degrees of freedom” or Shannon number  $S$  of this system [137], which is proportional to  $A\Omega/\lambda^2$ . Here  $A$  is the area of the first aperture and  $\Omega$  the solid angle subtended by the second aperture. More spatial modes are clearly allowed in a system with larger apertures. In our experiments, only the azimuthal modes, and not the radial ones, are being counted. This justifies the dependence of our results on the Fresnel-type number  $N = \sqrt{S}$ .

## 7.3 Conclusion

In conclusion, we presented the first experimental measurement of the OAM spectrum of a partially coherent light. Our source was designed to be approximately quasi homogeneous, without an overall OAM. The experimental technique can be extended to more general beams. If the symmetry  $P_l = P_{-l}$  is not obeyed, the phase of the interferometer should be stabilized and the intensity difference of the two output beams should be measured instead [136]. An additional measurement with a  $\pi/2$  phase shift will provide the amplitude of a *sine* series that should now be added to Eq. (7.5). Furthermore, this extended method also works for asymmetric beams or apertures [136]. Be aware, however, that due to the *quasi-intrinsic* nature of the OAM, the spectrum  $P_l$  will depend on the choice of the rotation axis.



# 8

## Spatial coherence of partially coherent classical beams with and without orbital angular momentum

We study the spatial coherence of a partially coherent beam before and after being transmitted through a spiral phase plate that changes the overall orbital angular momentum of the field. The two-point coherence function is measured and directly visualized on a CCD through interference in a Mach-Zehnder interferometer equipped with an image rotator. We show, in particular, how the coherence singularities associated with Airy rings are strongly affected by the spiral phase plate.

H. Di Lorenzo Pires, J. Woudenberg, and M. P. van Exter, *Measurements of spatial coherence of partially coherent light with and without orbital angular momentum*, J. Opt. Soc. Am. A **27**, 2630 (2010).

## 8.1 Introduction

Coherent singular optics is a prominent field of optical sciences [138]. Since the pioneering paper of Nye and Berry [139], great effort has been devoted to understand the fundamental properties of the “dislocations in wave trains” and to develop its technological applications. Wave dislocations or phase singularities are singular points of a complex-valued function, like in the complex representation of the electric field, where the amplitude is zero and the phase not well defined. A prominent example of such singularities are the so-called optical vortices. They are present in coherent beams, like the Laguerre-Gauss modes, and are associated with a screw-like circulation of the phase around the center of the beam, where the intensity is zero [140]. Another example of phase singularities are the dark rings of an Airy pattern, which appears in the focal plane of a uniformly illuminated lens [141] or in the diffraction pattern of a spatially coherent wave behind a circular aperture [142, 143].

Recently, the field of singular optics was extended to the realm of partially coherent light and the concept of “phase singularities of correlation functions” was introduced [127, 128, 144, 145]. A partially coherent field can be mathematically described by its cross-spectral density function (or coherence function)  $W(\mathbf{r}_1, \mathbf{r}_2)$ , which determines how the fluctuations of the field at a certain point  $\mathbf{r}_1$  are correlated with the fluctuations at  $\mathbf{r}_2$ . When a partially coherent beam is transmitted through an aperture or a spiral phase plate, sets of points can be found where the coherence is zero valued, implying the existence of phase singularities of this function. These points usually form a line in the transition between positively and negatively correlated field. The correlation singularity is considered a ‘virtual’ feature of the field, as it cannot be associated with any zeros of intensities but only with zeros of the two-point second-order coherence function [146].

This new branch of singular optics has been extensively studied, both theoretically [146–152] and experimentally [153–157]. Observations of a “coherence vortex” for an incoherent field have been reported [156] and the robustness of these singularities has been demonstrated [154]. The importance of correlation singularities to imaging science, where partially coherent illumination is often employed, has also been considered [150]. For a comprehensive discussion on the subject, see Ref. [158].

In this Chapter we will present measurements of the cross-spectral density  $W(\mathbf{r}_1, \mathbf{r}_2)$  for partially coherent light that exhibits two types of coherence singularities. The first singularities are the Airy rings that appear in the coherence function upon propagation behind a circular aperture with incoherent illumination. The second type of singularities are created by the transmission through a spiral phase plate with topological charge  $\ell = 1$ . The field now acquires an overall orbital angular momentum  $\ell\hbar$  per photon and an additional ring dislocation becomes visible in the coherence. We will show how these two types of singularities interact when the transverse coherence length of the source is changed.

In theoretical analyses of spatial correlation vortices in partially coherent

beams, the coherence of the initial field is often approximated by a Gaussian-Schell correlator [2], such that the input contains no coherence singularities. Although this approach allows analytical solutions, it can be an oversimplification of the experimental geometry. This remark also applies to [154], in which the existence of a ring dislocation in the correlation function was experimentally verified for the first time. In this Chapter we will develop a different theoretical approach that allows us to compute the propagation of a more general class of partially coherent fields, before and after being transmitted through a vortex phase plate.

Experimentally, we measure the cross-spectral density function of the field through interference in a Mach-Zehnder interferometer equipped with an image rotator. Furthermore, we implement a powerful method that allows the coherence singularities to be visualized in one single picture.

The Chapter is organized as follows: In Section 8.2 we formally introduce the cross-spectral density and calculate this function for our particular source. In Section 8.3 a convenient mathematical description of the propagation of partially coherent fields is developed and results of numerical simulations are presented. In section 8.4 we describe the experimental setup and present the results of our measurements. A summary of the results and conclusions are presented in Section 8.5.

## 8.2 Cross-spectral density

The state of coherence of light can be described by the cross-spectral density or mutual coherence function  $W(\boldsymbol{\rho}_1, \boldsymbol{\rho}_2, z; \omega) = \langle E^*(\boldsymbol{\rho}_1, z; \omega)E(\boldsymbol{\rho}_2, z; \omega) \rangle$ , where the brackets  $\langle \dots \rangle$  denotes average over an ensemble of strictly monochromatic waves. We are considering here the correlations between the transverse positions  $\boldsymbol{\rho}_1$  and  $\boldsymbol{\rho}_2$  at a fixed plane  $z$ . The cross spectral density can be measured by superposing the field with a phase delayed and spatially shifted copy of itself, yielding a combined intensity pattern profile

$$I = I_1 + I_2 + 2\text{Re} [W(\boldsymbol{\rho}_1, \boldsymbol{\rho}_2, z; \omega)e^{i\delta}], \quad (8.1)$$

where  $I_1$  and  $I_2$  are the intensities at positions  $\boldsymbol{\rho}_1$  and  $\boldsymbol{\rho}_2$ . By varying the phase  $\delta$  and subtracting the single intensities, both the real and imaginary components of  $W$  can be obtained (see Sec. 4.7.2 of [2] for a more rigorous derivation). For simplicity, we will omit the frequency  $\omega$  dependence in the derivation below of the cross-spectral density function for our particular source.

Figure 8.1 shows the geometry considered for the calculations. A circular aperture of diameter  $d_1$  is uniformly illuminated by fully incoherent light. A second aperture of diameter  $d_2$  is placed at a distance  $L$  from the first aperture, in a plane defined as  $z = 0$ . The field correlations between points  $\boldsymbol{\rho}_1$  and  $\boldsymbol{\rho}_2$  at  $z = 0$  can be computed with the van Cittert-Zernike theorem [2], which states that the mutual coherence  $W(\boldsymbol{\rho}_1, \boldsymbol{\rho}_2)$  in the far field of a spatially incoherent planar source is the Fourier transform of the intensity across the source. The cross-spectral density of the beam at  $z = 0$ , just behind aperture 2 is thus given

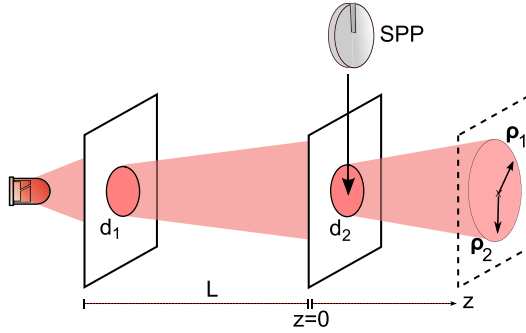


Figure 8.1: Geometry considered for the calculations. A circular aperture of diameter  $d_1$  is illuminated by fully incoherent light. A second aperture of diameter  $d_2$  is placed at a distance  $L$  from  $d_1$ , at  $z = 0$ . A spiral phase plate (SPP) can be placed just after aperture 2. The field correlations between the transverse positions  $\rho_1$  and  $\rho_2$  at the plane  $z$  are studied.

by

$$W_0(\rho_1, \rho_2) = T(\rho_1)T(\rho_2) \frac{J_1(\alpha|\rho_1 - \rho_2|)}{\alpha|\rho_1 - \rho_2|} e^{\frac{i\pi}{\lambda L}(\rho_1^2 - \rho_2^2)}, \quad (8.2)$$

where  $J_1(\cdot)$  is the first order Bessel function of the first kind,  $\alpha = \pi d_1 / \lambda L$ , and  $\lambda$  is the optical wavelength. The function  $T(\rho)$  describes the intensity profile at  $z = 0$ . It describes both the transmission profile of the second aperture and the illuminating intensity profile at  $z = 0$ , which itself is determined by the coherence of the light in the source  $d_1$ . The intensity at  $z = 0$  is uniform only in the limit of fully incoherent illumination [133].

The mutual coherence  $W_0$  generally decreases at increased distance between the two points  $\rho_1$  and  $\rho_2$ , up to a separation where the light is completely uncorrelated. This separation is defined as the coherence length  $L_c$  of the beam. Inspired by the theory of diffraction, the zeros of the function  $J_1(x)/x$  are denoted as the coherence Airy rings. For the first Airy ring we have

$$L_c = 1.22 \frac{\lambda L}{d_1}. \quad (8.3)$$

For a separation somewhat larger than  $L_c$  the coherence reappears. The fluctuations of the field are now slightly anti-correlated, associated with a  $\pi$  phase shift in the complex coherence function.

In order to investigate the properties of a coherence vortex, we add a spiral phase plate (SPP) centered inside aperture 2. This plate introduces a phase  $e^{i\ell\phi}$  to the optical field, i.e., a phase factor that varies linearly with the azimuthal angle  $\phi$ , and is able to change the overall angular momentum of the beam by  $\ell\hbar$  per photon. If the incident field would be a coherent Gaussian beam, the output beam would acquire a dip in the intensity that goes to zero and has an increasing

width under propagation [159]. The effect of this same SSP on a *partially coherent* beam is to change the cross-spectral density according to

$$W(\boldsymbol{\rho}_1, \boldsymbol{\rho}_2) = W_0(\boldsymbol{\rho}_1, \boldsymbol{\rho}_2)e^{i\ell(\phi_1 - \phi_2)}, \quad (8.4)$$

where  $W_0$  and  $W$  are the cross-spectral density just before and just after the SPP, respectively, and  $\phi_i$  is the azimuthal angle corresponding to the transverse position vector  $\boldsymbol{\rho}_i$ , for  $i = 1, 2$ . Under partially coherent illumination, the intensity after the SSP doesn't go to zero anymore. The coherence function will, however, still exhibit a zero, i.e., a coherence vortex in the form of a ring dislocation whose radius increases as the beam propagates [154]. Part of this Chapter addresses the question: "What is combined effect of this vortex ring with the Airy rings already present in the incident beam?"

### 8.3 Propagation of a partially coherent beam

The theory of propagation of partially coherent beams is well known [2,4]. Since the mutual coherence function satisfies two independent wave equations for the two position coordinates, both coordinates can be independently propagated using the same propagation laws of fields. In the Fresnel regime, the propagation of the cross-spectral density  $W(\boldsymbol{\rho}_1, \boldsymbol{\rho}_2; 0)$  from the plane  $z = 0$  to a certain plane  $z > 0$  can thus be written as

$$W(\boldsymbol{\rho}_1, \boldsymbol{\rho}_2; z) = \iint_{-\infty}^{+\infty} W(\boldsymbol{\rho}'_1, \boldsymbol{\rho}'_2; 0) e^{i\frac{k}{2z}|\boldsymbol{\rho}_1 - \boldsymbol{\rho}'_1|^2} e^{-i\frac{k}{2z}|\boldsymbol{\rho}_2 - \boldsymbol{\rho}'_2|^2} d\boldsymbol{\rho}'_1 d\boldsymbol{\rho}'_2, \quad (8.5)$$

where  $k = 2\pi/\lambda$ . Proportionality factors will be omitted in all equations throughout the Chapter. Equation (8.5) is a four-dimensional (4D) integral that cannot be easily solved, neither analytically nor numerically, except in a few special cases. Different approaches have been proposed in order to numerically treat this problem, such as the coherent-mode decomposition [2], Fourier-transform method [160], Monte Carlo simulation [161], and use of elementary functions [162]. One strategy is trying to rewrite Eq. (8.5) as a two-dimensional (2D) integral, which can then be numerically evaluated. With our particular problem in mind, we will follow this route.

First, notice that just after the  $\ell = 1$  SPP the coherence function, given by combining Eqs. (8.2) and (8.4), assumes the form

$$W(\boldsymbol{\rho}_1, \boldsymbol{\rho}_2; 0) = A(\boldsymbol{\rho}_1)A^*(\boldsymbol{\rho}_2)f(\boldsymbol{\rho}_1 - \boldsymbol{\rho}_2), \quad (8.6)$$

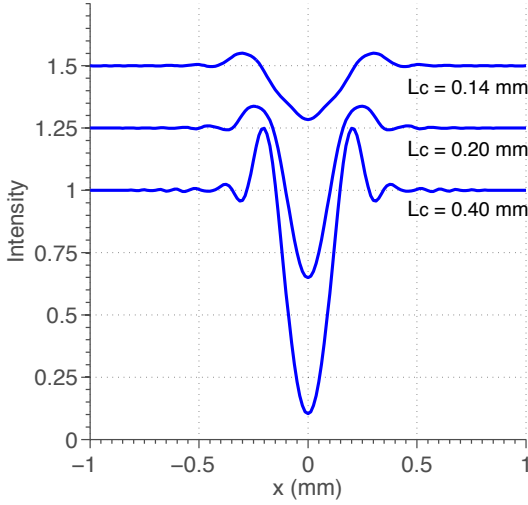


Figure 8.2: Cross sections of the theoretical (normalized) intensity distributions in the plane  $z = 45$  mm for different values of the coherence length  $L_c$  at the SPP and open second aperture. The curves are vertically displaced by 0.25 from each other.

with

$$A(\rho) = T(\rho)e^{\frac{i\pi}{\lambda L}\rho^2}e^{i\phi}, \quad (8.7)$$

$$f(\rho) = \frac{J_1(\alpha\rho)}{\alpha\rho}. \quad (8.8)$$

Equation (8.6) is very general and applies to all quasihomogeneous light sources [133]. The propagation of this coherence function to a plane  $z > 0$  is given by substituting Eq. (8.6) in Eq. (8.5). By introducing “sum” and “difference” coordinates

$$\rho_+ = \frac{\rho'_1 + \rho'_2}{2}, \quad \Delta\rho = \rho'_1 - \rho'_2, \quad (8.9)$$

$$\sigma = \frac{\rho_1 + \rho_2}{2}, \quad \delta = \rho_1 - \rho_2. \quad (8.10)$$

we can simplify the propagation integral to

$$W(\rho_1, \rho_2; z) = \int f(\Delta\rho) e^{-i\frac{k}{z}\Delta\rho\sigma} \times \left[ \int g\left(\rho_+ + \frac{\Delta\rho}{2}\right) g^*\left(\rho_+ - \frac{\Delta\rho}{2}\right) e^{-i\frac{k}{z}\rho_+\delta} d\rho_+ \right] d\Delta\rho, \quad (8.11)$$

where we defined the function

$$g(\boldsymbol{\rho}) \equiv A(\boldsymbol{\rho})e^{i\frac{k}{2z}\boldsymbol{\rho}^2}. \quad (8.12)$$

Next, we write the functions  $g$  and  $g^*$  in the second integral (between brackets) in terms of its Fourier transform,  $G(\mathbf{u}) = \mathcal{F}[g]$ . After some straightforward manipulations and simplifications one recognizes the Fourier transform  $F(\mathbf{u}) = \mathcal{F}[f]$  of the function  $f(\Delta\boldsymbol{\rho})$ . The propagated cross-spectral density can finally be represented by the following 2D integral, instead of 4D

$$\begin{aligned} \mathcal{W}(\boldsymbol{\sigma}, \boldsymbol{\delta}; z) = & \quad (8.13) \\ & \int G\left(\mathbf{u} - \frac{k}{2z}\boldsymbol{\delta}\right) F\left(\mathbf{u} + \frac{k}{z}\boldsymbol{\sigma}\right) G^*\left(\mathbf{u} + \frac{k}{2z}\boldsymbol{\delta}\right) d\mathbf{u}. \end{aligned}$$

Equation (8.13) is represented in the sum and difference coordinates according to  $\mathcal{W}(\boldsymbol{\sigma}, \boldsymbol{\delta}; z) = W(\boldsymbol{\rho}_1, \boldsymbol{\rho}_2; z)$ . It allows us to compute the mutual coherence function by solving one single 2D integral for each  $(\boldsymbol{\sigma}, \boldsymbol{\delta})$  combination. In practice, we are mainly interested in two important cases: the intensity distribution in the plane  $z$ ,  $I(\boldsymbol{\rho}; z) = W(\boldsymbol{\rho}, \boldsymbol{\rho}; z)$  which corresponds to  $\boldsymbol{\sigma} = \boldsymbol{\rho}$  and  $\boldsymbol{\delta} = 0$ , and the ‘‘coherence’’ of the field  $X(\boldsymbol{\rho}; z) = W(\boldsymbol{\rho}, -\boldsymbol{\rho}; z)$ , which corresponds to  $\boldsymbol{\sigma} = 0$  and  $\boldsymbol{\delta} = 2\boldsymbol{\rho}$ . From Eq. (8.13) they can be calculated via

$$I(\boldsymbol{\rho}; z) = \int |G(\mathbf{u})|^2 F\left(\mathbf{u} + \frac{k}{z}\boldsymbol{\rho}\right) d\mathbf{u}, \quad (8.14)$$

$$X(\boldsymbol{\rho}; z) = \int G\left(\mathbf{u} - \frac{k}{z}\boldsymbol{\rho}\right) F(\mathbf{u}) G^*\left(\mathbf{u} + \frac{k}{z}\boldsymbol{\rho}\right) d\mathbf{u}. \quad (8.15)$$

Equation (8.13) is especially useful if one has analytical expressions for the functions  $F(\mathbf{u})$  and  $G(\mathbf{u})$ . A straightforward numerical integration is then able to provide the desired results. Even when such analytical expressions can’t be found, Eq. (8.13) is still very convenient, since (2D) FFT algorithms for numerical Fourier transform are very efficient.

Analytical solutions can be found for our particular problem.  $F(\mathbf{u})$  is the Fourier transform of the coherence term  $f(\boldsymbol{\rho})$  at the plane  $z = 0$ , i.e.,

$$\begin{aligned} F(\mathbf{u}) = \mathcal{F}[f] &= \int \frac{J_1(\alpha|\boldsymbol{\rho}|)}{\alpha|\boldsymbol{\rho}|} e^{i\boldsymbol{\rho}\cdot\mathbf{u}} d\boldsymbol{\rho} \\ &= \begin{cases} 1, & u \leq \frac{kd_1}{2L} \\ 0, & u > \frac{kd_1}{2L} \end{cases} \quad (8.16) \end{aligned}$$

Apart from being simple, this function conveniently limits the numerical integration to a finite range.  $G(\mathbf{u})$  is the Fourier transform of the function  $g(\boldsymbol{\rho})$  defined

by Eq. (8.12), which reads

$$g(\boldsymbol{\rho}) = T(\rho) e^{\frac{ik}{2}(\frac{1}{z} + \frac{1}{L})\rho^2} e^{i\phi}, \quad (8.17)$$

where  $T(\rho)$  is the intensity distribution after the second aperture. In connection with our experiments, we will assume that  $d_2$  is very large and that the intensity is approximately uniform at  $z = 0$ . We have then

$$G(\mathbf{u}) = \mathcal{F}[g] = \int_0^\infty \int_0^{2\pi} \rho \, d\rho \, d\phi \, e^{ia\rho^2} e^{i(\phi + \boldsymbol{\rho} \cdot \mathbf{u})}, \quad (8.18)$$

where  $a = \frac{k}{2}(\frac{1}{z} + \frac{1}{L})$ . This integral can be analytically solved and results in

$$G(\mathbf{u}) = e^{i\phi} u e^{-\frac{iu^2}{8a}} \left[ J_1\left(\frac{u^2}{8a}\right) + iJ_0\left(\frac{u^2}{8a}\right) \right], \quad (8.19)$$

where  $\phi$  is the azimuthal angle of  $\mathbf{u}$  and  $J_0$  and  $J_1$  are the zeroth- and first-order Bessel functions. If the illumination is nonuniform but Gaussian  $T(\rho) = e^{-\rho^2/w^2}$ , due to partial coherence at the first aperture, the solution of Eq. (8.18) retains its form, but with the substitution  $ia \rightarrow ia - 1/w^2$ .

Next, we will present results for numerical calculations performed for a range of parameters similar to those used in our experiments. We consider the propagation of the coherence function to the plane  $z = 45$  mm from the SPP for different values of the coherence length  $L_c$  of the beam.

Figure 8.2 shows cross sections of the calculated intensity profiles when the coherence length of the source is varied. The predictions agree with those in [147], namely, that the core of the beam behind the SPP fills with diffuse light when the coherence at the SPP is decreased. The dip in the intensity drops to zero in the limit of completely coherent illumination. The intensity for points far away from the center remains uniform and is not affected by the SPP. With partially coherent illumination, the signature of a coherence singularity is only revealed in the *coherence* of the beam.

Figure 8.3 shows cross sections of the calculated coherence  $X(\boldsymbol{\rho})$  in the presence and absence of the SPP. The calculations are made using Eq. (8.15) for various values of the input coherence length  $L_c$ . The results are normalized to modulus one. For completeness, we note that a different kind of normalization is more often employed, namely,  $\mu(\mathbf{r}_1, \mathbf{r}_2) = W(\mathbf{r}_1, \mathbf{r}_2) / \sqrt{I(\mathbf{r}_1)I(\mathbf{r}_2)}$ . The so-called *spectral degree of coherence*  $\mu$  reaches its upper bound  $|\mu| = 1$  when pairs of points are completely correlated. Experimentally, however, it is more convenient to study the cross-spectral density  $W$ , instead of  $\mu$ , and normalize it to some reference value.

The dashed lines show the coherence  $X(\boldsymbol{\rho})$  for propagation without a phase plate. In this case we observe the coherence Airy rings, described by  $J_1(x)/x$ . The coherence length  $L_c$  at the plane  $z = 45$  mm is slightly larger than the  $L_c$

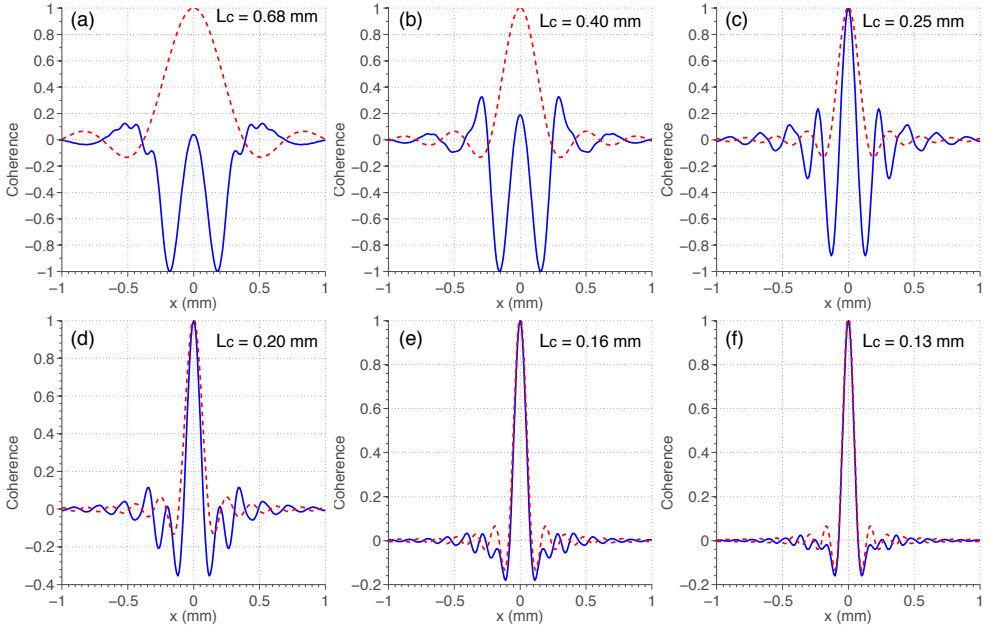


Figure 8.3: Cross sections of the theoretical coherence  $X(\rho)$  of the beam in the plane  $z = 45$  mm after the (open) second aperture. The dashed line is the prediction without phase plate; the continuous line corresponds to a SPP placed at aperture 2. The calculations are made for different values of the coherence length, (a)  $L_c = 0.68$  mm, (b)  $L_c = 0.40$  mm, (c)  $L_c = 0.25$  mm, (d)  $L_c = 0.20$  mm, (e)  $L_c = 0.16$  mm, and (f)  $L_c = 0.13$  mm.

at  $z = 0$  mm. This occurs because light “gains” coherence under the additional propagation. The coherence length at the plane  $z$  can be approximated by  $L_c^z \approx L_c(1 + z/L)$ .

The addition of a SPP at  $z = 0$  mm considerably modifies the coherence  $X(\rho)$ , now depicted as continuous lines. When the coherence length of the beam is relatively high, as in Figs. 8.3 (a) and (b), a coherence singularity manifest itself as a ring dislocation in  $X(\rho)$ , whose radius increases with decreasing coherence. This would be the only effect observable if the cross-spectral density before the SPP were described by a Gaussian function [147]. This trend changes when the input beam already has phase dislocations, associated with Airy rings. We now find that the vortex ring due to the SPP does not cross the first Airy ring when  $L_c$  is reduced, as has been hypothesized in Ref. [154], but modifies the coherence function as a whole. In fact, the presence of the SPP can even reduce the number of phase dislocations within a certain radius. For example, in Fig. 8.3(e) the coherence function without SPP crosses the zero six times for  $|x| < 0.5$  mm, but only five times when the SPP is in place.

Another interesting feature concerns the relative phase of the Airy rings in

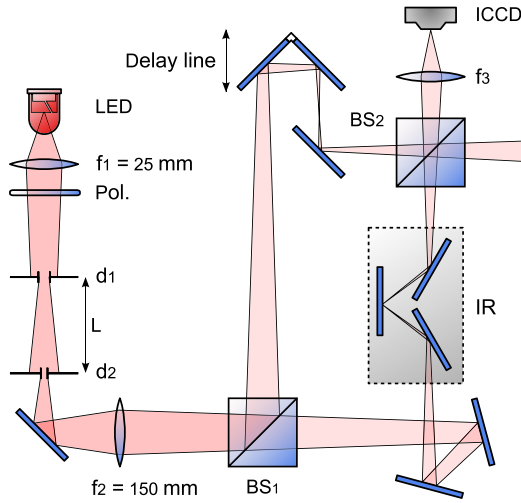


Figure 8.4: Experimental setup used to generate a partially coherent beam and to measure its mutual coherence function (see text for details).

the cases with and without SPP. For radii larger than some  $x_d$ , the phase of the Airy rings with the SPP inserted is observed to shift by  $\pi$  with respect to the case where the SPP is absent. The smaller the coherence length  $L_c$ , the larger  $x_d$ . For our geometry, the effect of the SPP on the coherence function is thus to shift the phase of the Airy rings by  $\pi$  when  $|x| \rightarrow \infty$ .

## 8.4 Measurements of the spatial coherence

The experimental determination of the mutual coherence function is a very important task in optics. Different techniques have been proposed and implemented, such as Young interferometers [163, 164] and different types of image inversion interferometers [165], like Sagnac [166–168] and Mach-Zehnder [169]. Most approaches, however, don't allow a direct visualization of the coherence function and positions and angles must be scanned to allow full reconstruction. In the following experiments, we will take advantage of our rotationally symmetric geometry and introduce a powerful method to visualize and measure the coherence function.

Figure 8.4 shows the experimental setup used to generate a partially coherent beam and to measure its mutual coherence function. A  $15\times$  magnified image of a light emitting diode (LED), with central wavelength  $\lambda = 826 \text{ nm}$ , is centered on an adjustable circular aperture of diameter  $d_1$ , after being filtered by a polarizer. We can regard this aperture as an incoherent, circular source of uniform intensity. The light propagates a distance  $L$  to a second circular aperture of fixed diameter  $d_2$ , which is approximately uniformly illuminated. The coherence length  $L_c$  of the

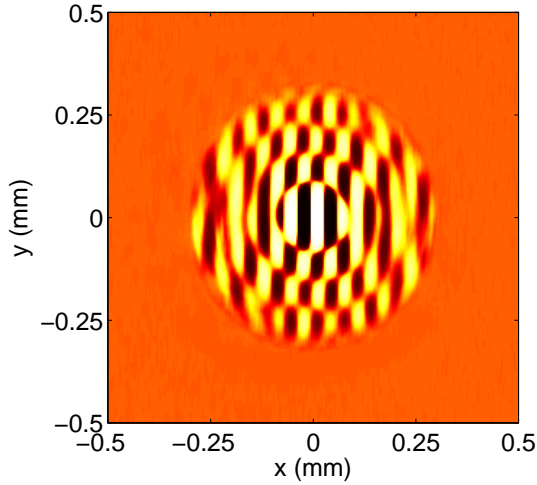


Figure 8.5: Visualization of coherence singularities in  $X(\rho)$  as measured from interference fringes. The SPP is absent and the aperture 2 is imaged at the ICCD. We set  $L_c = 0.15$  mm and  $d_2 = 0.59$  mm. The arctangent of  $X$  is shown in order to enhance contrast.

light at aperture 2 can be controlled by modifying the diameter  $d_1$  and the distance  $L$ , according to Eq. (8.3). Our results will be labeled by this coherence length, which we scan from  $L_c = 0.13 - 0.68$  mm, by adjusting the first aperture in the range  $d_1 = 0.6 - 3.0$  mm at  $L = 200$  mm or  $L = 400$  mm. A spiral phase plate (SPP) with  $\ell = 1$  can be placed just after the second aperture, at an actual distance of 10 mm. We will present results with and without the SPP. Lenses are used to image the coherence function either at the plane of the second aperture, or, after some propagation, at  $z = 45$  mm after the SPP. In the first case,  $f_2 = 150$  mm and  $f_3 = 250$  mm lenses are used to make a  $4\times$  magnified image of  $d_2$  at an intensified CCD (ICCD) camera. In the second case,  $f_2 = 150$  mm and  $f_3 = 40$  mm lenses are used to make a  $17.7\times$  magnified image of the plane  $z = 45$  mm at the ICCD.

In order to measure the mutual coherence function, the generated beam is sent through a Mach-Zehnder interferometer, where it is initially split at beam splitter BS1 and then recombined at BS2. In one of the arms of this interferometer there is an image rotator (IR), which rotates the input image by  $\theta$  degrees around its axis. A delay line allows us to set both arms of the interferometer to the same length. The original beam is then recombined with a rotated version of itself, and the interference pattern is recorded with the ICCD. Following Eq. (8.1), the cross spectral density  $W(\rho_1, \rho_2; z)$  can be obtained by measuring the interference pattern and subtracting the single intensities, which are obtained by blocking either arm of the interferometer.

The setup is ideal to extract the intensity  $I(\rho)$  and the coherence  $X(\rho)$  and to directly visualize the coherence singularities. The measured patterns will be rotationally symmetric when all components are properly aligned. A rotational

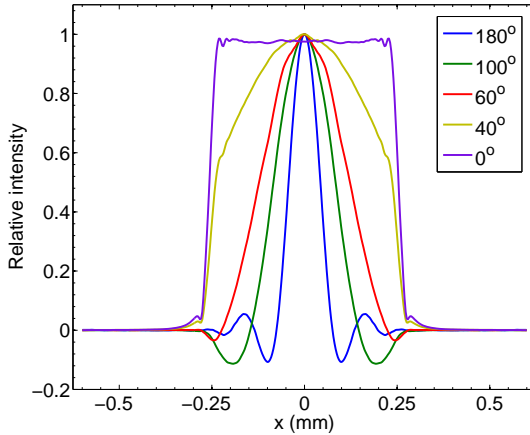


Figure 8.6: Cross sections of the interference pattern for different values of the angle of rotation  $\theta$ . The coherence length of the source is  $L_c = 0.15$  mm, the diameter of the second aperture is  $d_2 = 0.59$  mm, and the imaged plane is  $z = 0$  mm. The SPP is not in the setup.

average of the cross sections will fully characterize  $I(\rho)$  or  $X(\rho)$ . Alternatively, a more straightforward visualization of the singularities can be obtained by misaligning beam splitter  $BS_2$ , so that interference fringes are observed. Let us first illustrate this fringes method.

Figure 8.5 shows how the singularities in the coherence  $X(\rho)$  can be visualized by means of interference fringes. The SPP is absent and we choose  $L_c = 0.15$  mm and  $d_2 = 0.59$  mm. The plane of the aperture 2 is imaged at the ICCD. The image rotation is maximum, at  $\theta = 180^\circ$ . To enhance contrast, the *arctangent* of the results is shown, while some noise is removed with a Savitzky-Golay smoothing filter [170]. For  $\theta = 180^\circ$ , we are basically interfering the points  $\rho$  and  $-\rho$ , to reveal the coherence of the field. The singularities related to the Airy rings are clearly visible as flips from dark to bright within a fringe line. When the separation between these points equals the coherence length  $L_c$ , the function is zero valued. For larger separations, the field fluctuations can be either correlated or anti-correlated. A  $\pi$  phase shift indicates a coherence singularity and the transition between correlation and anti-correlation.

Figure 8.6 shows rotationally averaged cross sections of the measured interference pattern for different rotation angles  $\theta$ . These measurements are performed with the interferometer completely aligned. According to Eq. (8.2), we expect the interference to scale as

$$W_0(\rho, \theta) = |T(\rho)|^2 \frac{J_1[\alpha(\theta)\rho]}{\alpha(\theta)\rho}, \quad (8.20)$$

where  $\alpha(\theta) = 2\pi d_1 \sin(\theta/2)/\lambda L$ . At  $\theta = 0^\circ$ , we observe only the intensity distribution, which is the top-hat transmission profile of aperture 2. At  $\theta = 180^\circ$ ,

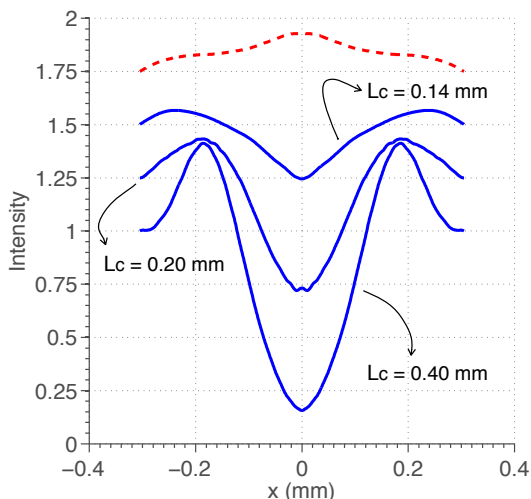


Figure 8.7: Rotationally averaged cross sections of the intensity profiles in the plane  $z = 45$  mm after the SPP. The dashed curve shows the intensity profile in the absence of the SPP. All curves are normalized and are displaced by 0.25 from each other.

we observe the coherence of the field. Most noticeable, a rotation from  $180^\circ$  to  $0^\circ$  allows one to “zoom in” the (central structure) of the coherence, of which the horizontal axis scale as  $1/\alpha(\theta)$ . Notice how the coherence is stretched as  $\theta$  decreases.

Figures 8.7-8.9 present results of measurements performed when a  $\ell = 1$  SPP is placed just after the second aperture. As discussed in Section 8.2, prominent effects are expected to be observed only after propagation. In the following experiments, the second aperture is wide open at  $d_2 = 2$  mm and the plane  $z = 45$  mm is imaged on the ICCD. A magnification of  $17.7\times$  is used in order to highlight the effects close to the beam center.

Figure 8.7 shows measurements of the intensity  $I(\rho)$  for different values of the coherence length  $L_c$  at the SPP. The curves are rotationally averaged cross sections of the intensity profiles measured by the ICCD. The observed intensity dips are similar to those reported in [147] and in agreement with our calculations and Fig. 8.2. The dips are more prominent when the coherence length is large; the dark core is filled with diffuse light at reduced  $L_c$ . Furthermore, the maximum in the intensity is closer to the center at large coherence ( $L_c = 0.40$ ) than at small coherence ( $L_c = 0.14$ ). The dashed curve shows the intensity profile without SPP; it varies just slightly in the considered range.

Figure 8.8 shows the coherence  $X(\rho)$  measured in the plane  $z = 45$  mm for different coherence lengths  $L_c$  of the illumination. The rotationally averaged cross-sections are displayed on the left (dashed curve without the SPP, solid curve with SPP). The interference fringes made with beamsplitter  $BS_2$  misaligned are

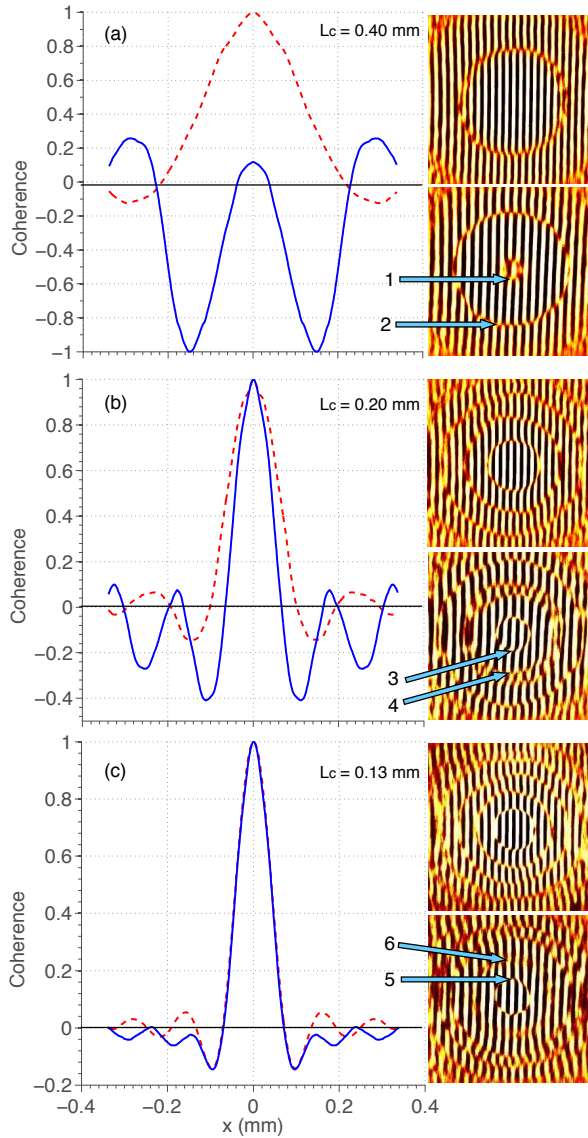


Figure 8.8: Measured coherence  $X(\rho)$  for (a)  $L_c = 0.40$  mm, (b)  $L_c = 0.20$  mm, and (c)  $L_c = 0.13$  mm. Left column: rotationally averaged cross sections. Continuous curves are measured with the SPP; dashed curves are without SPP. Right column: Interference patterns measured with beam splitter  $BS_2$  misaligned. Upper figures correspond to the case without SPP and lower figures to the case with SPP.

shown on the right (top pictures without SPP, bottom pictures with SPP). All the results are normalized to modulus one.

Figure 8.8(a) shows that when the coherence length is relatively large ( $L_c = 0.40$  mm), the effect of the SPP is to create an additional small ring dislocation in the coherence  $X(\rho)$ , indicated by arrow 1. The second dislocation, associated with the Airy ring, is pushed slightly outwards (arrow 2). Two phase jumps are clearly observable by following a fringe that goes through the center of the pattern. Notice also that the phase of the Airy rings are  $\pi$ -shifted with respect to the case without SPP. Figure 8.8(b) shows that as the coherence of the source decreases, the radius of the vortex ring increases (arrow 3), up to a point where it approaches the shrinking Airy rings (arrow 4).

Figure 8.8(c) shows the measured coherence  $X(\rho)$  at  $L_c = 0.13$  mm. At this point, the first singularity with the SPP already coincides with the first Airy ring in the coherence without SPP (arrow 5). The effect of the SPP is now far from trivial, but one can clearly see that it does reduce the total number of phase jumps, with respect to the case where the SPP is present. This is nicely illustrated in the fringes patterns. Notice that, contrary to Figs. 8.8(a) and 8.8(b), in Fig. 8.8(c) the fringes for the measurement with the SPP flip one time less than for the measurements without the SPP. There are no phase jumps at the position shown by arrow 6. It is also clear in the cross section that the coherence  $X(\rho)$  approaches the zero axis, but doesn't cross it. In the comparison of  $X(\rho)$  with and without SPP in Fig. 8.8(c), we distinguish three regimes. For  $\rho \lesssim 0.14$  mm the coherence for the case with SPP coincides with the one for the case without SPP. For  $\rho \gtrsim 0.25$  mm these two functions approximately coincide, but are  $\pi$ -shifted from each other; and for  $0.14$  mm  $\lesssim \rho \lesssim 0.25$  mm, there is a transition region. All measurements are in good agreement with the theoretical predictions shown in Fig. 8.3.

Finally, we have tracked how the first ring dislocation depends on the coherence length  $L_c$  of the beam. Figure 8.9 shows the diameter  $D$  of the first zero of the coherence  $X(\rho)$  as function of  $L_c$ . Two regimes can be distinguished. When  $L_c$  is relatively large,  $D$  increases with decreasing  $L_c$ . When the mutual coherence before the SPP is described by a Gauss-Schell model, one expects [154]

$$D = \sqrt{\frac{2}{\pi}} \frac{z\lambda}{L_c}. \quad (8.21)$$

In our experiments, we expect then a dependence  $D = 0.030/L_c$ . A curve fitting using only the last eight points of the plot provide  $D = (0.027 \pm 0.001)/L_c$  mm, which is in reasonably good agreement. The other regime occurs for smaller values of  $L_c$ . In this regime the first zero of  $X(\rho)$  coincides with the Airy ring. Since the first zero of the Airy ring is our definition of coherence length, we now expect  $D = L_c$ . This line is also shown in the plot.

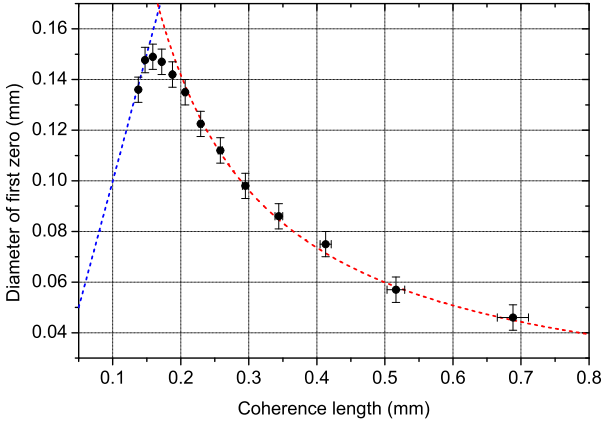


Figure 8.9: Dependence of the diameter of the first dislocation ring on the coherence length  $L_c$  of the input beam. The left line is defined as  $D = L_c$ . The right curve is a curve fit of the last eight points and has the form  $D = (0.027 \pm 0.001)/L_c$ .

## 8.5 Conclusion

In this Chapter we implement a method to directly visualize the coherence function of beams with two types of coherence singularities, Airy rings and a coherence vortex created by a spiral phase plate (SPP). As long as the radius of this vortex ring is small compared to the first Airy ring, the general features can be explained by the model presented in [147], which assumes a Gaussian shape for the coherence. In this regime, the origin of the coherence singularity can be well understood from a geometrical optics point of view, as discussed in [152]. For smaller values of the coherence length  $L_c$ , the presence of the SPP modifies the coherence function in a more subtle way. A clear-cut physical picture of the interaction between the Airy rings and the coherence vortex is not available. We formulate a theoretical description of the problem and present numerical simulations. Experimental and theoretical results are in good agreement. Curiously and non intuitively, the phase plate can reduce the total number of phase singularities in the field, instead of increasing it. Furthermore, the SPP shifts the phase of the Airy rings by  $\pi$ , for larger radii. These results provide new insights into the spatial coherence of beams with non-zero overall orbital angular momentum and into the properties of spatial correlation vortices.

# 9

## Statistical properties of nonlocal speckles

We experimentally study the statistics of non-local speckle patterns, obtained when spatially entangled photon pairs are scattered through a random medium. Striking differences arise between the scattering of highly entangled states and almost separable states. Both the purity of the field and the Schmidt number, which quantifies the number of entangled modes, can be obtained from the visibility of the speckles. We observe non-exponential statistics for both the intensities and the two-photon correlations.

## 9.1 Introduction

Speckles are the random intensity patterns that appear when a wave is reflected from or transmitted through a random scattering medium [171,172]. At the time of its discovery, speckles were mainly seen as a drawback in coherent imaging systems. Further studies revealed, however, that the speckle pattern carries information both on the coherence properties of the radiation and on the microscopic details of the scattering object. After averaging over many realizations of the disorder, useful information can be retrieved through statistical arguments. The study of wave propagation in random media has revealed many interesting phenomena, such as conductance fluctuations [173,174], enhanced backscattering [175], and Anderson localization [176].

More recently, considerable effort has been devoted to understand how the quantum nature of light manifests after multiple scattering [177–188]. A broad range of subjects have been investigated, such as the degradation of polarization entanglement [178,179,182], the transport of quantum noise [177,180], and the dynamics of photons in disordered lattices [188]. It has also been shown that entanglement can be induced by multiple scattering of squeezed states and that quantum interference can survive ensemble average [185,186].

The special features of scattering of quantum light are best appreciated in the spatial domain. When a pure two-photon state is scattered by a random medium, it will produce so-called “two-photon speckles” [187]. These patterns are remarkable because they exist in the more abstract space of fourth-order correlations. They show up in the coincidence count rate of two (scanning) detectors and are a function of two position coordinates.

In this Chapter we present the first experimental investigation of the statistics of two-photon speckles. We show that either non-local or separable speckle patterns can be observed, depending on the degree of spatial entanglement of the initial state. By averaging over many realizations of the disorder, important properties of the source can be retrieved. In this way, the two-photon state can be proven to be pure and the Schmidt number  $K$ , which quantifies the number of entangled modes, can be obtained. Experimentally quantifying multi-dimensional entanglement is an important, but very demanding task [39]. Our approach provides a feasible and theoretically sound solution for this problem. Finally, we recover the probability distributions of single-photon intensities and two-photon coincidences, which, contrary to most classical speckles, are in general non exponential.

## 9.2 Theory

Statistical distributions of two-photon speckles were first theoretically discussed by Beenakker *et al.* [184]. In this Chapter we will greatly benefit from their results. But in order to extend their conclusions to more realistic experimental conditions, our analysis will deviate at several points. First of all, we do not use a random matrix description, with its discrete number of input and output

channels, but instead we use a continuous description. The only requirement we will impose on the scattering is that it is sufficiently random and unitary (i.e. energy conserving). Second, we will start from the most general pure input state, whose Schmidt coefficients are not necessarily equal, i.e., we show how the *Schmidt number*  $K$  can be measured, instead of the *Schmidt rank*. Finally, we do not separate the two-photon phase space into half-spaces,  $q > 0$  and  $q < 0$ . This allows us to investigate separable states ( $K = 1$ ) as well.

We begin by reviewing some properties of classical speckles. When a field  $f(\mathbf{x})$  is scattered by a random medium, all possible light paths will acquire arbitrary phases. When these components are added together, they will form a complex interference pattern known as speckle. For unitary scattering, we can describe this pattern by the transformation  $F(\mathbf{x}) = \mathcal{U}[f(\mathbf{x})]$ . If the number of scattering centers is very large, the Central Limit Theorem assures that the probability density function for both the real and imaginary components of  $F(\mathbf{x})$  is asymptotically Gaussian. The intensity  $I = |F|^2$  has then an exponential distribution  $P(I) \propto \exp(-I/\langle I \rangle)$ , with average  $\langle I \rangle$ . The visibility or contrast of any speckle pattern is defined by  $\mathcal{V} = \langle I^2 \rangle / \langle I \rangle^2 - 1$ , where the brackets denote ensemble average. The exponential distribution has unity visibility.

These results can be generalized to a *two-photon field*  $A(\mathbf{x}_1, \mathbf{x}_2)$ , which describes the probability amplitude of finding one photon at transverse position  $\mathbf{x}_1$  and the other at  $\mathbf{x}_2$ . The quantum-entangled nature of the state is best appreciated in the so-called Schmidt decomposition [13], where the two-photon state is expressed as a discrete sum over factorizable two-photon states of the form  $A_k(\mathbf{x}_1, \mathbf{x}_2) = f_k(\mathbf{x}_1)g_k(\mathbf{x}_2)$ . Part of the beauty of the Schmidt decomposition is that it remains intact upon unitary scattering, as orthogonal states remain orthogonal under this scattering; only the eigenstates are modified. If we write the input state in the Schmidt form, the output state will be

$$A_{out}(\mathbf{x}_1, \mathbf{x}_2) = \sum_k \sqrt{\lambda_k} F_k(\mathbf{x}_1) G_k(\mathbf{x}_2), \quad (9.1)$$

where  $\lambda_k$  are the Schmidt coefficients and, analogously to the classical case,  $F_k(\mathbf{x}) = \mathcal{U}[f_k(\mathbf{x})]$  and  $G_k(\mathbf{x}) = \mathcal{U}[g_k(\mathbf{x})]$  are the speckle fields corresponding to the transformation of the Schmidt modes  $f_k$  and  $g_k$ . The coincidence rate measured by two photon counters at positions  $\mathbf{x}_1$  and  $\mathbf{x}_2$  is  $R_{cc}(\mathbf{x}_1, \mathbf{x}_2) \propto |A_{out}(\mathbf{x}_1, \mathbf{x}_2)|^2$ . If the initial state is separable, i.e., just one term in the Schmidt decomposition, the two-photon speckles observed in  $R_{cc}$  will also be separable. On the other hand, if the input state is highly entangled,  $R_{cc}$  will reveal a *nonlocal* speckle pattern. The effective number of entangled modes in the decomposition (9.1) is usually quantified by the Schmidt number  $K = 1/\sum_k |\lambda_k|^2$ . The Schmidt coefficients are normalized such that  $\sum_k |\lambda_k| = 1$ .

We will now study the statistics of the intensities  $I$  (single photon rate) and

of the coincidences  $R_{cc}$ . From Eq. (9.1) we immediately obtain

$$R_{cc} = \alpha \sum_{j,k} \sqrt{\lambda_j^* \lambda_k} F_j^* F_k G_j^* G_k, \quad (9.2)$$

$$R_{cc}^2 = \alpha^2 \sum_{i,j,k,m} \sqrt{\lambda_i^* \lambda_j^* \lambda_k \lambda_m} F_i^* F_j^* F_k F_m G_i^* G_j^* G_k G_m, \quad (9.3)$$

where we omit the coordinates  $\mathbf{x}_1$  and  $\mathbf{x}_2$ . The proportionality constant  $\alpha$  incorporates the experimental factors that relate the theory to the measured coincidences rate. Let's first assume that  $\mathbf{x}_1 \neq \mathbf{x}_2$ . In this case, the speckle fields  $F$  and  $G$  are statistically independent. Furthermore, the fields  $F_i$  and  $F_j$  are also statistically independent, unless  $i = j$ . The same holds for  $G$ . Due to the Gaussian-random nature of the scattered fields,  $\langle |F_i|^{2n} \rangle = \langle I^n \rangle = n!$ , where  $I$  is the exponentially distributed intensity, but  $\langle F_i^{2n} \rangle = 0$ . With these ingredients, it is straightforward to show that

$$\text{For } \mathbf{x}_1 \neq \mathbf{x}_2 \quad \begin{cases} \langle R_{cc} \rangle = \alpha, \\ \mathcal{V}_c = 1 + \frac{2}{K}, \end{cases} \quad (9.4)$$

where  $K$  is the Schmidt number and  $\mathcal{V}_c$  is the visibility of the two-photon speckle pattern. We see that  $\mathcal{V}_c$  varies from 3 (separable state) to 1 (maximally entangled state).

The single photon intensities can be obtained by a partial trace of the two-photon state as

$$I_{out}(\mathbf{x}) = \sum_k |\lambda_k| |F_k(\mathbf{x})|^2 = \sum_k |\lambda_k| |G_k(\mathbf{x})|^2, \quad (9.5)$$

which is an incoherent sum of many speckle patterns. The more terms in the distribution, the more uniform the intensity becomes. The visibility of the one-photon speckle reduces with the number of modes as

$$\mathcal{V}_I = \frac{1}{K}. \quad (9.6)$$

When the number of terms in (9.5) is very large, the Central Limit Theorem can be used to show that  $P(I)$  is normally distributed with mean  $\langle I \rangle$  and standard deviation  $1/\sqrt{K}$ .

We have assumed so far that the input state is pure. In a more general sense, the purity  $\mathcal{P}$  of the two-photon state can be calculated from the visibilities  $\mathcal{V}_I$  and  $\mathcal{V}_c$  of the single-photon and two-photon speckles as

$$\mathcal{P} = \mathcal{V}_c - 2\mathcal{V}_I. \quad (9.7)$$

This crucial result, which was first derived in [184], can also be proven using our formalism.

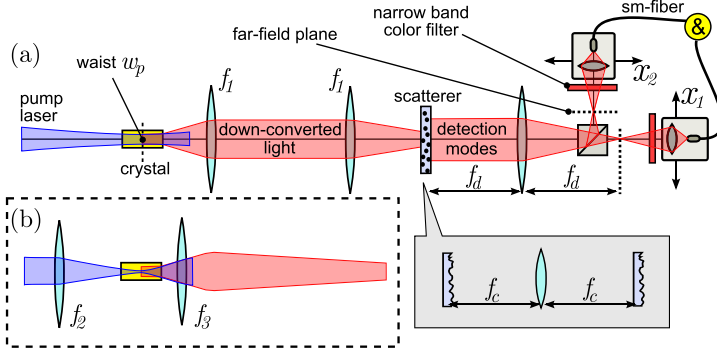


Figure 9.1: Entangled photon pairs are obtained via type I SPDC by pumping a 5-mm thick periodically poled KTP crystal with a laser beam ( $\lambda_p = 413.1$  nm and 200 mW power). The crystal center is imaged onto the incident plane of the scatterer with two  $f_1 = 200$  mm lenses. The far field of the scattering medium is imaged with a  $f_d = 250$  mm lens onto the detection plane. Detection occurs via projection onto two single-mode fibers. The size of the detection modes ( $w_{det} = 140$   $\mu\text{m}$ ) determines the spatial resolution in the far-field plane. Narrow band spectral filters (5 nm at 826.2 nm) are used to selected down-converted light close to frequency degeneracy. The inset shows our scattering medium, which comprises two light shaping diffusers positioned in each other's far field (using a lens  $f_c = 10$  mm). This configuration mimics a volume scatter [187], but it also allows sufficient counts to be measured. (a) Generation of a state with  $K_{th} = 80$ . The pump is weakly focused to a waist  $w_p = 160$   $\mu\text{m}$ . (b) Generation of a state with  $K_{th} = 1.4$ . The pump lens (not shown) is removed and a  $f_2 = 100$  mm lens focuses the beam to a spot  $w_p = 11.5$   $\mu\text{m}$  at the center of the crystal. The two  $f_1$  lenses are removed and a single  $f_3 = 59$  mm lens images the center of the crystal on the scatterer.

The probability distributions for  $R_{cc}$  and  $I$  can be deduced from Eqs. (9.2) and (9.5), which are weighted sums of products of random Gaussian variables. For the special case of  $K$  equally weighted Schmidt modes, with  $\lambda_k = 1/K$ , we recover the closed expressions of Ref. [184]

$$P_1(\tilde{I}) = \tilde{I}^{K-1} \frac{e^{-K\tilde{I}} K^K}{\Gamma(K)}, \quad (9.8)$$

$$P_2(\tilde{R}_{cc}) = \frac{K}{\Gamma(K)} (K\tilde{R}_{cc})^{\frac{K-1}{2}} \mathcal{K}_{K-1} \left[ 2\sqrt{K\tilde{R}_{cc}} \right], \quad (9.9)$$

where  $\tilde{I} = I/\langle I \rangle$  and  $\tilde{R}_{cc} = R_{cc}/\langle R_{cc} \rangle$ ,  $\Gamma$  is the Gamma function and  $\mathcal{K}_{K-1}$  is a modified Bessel function of the second kind. The single-photon probability density  $P_1(\tilde{I})$  is a Gamma distribution while, the two-photon probability  $P_2(\tilde{R}_{cc})$  is known as the “K”-distribution [189].

We finally consider the case  $\mathbf{x}_1 = \mathbf{x}_2 = \mathbf{x}$ . Because of the symmetry  $A(\mathbf{x}_1, \mathbf{x}_2) = A(\mathbf{x}_2, \mathbf{x}_1)$  of the two-photon field, the Schmidt modes  $F_i(\mathbf{x})$  and

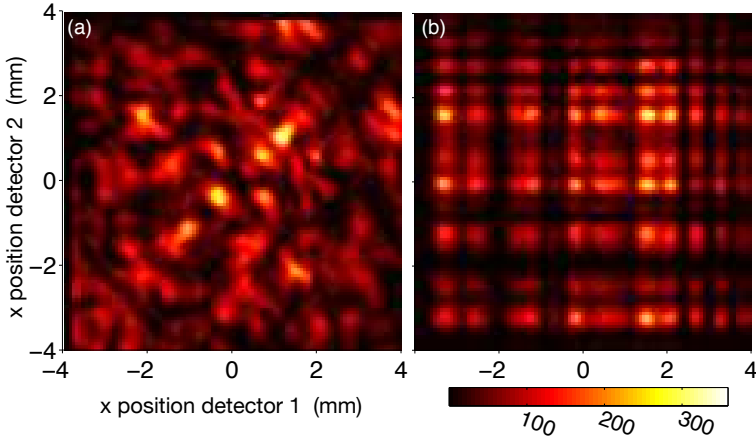


Figure 9.2: Coincidence counts measured by two scanning detectors for a single realization of the scattering medium. (a) A non-local speckle pattern, corresponding to the scattering of a highly entangled state with  $K_{th} = 80$ . (b) Separable speckle pattern, corresponding to the scattering of a state with a small number of modes,  $K_{th} = 1.4$ .

$G_j(\mathbf{x})$  are not all statistically independent. Taking this into consideration, we can repeat the steps above and show that Eqs. (9.4) and (9.9) retain their form, but with the substitution  $K \rightarrow K/2$ , which implies that  $\mathcal{V}_c = 1 + \frac{4}{K}$ . The average  $\langle R_{cc} \rangle = 2\alpha$  is twice as large. This photon bunching effect survives averaging over many realizations of the disorder.

### 9.3 Experimental results

Figure 9.1 shows the experimental setup used to generate entangled photon pairs and to measure the statistics of the speckles. We investigate two different regimes, namely, a highly entangled state with theoretical Schmidt number  $K_{th} = 80$  and an almost separable state with  $K_{th} = 1.4$ .

Figure 9.2 shows measurements of two-photon speckle patterns for a fixed realization of the scattering medium. These figures are obtained by scanning both detectors horizontally, keeping  $y_1 = y_2$  fixed, and recording the coincidences count rate. The results are corrected for accidental counts. Figure 9.2(a) corresponds to a highly entangled state, while Fig. 9.2(b) shows the results for an almost separable state. The differences are striking. When operating under reduced number of modes, the coincidences rate is practically separable in the product of single-photon intensities,  $R_{cc}(x_1, x_2) \approx I(x_1)I(x_2)$ . On the other hand, when the number of modes is very large the pattern is clearly non-separable. By measuring photon 1 at a certain position, photon 2 is “nonlocally” projected into a speckle pattern that depends on the position of detector 1. Notice also that

Table 9.1: Overview of the measured statistics, obtained for  $x_1 \neq x_2$ . The theoretical Schmidt number  $K_{th}$  is calculated via the procedure in [13];  $\mathcal{V}_I$  and  $\mathcal{V}_c$  are the visibilities of the intensities and coincidences respectively,  $\mathcal{P}$  is the purity, and  $K_{ex}$  is the measured Schmidt number.

$K_{th}$	$\mathcal{V}_I$	$\mathcal{V}_c$	$\mathcal{P}$	$K_{ex}$
1.4	$0.83 \pm 0.02$	$2.65 \pm 0.15$	$0.98 \pm 0.15$	$1.20 \pm 0.03$
80	$0.014 \pm 0.002$	$1.04 \pm 0.04$	$1.01 \pm 0.04$	$70 \pm 9$

both patterns are symmetric with respect to the  $x_1 = x_2$  diagonal; this reflects the symmetry of the field  $A(\mathbf{x}_1, \mathbf{x}_2) = A(\mathbf{x}_2, \mathbf{x}_1)$ .

We will next discuss the statistical distributions of the coincidences  $R_{cc}$  and intensities  $I$  under various conditions. To this end, the detectors are placed at fixed positions, either  $x_1 = x_2$  or  $x_1 \neq x_2$ . Different realizations of disorder are obtained by rotating the first or the second diffuser in steps of  $3^\circ$ . In this way, we can measure 14,400 realizations of the scattering medium. The acquisition time for each measurement was 5 seconds. An overview of the results for  $x_1 \neq x_2$  is shown in table 9.1.

Figure 9.3 shows the probability distributions measured for  $K_{th} = 1.4$ , i.e., for an almost separable state. The dashed red curves are the theoretical curves, obtained using Eqs. (9.8) and (9.9) with the measured Schmidt number  $K$  instead. The dashed black lines correspond to an exponential distribution and confirm that all three distributions are non-exponential. When  $K_{th} = 1.4$ , the field is not only coherent in fourth order, but it is also almost coherent in second order. The single photon speckles exhibit high visibility,  $\mathcal{V}_I = 0.83 \pm 0.02$ , not very far from unity visibility, which holds for completely coherent light. This visibility allows us to estimate the experimental Schmidt number to be  $K = 1.20 \pm 0.03$ , confirming that our state is practically separable. The associated probability distribution  $P_1$  is shown in Fig. 9.3(a). The distribution is slightly concave on a semi-log scale and is theoretically described by a Gamma distribution. This distribution would have been exactly exponential in the limit  $K = 1$ .

The results for the coincidence counts are more interesting. Figure 9.3(b) shows the probability distribution  $P_2$  of two-photon speckles for  $x_1 \neq x_2$ . The associated visibility  $\mathcal{V}_c = 2.65 \pm 0.15$  has a relatively large error margin. The main reason for this error is the occurrence of a few very large fluctuations, associated with the extreme tail of the  $P_2$  distribution. As we can see, the distribution has a convex shape on a semi-log scale, such that the probability of very small and very high fluctuations are higher than for an exponential distribution. The error in  $\mathcal{V}_c$  will propagate to the purity  $\mathcal{P}$ . We obtain an average value  $\mathcal{P} = 0.98 \pm 0.15$  for the purity of the two-photon state.

Figure 9.3(c) shows the probability distribution of  $R_{cc}$  for  $x_1 = x_2$ . The convexity is even more pronounced and the peak close to  $R_{cc} \approx 0$  is twice as large,

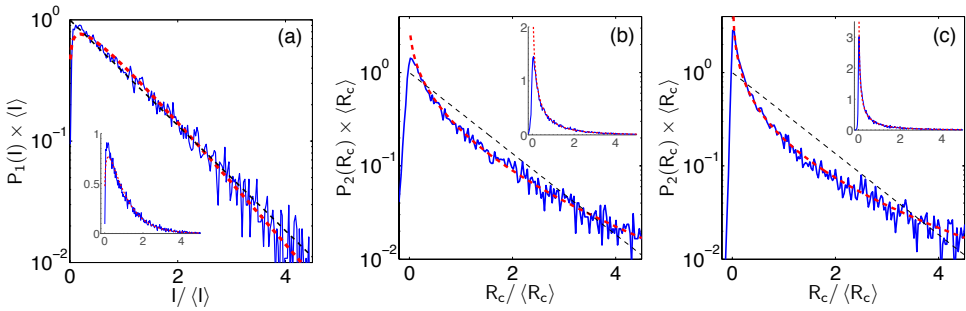


Figure 9.3: Probability distributions measured for  $K_{th} = 1.4$ . The (red) dashed curves are the theoretical distributions and the (black) dashed lines correspond to an exponential distribution. The insets show the results on a linear scale. (a) Distribution  $P_1$  of intensities. (b) Distribution  $P_2$  of coincidences for  $x_1 \neq x_2$ . (c) Distribution  $P_2$  of coincidences for  $x_1 = x_2$ .

as can be seen in the insets. Theoretically, the peak at  $R_{cc} = 0$  should be much higher. The measured shape and peak around  $R_{cc} = 0$ , however, are limited by the experimental noise that inevitably dominates at the smallest count rates. The two-photon speckle contrast is  $\mathcal{V}_c = 4.45 \pm 0.30$ , which reflects the almost classical, i.e. local, nature of the fluctuations. For a fully factorizable speckle, the visibility of  $R_{cc} \approx I^2$  is  $\mathcal{V}_c = 5$ .

Figure 9.4 shows the probability distributions for a highly entangled state with  $K_{th} = 80$ . In the limit of high  $K$ , the two-photon speckles are a genuine two-coordinate function and can be considered as a more authentic generalization of classical speckles to fourth-order optics. The fluctuations at  $x_1 = x_2$  are now not more special than those at  $x_1 \neq x_2$ ; only the average level will be different due to the photon bunching effect. The probability distribution  $P_2$  for  $x_1 \neq x_2$ , shown in Fig. 9.4(a), is practically exponential and the visibility  $\mathcal{V}_c = 1.04 \pm 0.04$  is close to unity. Extreme fluctuations do not occur very often for this distribution. As a result, the error in  $\mathcal{V}_c$  is smaller. The distributions for  $x_1 = x_2$  and  $x_1 \neq x_2$  have approximately the same shape, but since the number of modes is still finite, the visibility for  $x_1 = x_2$  is slightly higher, namely,  $\mathcal{V}_c = 1.10 \pm 0.05$ .

Figure 9.4(b) shows the probability distribution  $P_1$  on a linear scale. Because the reduced one-photon state is now practically incoherent, the intensity will exhibit only limited fluctuations around the average  $\langle I \rangle$ . As expected from the Central Limit Theorem, the curve is approximately Gaussian. The associated one-photon visibility is only  $\mathcal{V}_I = 0.014 \pm 0.002$ . To measure this value, we had to correct for a small wedge effect in the diffusors. This correction introduces a relative larger error, which propagates when calculating the Schmidt number. Nonetheless, the obtained value  $K_{ex} = 70 \pm 9$  agrees reasonably well with the large number of modes expected. Finally, we obtain  $\mathcal{P} = 1.01 \pm 0.04$  for the purity of the state.

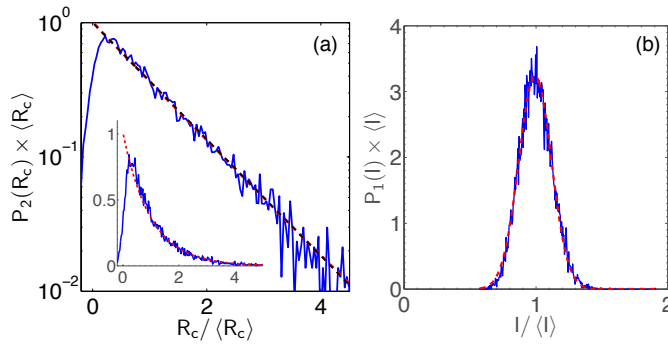


Figure 9.4: Probability distributions measured for  $K_{th} = 80$ . The (red) curves are the theoretical distributions and the (black) dashed lines correspond to an exponential distribution. (a) Distribution  $P_2$  of coincidences for  $x_1 \neq x_2$ . (b) Distribution  $P_1$  of intensities.

## 9.4 Conclusion

We have studied the statistics of two-photon speckle patterns. These patterns are a generalization of classical speckles to fourth-order optics. Depending on the degree of spatial entanglement of the input state, the scattered field can exhibit very different structures and statistics. We have measured the Schmidt number of both an almost separable state and a highly entangled state. We have also proven that both generated states are pure to a good degree of accuracy. These results provide new insights into the role of spatial entanglement to the scattering of light and opens the door to new developments in the field of quantum optics in random media.



# Bibliography

- [1] R. Feynman, R. Leighton, and M. Sands, *The Feynman Lectures in Physics* (Addison-Wesley, Reading, 1963).
- [2] L. Mandel and E. Wolf, *Optical Coherence and Quantum Optics* (Cambridge University Press, 1995).
- [3] E. Wolf, *Introduction to the Theory of Coherence and Polarization of Light* (Cambridge University Press, New York, 2007).
- [4] M. Born and E. Wolf, *Principles of Optics* 7th ed. (Cambridge U. Press, 1999).
- [5] R. H. Brown and R. Twiss, "Correlation between photons in two coherent beams of light," *Nature* **177**, 27 (1956).
- [6] R. Hanbury Brown and R. Q. Twiss, "A test of a new type of stellar interferometer on Sirius," *Nature* **178**, 1046 (1956).
- [7] G. A. Rebka and R. V. Pound, "Time-correlated photons," *Nature* **180**, 1035 (1957).
- [8] R. J. Glauber, "The quantum theory of optical coherence," *Phys. Rev.* **130**, 2529 (1963).
- [9] B. R. Mollow, "Photon correlations in the parametric frequency splitting of light," *Phys. Rev. A* **8**, 2684 (1973).
- [10] D. N. Klyshko, "Utilization of vacuum fluctuations as an optical brightness standard," *Sov. J. Quantum Electron.* **7**, 591 (1977).
- [11] M. H. Rubin, D. N. Klyshko, Y. H. Shih, and A. V. Sergienko, "Theory of two-photon entanglement in type-II optical parametric down-conversion," *Phys. Rev. A* **50**, 5122 (1994).
- [12] A. Peres, *Quantum Theory: Concepts and Methods* (Kluwer Academic, Boston, 1995)
- [13] C. K. Law and J. H. Eberly, "Analysis and interpretation of high transverse entanglement in optical parametric down conversion," *Phys. Rev. Lett.* **92**, 127903 (2004).

- [14] T. B. Pittman, D. V. Strekalov, D. N. Klyshko, M. H. Rubin, A. V. Sergienko, and Y. H. Shih, "Two-photon geometric optics," *Phys. Rev. A* **53**, 2804 (1996).
- [15] D. V. Strekalov, A. V. Sergienko, D. N. Klyshko, and Y. H. Shih, "Observation of two-photon ghost interference and diffraction," *Phys. Rev. Lett.* **74**, 3600 (1995).
- [16] A. N. Boto, P. Kok, D. S. Abrams, S. L. Braunstein, C. P. Williams, and J. P. Dowling, "Quantum interferometric optical lithography: exploiting entanglement to beat the diffraction limit," *Phys. Rev. Lett.* **85**, 2733 (2000).
- [17] M. D'Angelo, M. V. Chekhova, and Y. Shih, "Two-photon diffraction and quantum lithography," *Phys. Rev. Lett.* **87**, 013602 (2001).
- [18] T. Yarnall, A. F. Abouraddy, B. E. A. Saleh, and M. C. Teich, "Experimental violation of bell's inequality in spatial-parity space," *Phys. Rev. Lett.* **99**, 170408 (2007).
- [19] C. H. Monken, P. H. Souto Ribeiro, and S. Pádua, "Transfer of angular spectrum and image formation in spontaneous parametric down-conversion," *Phys. Rev. A* **57**, 3123 (1998).
- [20] D. A. Kleinman and R. C. Miller, "Dependence of second-harmonic generation on the position of the focus," *Phys. Rev.* **148**, 302 (1966).
- [21] G. D. Boyd and D. A. Kleinman, "Parametric interaction of focused gaussian light beams," *J. Appl. Phys.* **39**, 3597 (1968).
- [22] W. A. T. Nogueira, S. P. Walborn, S. Pádua, and C. H. Monken, "Experimental observation of spatial antibunching of photons," *Phys. Rev. Lett.* **86**, 4009 (2001).
- [23] D. P. Caetano and P. H. Souto Ribeiro, "Generation of spatial antibunching with free-propagating twin beams," *Phys. Rev. A* **68**, 043806 (2003).
- [24] M. D'Angelo, Y.H. Kim, S. P. Kulik, and Y. Shih, "Identifying entanglement using quantum ghost interference and imaging," *Phys. Rev. Lett.* **92**, 233601 (2004).
- [25] J. C. Howell, R. S. Bennink, S. J. Bentley, and R. W. Boyd, "Realization of the Einstein-Podolsky-Rosen paradox using momentum- and position-entangled photons from spontaneous parametric down conversion," *Phys. Rev. Lett.* **92**, 210403 (2004).
- [26] B. E. A. Saleh, A. F. Abouraddy, A. V. Sergienko, and M. C. Teich, "Duality between partial coherence and partial entanglement," *Phys. Rev. A* **62**, 043816 (2000).
- [27] W. H. Peeters and M. P. van Exter, "Optical characterization of periodically-poled  $\text{KTiOPO}_4$ ," *Opt. Express* **16**, 7344 (2008).

- [28] S. Mancini, V. Giovannetti, D. Vitali, and P. Tombesi, "Entangling macroscopic oscillators exploiting radiation pressure," *Phys. Rev. Lett.* **88**, 120401 (2002).
- [29] M. V. Fedorov, M. A. Efremov, P. A. Volkov, and J. H. Eberly, "Short-pulse or strong-field breakup processes: a route to study entangled wave packets," *J. Phys. B* **39**, S467 (2006).
- [30] K. W. Chan, J. P. Torres, and J. H. Eberly, "Transverse entanglement migration in Hilbert space," *Phys. Rev. A* **75**, 050101(R) (2007).
- [31] C. K. Hong and L. Mandel, "Theory of parametric frequency down conversion of light," *Phys. Rev. A* **31**, 2409 (1985).
- [32] Y. H. Shih and C. O. Alley, "New type of einstein-podolsky-rosen-bohm experiment using pairs of light quanta produced by optical parametric down conversion," *Phys. Rev. Lett.* **61**, 2921 (1988).
- [33] D. Bouwmeester, J.-W. Pan, K. Mattle, M. Eibl, H. Weinfurter, and A. Zeilinger, "Experimental quantum teleportation," *Nature* **390**, 575 (1997).
- [34] A. V. Sergienko, M. Atatüre, Z. Walton, G. Jaeger, B. E. A. Saleh, and M. C. Teich, "Quantum cryptography using femtosecond-pulsed parametric down-conversion," *Phys. Rev. A* **60**, R2622 (1999).
- [35] M. V. Fedorov, M. A. Efremov, P. A. Volkov, E. V. Moreva, S. S. Straupe, and S. P. Kulik, "Spontaneous parametric down-conversion: Anisotropic and anomalously strong narrowing of biphoton momentum correlation distributions," *Phys. Rev. A* **77**, 032336 (2008).
- [36] S. P. Walborn and C. H. Monken, "Transverse spatial entanglement in parametric down-conversion," *Phys. Rev. A* **76**, 062305 (2007).
- [37] A. V. Burlakov, M. V. Chekhova, D. N. Klyshko, S. P. Kulik, A. N. Penin, Y. H. Shih, and D. V. Strekalov, "Interference effects in spontaneous two-photon parametric scattering from two macroscopic regions," *Phys. Rev. A* **56**, 3214 (1997).
- [38] M. Tsang, "Relationship between resolution enhancement and multiphoton absorption rate in quantum lithography," *Phys. Rev. A* **75**, 043813 (2007).
- [39] H. Di Lorenzo Pires and M. P. van Exter, "Observation of near-field correlations in spontaneous parametric down-conversion," *Phys. Rev. A* **79**, 041801(R) (2009).
- [40] P. H. Souto Ribeiro, C. H. Monken, and G. A. Barbosa, "Measurement of coherence area in parametric downconversion luminescence," *Appl. Opt.* **33**, 352 (1994).

- [41] I. F. Santos, J. G. Aguirre-Gómez, and S. Pádua, "Comparing quantum imaging with classical second-order incoherent imaging," *Phys. Rev. A* **77**, 043832 (2008).
- [42] A. Valencia, G. Scarcelli, M. D'Angelo, and Y. Shih, "Two-photon imaging with thermal light," *Phys. Rev. Lett.* **94**, 063601 (2005).
- [43] H. M. Ozaktas and D. Mendlovic, "Fractional Fourier optics," *J. Opt. Soc. Am. A* **12**, 743 (1995).
- [44] P. Pellat-Finet, "Fresnel diffraction and the fractional-order Fourier transform," *Opt. Lett.* **19**, 1388 (1994).
- [45] P. Pellat-Finet and G. Bonnet, "Fractional order Fourier transform and Fourier optics," *Opt. Commun.* **111**, 141 (1994).
- [46] D. S. Tasca, S. P. Walborn, P. H. Souto Ribeiro, and F. Toscano, "Detection of transverse entanglement in phase space," *Phys. Rev. A* **78**, 010304(R) (2008).
- [47] A. F. Abouraddy, B. E. A. Saleh, A. V. Sergienko, and M. C. Teich, "Entangled-photon Fourier optics," *J. Opt. Soc. Am. B* **19**, 1174 (2002).
- [48] M. B. Nasr, A. F. Abouraddy, M. C. Booth, B. E. A. Saleh, A. V. Sergienko, M. C. Teich, M. Kempe, and R. Wolleschensky, "Biphoton focusing for two-photon excitation," *Phys. Rev. A* **65**, 023816 (2002).
- [49] M. D'Angelo, A. Valencia, M. H. Rubin, and Y. Shih, "Resolution of quantum and classical ghost imaging," *Phys. Rev. A* **72**, 013810 (2005).
- [50] O. Cosme, A. Delgado, G. Lima, C. H. Monken, and S. Pádua, "Controlling the transverse correlation in QPM parametric down-conversion," arXiv:0906.4734.
- [51] M. H. Rubin, "Transverse correlation in optical spontaneous parametric down-conversion," *Phys. Rev. A* **54**, 5349 (1996).
- [52] W. H. Peeters, J. J. Renema, and M. P. van Exter, "Engineering of two-photon spatial quantum correlations behind a double slit," *Phys. Rev. A* **79**, 043817 (2009).
- [53] B. E. A. Saleh, M. C. Teich, and A. V. Sergienko, "Wolf Equations for Two-Photon Light," *Phys. Rev. Lett.* **94**, 223601 (2005).
- [54] V. Prasad, D. Semwogerere, and E. R. Weeks, "Confocal microscopy of colloids," *J. Phys.: Cond. Matt.* **19**, 113102 (2007).
- [55] D. A. Kleinman and R. C. Miller, "Dependence of second-harmonic generation on the position of the focus," *Phys. Rev.* **148**, 302 (1966).
- [56] D. A. Kleinman, A. Ashkin, and G. D. Boyd, "Second-harmonic generation of light by focused laser beams," *Phys. Rev.* **145**, 338 (1966).

- [57] W. A. T. Nogueira, S. P. Walborn, S. Pádua, and C. H. Monken, "Experimental observation of spatial antibunching of photons," *Phys. Rev. Lett.* **86**, 4009 (2001).
- [58] D. P. Caetano and P. H. Souto Ribeiro, "Generation of spatial antibunching with free-propagating twin beams," *Phys. Rev. A* **68**, 043806 (2003).
- [59] A. Gatti, E. Brambilla, L. Caspani, O. Jedrkiewicz, and L. A. Lugiato, "X entanglement: the nonfactorable spatiotemporal structure of biphoton correlation," *Phys. Rev. Lett.* **102**, 223601 (2009).
- [60] R. M. Gomes, A. Salles, F. Toscano, P. H. Souto Ribeiro, and S. P. Walborn, "Observation of a Nonlocal Optical Vortex," *Phys. Rev. Lett.* **103**, 033602 (2009).
- [61] H. Di Lorenzo Pires, C. H. Monken, and M. P. van Exter, "Direct measurement of transverse-mode entanglement in two-photon states," *Phys. Rev. A* **80**, 022307 (2009).
- [62] Z.Y.J. Ou, *Multi-Photon Quantum Interference* (Springer, New York, 2007).
- [63] H. Di Lorenzo Pires and M. P. van Exter, "Direct measurement of transverse-mode entanglement in two-photon states," *Phys. Rev. A* **80**, 053820 (2009).
- [64] S. P. Walborn, C. H. Monken, S. Pádua, and P. H. Souto Ribeiro, "Spatial correlations in parametric down-conversion," *Phys. Rep.* **495**, 87 (2010).
- [65] R. Andrews, E. Pike, and S. Sarkar, "Optimal coupling of entangled photons into single-mode optical fibers," *Opt. Express* **12**, 3264-3269 (2004).
- [66] A. Dragan, "Efficient fiber coupling of down-conversion photon pairs," *Phys. Rev. A* **70**, 053814 (2004).
- [67] D. Ljunggren and M. Tengner, "Optimal focusing for maximal collection of entangled narrow-band photon pairs into single-mode fibers," *Phys. Rev. A* **72**, 062301 (2005).
- [68] P. S. K. Lee, M. P. van Exter, and J. P. Woerdman, "How focused pumping affects type-II spontaneous parametric down-conversion," *Phys. Rev. A* **72**, 033803 (2005).
- [69] G. Molina-Terriza, S. Minardi, Y. Deyanova, C. I. Osorio, M. Hendrych, and J. P. Torres, "Control of the shape of the spatial mode function of photons generated in noncollinear spontaneous parametric down-conversion," *Phys. Rev. A* **72**, 065802 (2005).
- [70] R. S. Bennink, Y. Liu, D. D. Earl, and W. P. Grice, "Spatial distinguishability of photons produced by spontaneous parametric down-conversion with a focused pump," *Phys. Rev. A* **74**, 023802 (2006).

- [71] A. Ling, A. Lamas-Linares, and C. Kurtsiefer, "Absolute emission rates of spontaneous parametric down-conversion into single transverse Gaussian modes," *Phys. Rev. A* **77**, 043834 (2008).
- [72] Ö. Süzer and T. Goodson, "Does pump beam intensity affect the efficiency of spontaneous parametric down conversion?," *Opt. Express* **16**, 20166 (2008).
- [73] Z. Zhao, K. A. Meyer, W. B. Whitten, R. W. Shaw, R. S. Bennink, and W. P. Grice, "Observation of spectral asymmetry in cw-pumped type-II spontaneous parametric down-conversion," *Phys. Rev. A* **77**, 063828 (2008).
- [74] P. Kolenderski, W. Wasilewski, and K. Banaszek, "Modeling and optimization of photon pair sources based on spontaneous parametric down-conversion," *Phys. Rev. A* **80**, 013811 (2009).
- [75] R. S. Bennink, "Optimal collinear Gaussian beams for spontaneous parametric down-conversion," *Phys. Rev. A* **81**, 053805 (2010).
- [76] L. E. Vicent, A. B. U'Ren, R. Rangarajan, C. I. Osorio, J. P. Torres, L. Zhang, I. A. Walmsley, "Design of bright, fiber-coupled and fully factorable photon pair sources," *New J. Phys.* **12**, 093027 (2010).
- [77] W. H. Louisell, A. Yariv, and A. E. Siegman, "Quantum fluctuations and noise in parametric processes. I," *Phys. Rev.* **124**, 1646 (1961).
- [78] A. Yariv, *Quantum Electronics* (Wiley, New York, 1989).
- [79] B. Schröder, "Optical parametric amplification from quantum noise," *Opt. Quantum Electron.* **15**, 57 (1983).
- [80] A. Gatti, H. Wiedemann, L. A. Lugiato, I. Marzoli, G. L. Oppo, and S. M. Barnett, "Langevin treatment of quantum fluctuations and optical patterns in optical parametric oscillators below threshold," *Phys. Rev. A* **56**, 877 (1997).
- [81] A. Picozzi and M. Haelterman, "Influence of walk-off, dispersion, and diffraction on the coherence of parametric fluorescence," *Phys. Rev. E* **63**, 056611 (2001).
- [82] P. Di Trapani, G. Valiulis, W. Chinaglia, and A. Andreoni, "Two-dimensional spatial solitary waves from traveling-wave parametric amplification of the quantum noise," *Phys. Rev. Lett.* **80**, 265 (1998).
- [83] A. Picozzi and M. Haelterman, "Hidden coherence along space-time trajectories in parametric wave mixing," *Phys. Rev. Lett.* **88**, 083901 (2002).
- [84] O. Jedrkiewicz, A. Picozzi, M. Clerici, D. Faccio, and P. Di Trapani, "Emergence of X-shaped spatiotemporal coherence in optical waves," *Phys. Rev. Lett.* **97**, 243903 (2006).

- 
- [85] O. Jedrkiewicz, M. Clerici, A. Picozzi, D. Faccio, and P. Di Trapani, "X-shaped space-time coherence in optical parametric generation," *Phys. Rev. A* **76**, 033823 (2007).
- [86] H. F. Schouten and T. D. Visser, "The role of correlation functions in the theory of optical wave fields," *Am. J. Phys.* **76**, 867 (2008).
- [87] M. W. Mitchell, "Parametric down-conversion from a wave-equation approach: Geometry and absolute brightness," *Phys. Rev. A* **79**, 043835 (2009).
- [88] G. Bimonte, "Commutation relations for the electromagnetic field in the presence of dielectrics and conductors," *J. Phys. A: Math. Theor.* **43**, 155402 (2010).
- [89] W. Eckhardt, "Macroscopic theory of electromagnetic fluctuations and stationary radiative heat transfer," *Phys. Rev. A* **29**, 1991 (1984).
- [90] N. Gonzalez, G. Molina-Terriza, and J. P. Torres, "Properties of the spatial Wigner function of entangled photon pairs," *Phys. Rev. A* **80**, 043804 (2009).
- [91] P. Horodecki, "Measuring Quantum Entanglement without Prior State Reconstruction," *Phys. Rev. Lett.* **90**, 167901 (2003).
- [92] S. P. Walborn, P. H. Souto Ribeiro, L. Davidovich, F. Mintert, and A. Buchleitner, "Experimental determination of entanglement with a single measurement," *Nature (London)* **440**, 1022 (2006).
- [93] C. Schmid, N. Kiesel, W. Wieczorek, H. Weinfurter, F. Mintert, and A. Buchleitner, "Experimental direct observation of mixed state entanglement," *Phys. Rev. Lett.* **101**, 260505 (2008).
- [94] F. Mintert and A. Buchleitner, "Observable entanglement measure for mixed quantum states," *Phys. Rev. Lett.* **98**, 140505 (2007).
- [95] J. Cai and W. Song, "Novel schemes for directly measuring entanglement of general states," *Phys. Rev. Lett.* **101**, 190503 (2008).
- [96] S. M. Lee, S. W. Ji, H. W. Lee, and M. Suhail Zubairy, "Proposal for direct measurement of concurrence via visibility in a cavity QED system," *Phys. Rev. A* **77**, 040301(R) (2008).
- [97] L. Aolita, A. Buchleitner, and F. Mintert, "Scalable method to estimate experimentally the entanglement of multipartite systems," *Phys. Rev. A* **78**, 022308 (2008).
- [98] H. Bechmann-Pasquinucci and W. Tittel, "Quantum cryptography using larger alphabets," *Phys. Rev. A* **61**, 062308 (2000).
- [99] P. Rungta, V. Buzek, C. M. Caves, M. Hillery, and G. J. Milburn, "Universal state inversion and concurrence in arbitrary dimensions," *Phys. Rev. A* **64**, 042315 (2001).

- [100] M. V. Fedorov, M. A. Efremov, P. A. Volkov, E. V. Moreva, S. S. Straupe, and S. P. Kulik, "Spontaneous parametric down-conversion: Anisotropical and anomalously strong narrowing of biphoton momentum correlation distributions," *Phys. Rev. A* **77**, 032336 (2008).
- [101] M. V. Fedorov, M. A. Efremov, A. E. Kazakov, K. W. Chan, C. K. Law, and J. H. Eberly, "Packet narrowing and quantum entanglement in photoionization and photodissociation," *Phys. Rev. A* **69**, 052117 (2004).
- [102] M. J. Bastiaans, "The Wigner distribution function of partially coherent light," *Opt. Acta* **28**, 1215 (1981).
- [103] J. B. Pors, S. S. R. Oemrawsingh, A. Aiello, M. P. van Exter, E. R. Eliel, G. W. t Hooft, and J. P. Woerdman, "Shannon dimensionality of quantum channels and its application to photon entanglement," *Phys. Rev. Lett.* **101**, 120502 (2008).
- [104] H. Bechmann-Pasquinucci and W. Tittel, "Quantum cryptography using larger alphabets," *Phys. Rev. A* **61**, 062308 (2000).
- [105] A. Mair, A. Vaziri, G. Weihs, and A. Zeilinger, "Entanglement of the orbital angular momentum states of photons," *Nature (London)* **412**, 313 (2001).
- [106] A. Vaziri, G. Weihs, and A. Zeilinger, "Experimental Two-Photon, Three-Dimensional Entanglement for Quantum Communication," *Phys. Rev. Lett.* **89**, 240401 (2002).
- [107] J. Leach, B. Jack, J. Romero, M. Ritsch-Marte, R. W. Boyd, A. K. Jha, S. M. Barnett, S. Franke-Arnold, and M. J. Padgett, "Violation of a Bell inequality in two-dimensional orbital angular momentum state-spaces," *Opt. Express* **17**, 8287 (2009).
- [108] A. Vaziri, J. W. Pan, T. Jennewein, G. Weihs, and A. Zeilinger, "Concentration of higher dimensional entanglement: qutrits of photon orbital angular momentum," *Phys. Rev. Lett.* **91**, 227902 (2003).
- [109] G. Molina-Terriza,, A. Vaziri, R. Ursin, and A. Zeilinger, "Experimental quantum coin tossing," *Phys. Rev. Lett.* **94**, 040501 (2005).
- [110] J. P. Torres, A. Alexandrescu, and L. Torner, "Quantum spiral bandwidth of entangled two-photon states," *Phys. Rev. A* **68**, 050301(R) (2003).
- [111] L. Torner, J. P. Torres, and S. Carrasco, "Digital spiral imaging," *Opt. Express* **13**, 873 (2005).
- [112] W. H. Peeters, E. J. K. Verstegen, and M. P. van Exter, "Orbital angular momentum analysis of high-dimensional entanglement," *Phys. Rev. A* **76**, 042302 (2007).

- [113] A. K. Jha, B. Jack, E. Yao, J. Leach, R. W. Boyd, G. S. Buller, S. M. Barnett, S. Franke-Arnold, and M. J. Padgett, "Fourier relationship between the angle and angular momentum of entangled photons," *Phys. Rev. A* **78**, 043810 (2008).
- [114] G. Molina-Terriza, J. P. Torres, and L. Torner, "Twisted photons," *Nature Phys.* **3**, 305 (2007).
- [115] C. I. Osorio, G. Molina-Terriza, and J. P. Torres, "Correlations in orbital angular momentum of spatially entangled paired photons generated in parametric down-conversion," *Phys. Rev. A* **77**, 015810 (2008).
- [116] J. Leach, J. Courtial, K. Skeldon, S. M. Barnett, S. F. Arnold, and M. J. Padgett, "Interferometric methods to measure orbital and spin, or the total angular momentum of a single photon," *Phys. Rev. Lett.* **92**, 013601 (2004).
- [117] R. Zambrini and S. M. Barnett, "Quasi-intrinsic angular momentum and the measurement of its spectrum," *Phys. Rev. Lett.* **96**, 113901 (2006).
- [118] G. A. Barbosa, "Indistinguishability of orbital angular-momentum modes in spontaneous parametric down-conversion," *Phys. Rev. A* **79**, 055805 (2009).
- [119] S. P. Walborn, A. N. de Oliveira, R. S. Thebaldi, and C. H. Monken, "Entanglement and conservation of orbital angular momentum in spontaneous parametric down-conversion," *Phys. Rev. A* **69**, 023811 (2004).
- [120] J. P. Torres, A. Alexandrescu, S. Carrasco, and L. Torner, "Quasi-phase-matching engineering for spatial control of entangled two-photon states," *Opt. Lett.* **29**, 376 (2004).
- [121] T. Yarnall, A. F. Abouraddy, B. E. Saleh, and M. C. Teich, "Spatial coherence effects on second- and fourth-order temporal interference," *Opt. Express* **16**, 7634 (2008).
- [122] C. H. Bennett, H. J. Bernstein, S. Popescu, and B. Schumacher, "Concentrating partial entanglement by local operations," *Phys. Rev. A* **53**, 2046 (1996).
- [123] H. H. Arnaut and G. A. Barbosa, "Orbital and intrinsic angular momentum of single photons and entangled pairs of photons generated by parametric down-conversion," *Phys. Rev. Lett.* **85**, 286 (2000).
- [124] G. Molina-Terriza, S. Minardi, Y. Deyanova, C. I. Osorio, M. Hendrych, and J. P. Torres, "Control of the shape of the spatial mode function of photons generated in noncollinear spontaneous parametric down-conversion," *Phys. Rev. A* **72**, 065802 (2005).
- [125] S. Feng and P. Kumar, "Spatial symmetry and conservation of orbital angular momentum in spontaneous parametric down-conversion," *Phys. Rev. Lett.* **101**, 163602 (2008).

- [126] L. Allen, M. W. Beijersbergen, R. J. C. Spreeuw, and J. P. Woerdman, "Orbital angular momentum of light and the transformation of Laguerre-Gaussian laser modes", *Phys. Rev. A* **45**, 8185 (1992).
- [127] G. S. Agarwal, "SU(2) structure of the Poincaré sphere for light beams with orbital angular momentum", *J. Opt. Soc. Am. A* **16**, 2914 (1999).
- [128] S. A. Ponomarenko, "A class of partially coherent beams carrying optical vortices", *J. Opt. Soc. Am. A* **18**, 150 (2001).
- [129] J. Serna and J. M. Movilla, "Orbital angular momentum of partially coherent beams", *Opt. Lett.* **26**, 405 (2001).
- [130] G. V. Bogatyryova, C. V. Fel'Ďe, P. V. Polyanskii, S. A. Ponomarenko, M. S. Soskin, and E. Wolf, "Partially coherent vortex beams with a separable phase", *Opt. Lett.* **28**, 878 (2003).
- [131] D. M. Palacios, I. D. Maleev, A. S. Marathay, and G. A. Swartzlander, "Spatial correlation singularity of a vortex field", *Phys. Rev. Lett.* **92**, 143905 (2004).
- [132] Y. D. Liu, C. Gao, M. Gao, and F. Li, "Coherent-mode representation and orbital angular momentum spectrum of partially coherent beam", *Opt. Commun.* **281**, 1968 (2007).
- [133] W. H. Carter and E. Wolf, "Coherence and radiometry with quasihomogeneous planar sources", *J. Opt. Soc. Am. A* **67**, 785 (1977).
- [134] M. Abramowitz and I. Stegun, *Handbook of Mathematical Functions* (Dover, New York, 1972).
- [135] I. S. Gradshteyn and I. M. Ryzhik, *Table of Integrals, Series and Products* (Academic Press, 2007).
- [136] R. Zambrini and S. M. Barnett, "Quasi-intrinsic angular momentum and the measurement of its spectrum," *Phys. Rev. Lett.* **96**, 113901 (2006).
- [137] G. Toraldo Di Francia, "Resolving power and information," *J. Opt. Soc. Am.* **45**, 497 (1955).
- [138] M.S. Soskin and M.V. Vasnetsov, "Singular Optics" in *Progress in Optics*, E. Wolf, ed. (Elsevier, Amsterdam, 2001), Vol. 42, pp. 219–276.
- [139] J. F. Nye and M. V. Berry, "Dislocations in wave trains," *Proc. R. Soc. London A, Ser. A* **336**, 165–190 (1974).
- [140] L. Allen, S. M. Barnett, and M. J. Padgett, eds., "Optical Angular Momentum" (IOP, 2003).

- [141] G. P. Karman, M. W. Beijersbergen, A. van Duijl, and J. P. Woerdman, "Creation and annihilation of phase singularities in a focal field," *Opt. Lett.* **22**, 1503–1505 (1997).
- [142] I. V. Basistiy, M. S. Soskin, and M. V. Vasnetsov, "Optical wavefront dislocations and their properties," *Opt. Comm.* **119**, 604–612 (1995).
- [143] S. A. Ponomarenko and E. Wolf, "Spectral anomalies in a Fraunhofer diffraction pattern," *Opt. Lett.* **27**, 1211–1213 (2002).
- [144] H. F. Schouten, G. Gbur, T. D. Visser, and E. Wolf, "Phase singularities of the coherence functions in young's interference pattern," *Opt. Lett.* **28**, 968–970 (2003).
- [145] F. Gori, M. Santarsiero, R. Borghi, and S. Vicalvi, "Partially coherent sources with helicoidal modes," *J. Mod. Opt.* **45**, 539–554 (1998).
- [146] G. Gbur and T. D. Visser, "Coherence vortices in partially coherent beams," *Opt. Comm.* **222**, 117–125 (2003).
- [147] I. Maleev, D. Palacios, A. Marathay, and G. Swartzlander, Jr., "Spatial correlation vortices in partially coherent light: theory," *J. Opt. Soc. Am. B* **21**, 1895–1900 (2004).
- [148] G. Gbur and T. D. Visser, "Phase singularities and coherence vortices in linear optical systems," *Opt. Comm.* **259**, 428–435 (2005).
- [149] I. Maleev and G. Swartzlander, Jr., "Propagation of spatial correlation vortices," *J. Opt. Soc. Am. B* **25**, 915–922 (2008).
- [150] G. Gbur and G. A. Swartzlander, Jr., "Complete transverse representation of a correlation singularity of a partially coherent field," *J. Opt. Soc. Am. B* **25**, 1422–1429 (2008).
- [151] T. van Dijk, H. F. Schouten, and T. D. Visser, "Coherence singularities in the field generated by partially coherent sources," *Phys. Rev. A* **79**, 033805 (2009).
- [152] G. A. Swartzlander, Jr. and R. I. Hernandez-Aranda, "The optical Rankine vortex and the anomalous circulation of light," *Phys. Rev. Lett.* **99**, 163901 (2007).
- [153] G. Bogatyryova, C. Fel'de, P. Polyanskii, S. Ponomarenko, M. Soskin, and E. Wolf, "Partially coherent vortex beams with a separable phase," *Opt. Lett.* **28**, 878–880 (2003).
- [154] D. M. Palacios, I. D. Maleev, A. S. Marathay, and G. A. Swartzlander, Jr., "Spatial correlation singularity of a vortex field," *Phys. Rev. Lett.* **92**, 143905 (2004).

- [155] K. Motzek, Y. Kivshar, M. Shih, and G. Swartzlander, Jr., "Spatial coherence singularities and incoherent vortex solitons," *J. Opt. Soc. Am. B* **22**, 1437–1442 (2005).
- [156] W. Wang, Z. Duan, S. G. Hanson, Y. Miyamoto, and M. Takeda, "Experimental study of coherence vortices: Local properties of phase singularities in a spatial coherence function," *Phys. Rev. Lett.* **96**, 073902 (2006).
- [157] H. Di Lorenzo Pires, J. Woudenberg, and M. P. van Exter, "Measurement of the orbital angular momentum spectrum of partially coherent beams," *Opt. Lett.* **35**, 889–891 (2010).
- [158] I. Maleev, "Partial coherence and optical vortices," PhD thesis (Worcester Polytechnic Institute, 2004), [http://www.wpi.edu/Pubs/ETD/Available/etd-0713104-021808/unrestricted/Maleev\\_PhD.pdf](http://www.wpi.edu/Pubs/ETD/Available/etd-0713104-021808/unrestricted/Maleev_PhD.pdf).
- [159] Z. Sacks, D. Rozas, and G. Swartzlander, Jr., "Holographic formation of optical-vortex filaments," *J. Opt. Soc. Am. B* **15**, 2226–2234 (1998).
- [160] B. Saleh and M. Rabbani, "Simulation of partially coherent imagery in the space and frequency domains and by modal expansion," *Appl. Opt.* **21**, 2770–2777 (1982).
- [161] D. Fischer, S. Prah, and D. Duncan, "Monte Carlo modeling of spatial coherence: free-space diffraction," *J. Opt. Soc. Am. A* **25**, 2571–2581 (2008).
- [162] A. Burvall, A. Smith, and C. Dainty, "Elementary functions: propagation of partially coherent light," *J. Opt. Soc. Am. A* **26**, 1721–1729 (2009).
- [163] M. Santarsiero and R. Borghi, "Measuring spatial coherence by using a reversed-wavefront Young interferometer," *Opt. Lett.* **31**, 861–863 (2006).
- [164] C. Q. Tran, G. J. Williams, A. Roberts, S. Flewett, A. G. Peele, D. Paterson, M. D. de Jonge, and K. A. Nugent, "Experimental measurement of the four-dimensional coherence function for an undulator x ray source," *Phys. Rev. Lett.* **98**, 224801 (2007).
- [165] K. Wicker, S. Sindbert, and R. Heintzmann, "Characterisation of a resolution enhancing image inversion interferometer," *Opt. Express* **17**, 15491–15501 (2009).
- [166] D. Mendlovic, G. Shabtay, A. Lohmann, and N. Konforti, "Display of spatial coherence," *Opt. Lett.* **23**, 1084–1086 (1998).
- [167] C. C. Cheng, M. G. Raymer, and H. Heier, "A variable lateral-shearing Sagnac interferometer with high numerical aperture for measuring the complex spatial coherence of light," *J. Mod. Opt.* **47**, 1237–1246 (2000).

- 
- [168] B. Smith, B. Killett, M. Raymer, I. Walmsley, and K. Banaszek, "Measurement of the transverse spatial quantum state of light at the single-photon level," *Opt. Lett.* **30**, 3365–3367 (2005).
- [169] E. Mukamel, K. Banaszek, I. Walmsley, and C. Dorrer, "Direct measurement of the spatial Wigner function with area-integrated detection," *Opt. Lett.* **28**, 1317–1319 (2003).
- [170] A. Savitzky and M. J. E. Golay, "Smoothing and differentiation of data by simplified least squares procedures," *Anal. Chem.* **36**, 1627–1639 (1964).
- [171] J. W. Goodman, *Speckle Phenomena in Optics: Theory and Applications* (Roberts & Company, Greenwood Village, CO, 2007).
- [172] J. W. Goodman, "Some fundamental properties of speckle," *Opt. Soc. Am.* **66**, 1145 (1976).
- [173] S. Washburn and R. A. Webb, "Quantum transport in small disordered samples from the diffusive to the ballistic regime," *Rep. Prog. Phys.* **55**, 1311 (1992).
- [174] C. W. J. Beenakker, "Random-matrix theory of quantum transport," *Rev. Mod. Phys.* **69**, 731 (1997).
- [175] M. P. Van Albada and A. Lagendijk, "Observation of weak localization of light in a random medium," *Phys. Rev. Lett.* **55**, 2692 (1985).
- [176] D. S. Wiersma, P. Bartolini, A. Lagendijk, and R. Righini, "Localization of light in a disordered medium," *Nature* **390**, 671 (1997).
- [177] M. Patra and C. W. J. Beenakker, "Propagation of squeezed radiation through amplifying or absorbing random media," *Phys. Rev. A* **61**, 063805 (2000).
- [178] A. Aiello and J. P. Woerdman, "Intrinsic entanglement degradation by multimode detection," *Phys. Rev. A* **70**, 023808 (2004).
- [179] J. L. van Velsen and C. W. J. Beenakker, "Transition from pure-state to mixed-state entanglement by random scattering," *Phys. Rev. A* **70**, 032325 (2004).
- [180] P. Lodahl and A. Lagendijk, "Transport of quantum noise through random media," *Phys. Rev. Lett.* **94**, 153905 (2005).
- [181] P. Lodahl, A. P. Mosk, and A. Lagendijk, "Spatial quantum correlations in multiple scattered light," *Phys. Rev. Lett.* **95**, 173901 (2005).
- [182] G. Puentes, A. Aiello, D. Voigt, and J.P. Woerdman, "Entangled mixed-state generation by twin-photon scattering," *Phys. Rev. A* **75**, 032319 (2007).

- [183] S. E. Skipetrov, "Quantum theory of dynamic multiple light scattering in fluctuating disordered media," *Phys. Rev. A* **75**, 053808 (2007).
- [184] C. W. J. Beenakker, J. W. F. Venderbos, and M. P. van Exter, "Two-photon speckle as a probe of multi-dimensional entanglement," *Phys. Rev. Lett.* **102**, 193601 (2009).
- [185] S. Smolka, A. Huck, U. L. Andersen, A. Lagendijk, and P. Lodahl, "Observation of spatial quantum correlations induced by multiple scattering of nonclassical light," *Phys. Rev. Lett.* **102**, 193901 (2009).
- [186] J. R. Ott, N. A. Mortensen, and P. Lodahl, "Quantum interference and entanglement induced by multiple scattering of light," *Phys. Rev. Lett* **105**, 090501 (2010).
- [187] W. H. Peeters, J. J. D. Moerman, and M. P. van Exter, "Observation of two-photon speckle patterns," *Phys. Rev. Lett* **104**, 173601 (2010).
- [188] Y. Lahini, Y. Bromberg, D.N. Christodoulides, and Y. Silberberg, "Quantum correlations in two-particle anderson localization," *Phys. Rev. Lett.* **105**, 163905 (2010).
- [189] L. C. Andrews and R. L. Phillips, *Laser Beam Propagation through Random Media* (SPIE, Bellingham, WA, 2005).

# List of publications

- H. Di Lorenzo Pires and C. H. Monken, *On the statistics of the entropy-depolarization relation in random light scattering*, *Opt. Express* **16**, 21059 (2008).
- H. Di Lorenzo Pires and M. P. van Exter, *Observation of near-field correlations in spontaneous parametric down-conversion*, *Phys. Rev. A* **79**, 041801(R) (2009).
- H. Di Lorenzo Pires, C. H. Monken, and M. P. van Exter, *Direct measurement of transverse mode entanglement in two-photon states*, *Phys. Rev. A* **80**, 022307 (2009).
- H. Di Lorenzo Pires and M. P. van Exter, *Near-field correlations in the two-photon field*, *Phys. Rev. A* **80**, 053820 (2009).
- H. Di Lorenzo Pires, H. C. B. Florijn, and M. P. van Exter, *Measurement of the Spiral Spectrum of Entangled Two-Photon States*, *Phys. Rev. Lett.* **104**, 020505 (2010).
- H. Di Lorenzo Pires, J. Woudenberg, and M. P. van Exter, *Measurement of the orbital angular momentum spectrum of partially coherent beams*, *Opt. Lett.* **35**, 889 (2010).
- H. Di Lorenzo Pires, J. Woudenberg, and M. P. van Exter, *Measurements of spatial coherence of partially coherent light with and without orbital angular momentum*, *J. Opt. Soc. Am. A* **27**, 2630 (2010).
- H. Di Lorenzo Pires, F. M. G. J. Coppens, and M. P. van Exter, *Type-I spontaneous parametric down conversion with a strongly focused pump*, *Phys. Rev. A* **38**, 033837 (2011).
- H. Di Lorenzo Pires, J. Woudenberg, and M. P. van Exter, *Statistical properties of non-local speckles*. (Manuscript submitted).
- M. P. van Exter, J. Woudenberg, H. Di Lorenzo Pires, and W. H. Peeters, *Bosonic, fermionic, and anyonic behavior in two-photon scattering*. (Manuscript submitted)



# Summary

Light is classically described as an electromagnetic wave. At the most fundamental level, however, physicists describe it in terms of *photons*, which are the fundamental particles or quanta of light. In this thesis we investigate some intriguing spatial properties of photons. In special, we generate a light field containing two photons that are correlated in a way that cannot be described classically. Among the questions we address are: How are these photon pairs distributed in space? How do they propagate? Can we verify that the correlations are indeed quantum?

Most of the work presented in this thesis is experimental, but in order to fully appreciate the essence of the studied phenomena, we have developed new theoretical tools as well. Our main motivation is to get new insights into the nature of quantum correlated photons, which could possibly be applied in the rapidly developing field of quantum information.

In this summary we describe our most important results and the basic physics behind our experiments. The discussion is structured around the four key themes in this thesis.

## Spatial coherence (Chapter 1)

Many of the most important experiments in optics involve interference of light. For instance, by sending a laser beam through narrow slits, interference fringes will be observed on a screen behind the slits. Interference only occurs when the oscillations of the light *wave* at the slits are perfectly synchronized. A light beam with this property is denominated *completely coherent*.

In our everyday experience with light, however, interference effects are rarely observed. If you illuminate an object with a laser, sharp maxima and minima in the intensities can be seen in the transmitted or reflected beam. If you repeat the same experiment with a (monochromatic) “normal” light source, like a LED lamp, the intensity of the transmitted or reflected light will generally be uniform or smoothly varying. The reason is that normal light sources, unlike laser beams, are *incoherent*. The field at different points of space is randomly oscillating such that all interference effects are quickly averaged out and cannot be observed.

Completely coherent light can produce interference patterns with very high contrast, whereas completely incoherent light cannot produce any interference

at all. These are the two extreme cases, but most fields are in practice partially coherent, that is, they can produce some interference depending on their degree of coherence.

**Chapter 1** formally introduces the concept of spatial coherence and discusses some basic mathematical tools necessary for the following chapters. The concept is extended to the quantum domain and higher order correlation functions are introduced. At the quantum level, light can be described in terms of *photons*. Chapter 1 also sets the stage for the next chapters, which mainly investigate the quantum properties of photons.

### **Quantum entanglement (Chapters 2-5)**

One of the most bizarre premises of quantum theory, which has long fascinated philosophers and physicists, states that by the very act of watching, the observer affects the observed reality. This is caricatured in the famous Schrödinger paradox, which presents a cat in closed box. In this thought experiment the cat can be in a superposition state, where he is *at the same time* “alive” and “dead”, until we open the box and look inside it. At this moment the reality has to “collapse” in one possible result, and the fate of the poor cat is determined.

Consider now a system with two quantum particles. Under some conditions, it can happen that by observing the “reality” of the first particle, the “reality” of the other particle can be instantaneously determined; no matter where it is. This property, which is called *entanglement*, is the property of quantum mechanics that caused Einstein and others to dislike the theory. It violates the philosophical principles of realism and locality. Fortunately, this almost magical link between two objects can be relatively easily realized in the labs.

In most of our experiments we generate photon pairs that are quantum entangled in their positions. This can be obtained via the interaction of a laser beam with a nonlinear crystal, in a process known as spontaneous parametric down conversion (SPDC).

**Chapters 2 and 3** investigate the spatial properties of entangled photon pairs. We explore a region known as the *near field*, which is the plane corresponding to an image of the crystal and which can be easily accessed using a single lens. Using two photon counters, we measure the spatial distribution of photon 2 once the position of photon 1 is known. This simultaneous “click” of two detectors, known as a coincidence measurement, allows us to reconstruct the *wavefunction* of the photon pairs.

The results reveal many interesting and yet unknown spatial correlations. We observe spatial antibunching of light, an extreme localization of photon pairs, and spatial correlations that resemble Bessel beams in propagation. We also link our observations to well-known phenomena in classical optics, such as second harmonic generation and phase-singularities.

**Chapter 4** explores the boundaries between the classical and the quantum

---

description of the two-photon field. Most experiments with spontaneous parametric down conversion have focused on the quantum correlations between the two generated photons. This chapter investigates, instead, the classical properties of the field. We use a strongly focused laser beam to generate photon pairs and we observe the intensity patterns with an ordinary CCD camera. When the laser beam is strongly focused, the measured correlations are *almost* classical.

There are many theories that provide mathematical expressions to quantify the amount of entanglement associated with the position of photon pairs. The equations are usually derived in a quite abstract way and actual computations are difficult and time demanding. In **Chapter 5** we provide an operational meaning to one of the most important entanglement quantifiers, namely, the Schmidt number. Contrary to what is usually assumed, we show that this number can be experimentally estimated in a straightforward way. To this end, we explore a link between the mathematics of entanglement and the mathematics of classical optics.

### **Orbital angular momentum (Chapters 6-8)**

Physicists have known for a long time that light has some properties that are usually associated with particles, for instance, a light beam can carry linear and angular momentum. Loosely speaking, angular momentum is associated with “rotations”, and like a planet that orbits a star and also rotates around its axis, the angular momentum of light can be decomposed into orbital and spin components. The spin of light is associated with circular polarization, while the orbital part is related to a vortex phase structure of the electromagnetic field.

It is now recognized that this angular momentum is a property of the photons. The angular momentum content of a photon is quantized, being an integer multiple  $\ell$  of Planck’s constant  $\hbar$ . Photonic states carrying angular momentum are specially important because quantum information can be encoded in the index  $\ell$  of the photons.

The photons we generate via SPDC are also entangled in orbital angular momentum (OAM). If we measure one photon with an OAM equal to  $\ell\hbar$ , the other photon will have an OAM equal to  $-\ell\hbar$ . The probability  $P_\ell$  of finding  $(\ell, -\ell)$  pairs depends, however, on the number  $\ell$ . In **Chapter 6** we show how these correlations can be experimentally measured. We implement an interferometric technique that allows us to obtain the distribution  $P_\ell$ , which fully characterizes the entanglement structure. Furthermore, we show how we can manipulate and increase the number of generated modes in an efficient way.

**Chapter 7** focuses on the angular momentum distribution of single photons, instead of photon pairs. Classical sources of light, like a LED lamp, can also generate photons with angular momentum. But in general, the fraction of generated photons carrying negative and positive OAM are practically the same, such that the overall OAM content of the light source is null. In this chapter we experi-

mentally investigate what is exactly the fraction of photons carrying OAM equal to  $\ell\hbar$ . We also show how this distribution can be changed.

The overall orbital angular momentum content of a light beam can be modified by so-called spiral phase plates. These plates modify the phase structure of the field and can therefore decrease or increase the OAM. Most experiments with spiral phase plates use a completely coherent beam, like a laser. In **Chapter 8**, however, we present an experimental investigation of the effect of a spiral phase plate on *partially coherent beams*. When partially coherent light is transmitted through a spiral phase plate, the field will reveal *correlation singularities*, which can only be observed by interfering the field with itself. We present measurements of the coherence function for fields possessing coherence singularities.

### **Scattering (Chapter 9)**

When a completely coherent light, like a laser beam, is transmitted through or reflected from a random medium (e.g., milk, white paint, diffusor) the intensity will be a speckled pattern of bright and dark spots. This pattern carries information both on the coherence properties of the radiation and on the microscopic details of the scattering object. For many realizations of the disorder, statistical arguments can be used in order to recover useful information.

When entangled photon pairs are transmitted through a random medium, a random pattern is also revealed in the coincidences rate measured by two detectors. It is a speckle pattern in the *correlation* between the positions of the two photons. **Chapter 9** experimentally investigates the statistics of these patterns. In this final chapter, most of the phenomena investigated in the previous chapters are put together in a single context. We show how spatial entanglement gives two-photon speckles a richer structure and we discuss the striking differences between a highly entangled state and a non-entangled state. An interesting link between spatial coherence, spatial entanglement, and speckle statistics offers a novel way to measure the number of entangled modes (the Schmidt number).

# Samenvatting

Licht kan klassiek beschreven worden als een elektromagnetische golf. Op het meest fundamentele niveau beschrijven natuurkundigen licht echter als fotonen; de fundamentele deeltjes of quanta van licht. In dit proefschrift onderzoeken wij een aantal ruimtelijke eigenschappen van fotonen. We gebruiken hiervoor een lichtveld dat bestaat uit fotonparen die gecorreleerd zijn op een manier die niet op een klassieke wijze beschreven kan worden. Enkele vragen die wij behandelen zijn: Hoe zijn deze fotonparen ruimtelijk verdeeld? Hoe planten zij zich voort? Kunnen we verifiëren dat de correlaties inderdaad quantumcorrelaties zijn?

Het meeste werk in dit proefschrift is experimenteel. Om de essentie van de bestudeerde fenomenen volledig te kunnen doorgronden hebben we ook nieuwe theoretische methoden ontwikkeld. Onze belangrijkste motivatie is het verkrijgen van nieuwe inzichten in de aard van quantumgecorrleerde fotonen, die zouden kunnen worden toegepast in het snel ontwikkelende veld van de quantuminformatie.

In deze samenvatting beschrijven wij onze belangrijkste resultaten en de natuurkunde die aan deze experimenten ten grondslag ligt. Dit is gestructureerd rond de vier hoofdthema's van dit proefschrift.

## Ruimtelijke coherentie (Hoofdstuk 1)

Veel belangrijke experimenten in de optica gaan over de interferentie van licht. Wanneer bijvoorbeeld een laserstraal door nauwe spleetjes gaat, kan een interferentiepatroon waargenomen worden op een scherm achter de spleetjes. Interferentie treedt alleen op wanneer de oscillaties van de lichtgolven bij de spleten perfect gesynchroniseerd zijn. Een lichtstraal met deze eigenschap heet compleet coherent.

In het dagelijks leven kun je interferentie-effecten van licht echter zelden waarnemen. Wanneer je een object belicht met een laser, kun je scherpe maxima en minima in de intensiteit zien van de doorgaande of de gereflecteerde bundel. Wanneer je ditzelfde experiment herhaalt met een (monochromatische) 'normale' lichtbron, zoals een LED-lamp, dan zal de intensiteit van de doorgaande of gereflecteerde bundel over het algemeen uniform zijn of slechts geleidelijk variërend. De reden hiervoor is dat normale lichtbronnen, in tegenstelling

tot laserstralen, incoherent zijn. Het veld op verschillende punten in de ruimte oscilleert willekeurig zodat interferentie-effecten snel worden uitgemiddeld en niet geobserveerd kunnen worden.

Volledig coherent licht kan interferentiepatronen produceren met zeer hoog contrast, terwijl compleet incoherent licht helemaal geen interferentie geeft. Dit zijn de twee extreme gevallen, maar de meeste velden zijn in de praktijk gedeeltelijk coherent, wat betekent dat ze wat interferentie kunnen produceren; de mate waarin ze dit doen hangt af van hun coherentie.

**Hoofdstuk 1** introduceert formeel het concept van ruimtelijke coherentie en beschrijft enkele wiskundige middelen die nodig zijn voor de volgende hoofdstukken. Het concept van ruimtelijke coherentie wordt daarna uitgebreid naar het quantumdomein en hogere-orde-correlatiefuncties worden geïntroduceerd. Op quantumniveau kan licht beschreven worden in termen van fotonen. Hoofdstuk 1 leidt ook de volgende hoofdstukken in die vooral gaan over de quantumeigenschappen van fotonen.

### **Quantumverstregeling (Hoofdstukken 2-5)**

Eén van de meest bizarre vooronderstellingen van de quantumtheorie, iets wat filosofen en natuurkundigen al lang fascineert, is het bestaan van toestanden waarbij de geobserveerde realiteit beïnvloed wordt door het waarnemen ervan. Een voorbeeld hiervan is de beroemde Schrödinger paradox over een kat in een gesloten doos. In dit gedachte-experiment bevindt de kat zich in een superpositie toestand, waarin hij tegelijkertijd dood en levend is, totdat we de doos openen en erin kijken. Op dit moment moet de realiteit ineens tot één mogelijk resultaat en wordt het lot van de arme kat bepaald.

Beschouw nu een systeem met twee quantumdeeltjes. Onder sommige omstandigheden kan het gebeuren dat, door de realiteit van het eerste deeltje waar te nemen, de realiteit van het andere deeltje ogenblikkelijk kan worden bepaald; onafhankelijk van waar het is. Deze eigenschap, die verstregeling heet, is de voornaamste reden dat Einstein en anderen een afkeer hadden voor de quantummechanica. Het is namelijk in tegenspraak met filosofische principes van realisme en plaats. Gelukkig kan deze bijna magische verbinding tussen twee objecten nu relatief gemakkelijk worden gerealiseerd in laboratoria.

In de meeste van onze experimenten wekken we fotonparen op die quantumverstregeld zijn in hun ruimtelijke vrijheidsgraden. Dit gebeurt door de interactie van een laserstraal met een optisch niet-lineair kristal, in een proces dat bekend staat als "spontaneous parametric down conversion (SPDC)".

**Hoofdstukken 2 en 3** gaan over de ruimtelijke eigenschappen van verstregelde fotonparen. We verkennen een gebied dat bekend staat als het nabije veld. Dit vlak correspondeert met de afbeelding van het kristal en kan gemakkelijk worden bereikt met een enkele lens. Wij meten de gecombineerde posities van foton 1 en foton 2 met twee fototellers. Het ruimtelijk profiel van deze zogenaamde "coincidence count" staat ons toe om de golf functie van de fotonparen te recon-

---

strueren. De resultaten laten vele interessante en tot dusver onbekende ruimtelijke correlaties zien. Hierbij zien we ruimtelijke “antibunching” van licht, een extreme lokalisering van fotonparen en ruimtelijke correlaties die lijken op Bessel stralen in voortplanting. Wij vergelijken onze waarnemingen met bekende fenomenen in de klassieke optica, zoals tweede harmonische generatie en fase-singulariteiten.

**Hoofdstuk 4** verkent de grens tussen de klassieke- en quantumbeschrijving van het twee-fotonveld. De meeste experimenten met “spontaneous parametric down conversion” hebben zich gericht op de quantumcorrelaties tussen de twee opgewekte fotonen. Dit hoofdstuk beschrijft echter de klassieke eigenschappen van het veld. We gebruiken een sterk gefocusseerde laserstraal om fotonparen op te wekken en we nemen de intensiteitspatronen op met een gewone CCD camera. Wanneer de laserstraal sterk gefocusseerd is, zijn de gemeten correlaties bijna klassiek.

Er zijn veel theorieën die wiskundige formules geven om de hoeveelheid verstrengeling te kwantificeren die geassocieerd is met de positie van fotonparen. De formules worden meestal op een vrij abstracte manier afgeleid en daadwerkelijke berekeningen zijn moeilijk en tijdrovend. **Hoofdstuk 5** presenteert een gebruiksformule van één van de belangrijkste verstrengelingsuitdrukkingen, het Schmidt getal. In tegenstelling tot wat meestal wordt aangenomen, laten we zien dat dit getal experimenteel redelijk eenvoudig kan worden geschat. Om dit te doen verkennen we de overeenkomst tussen de wiskunde van verstrengeling en de wiskunde van klassieke optica.

### **Baan draaiimpuls (Hoofdstukken 6-8)**

Natuurkundigen weten al lang dat licht een aantal eigenschappen heeft die normaal gesproken worden geassocieerd met deeltjes. Een lichtstraal kan bijvoorbeeld een lineair impuls en een draaiimpuls hebben. De draaiimpuls kan geassocieerd worden met “rotaties”. Zoals een planeet die in een baan rond een ster loopt en daarnaast ook rond zijn eigen as draait, zo kan de draaiimpuls van licht onderverdeeld worden in baan- en spincomponenten. De spin van licht wordt geassocieerd met circulaire polarisatie, terwijl de baancomponent gerelateerd is aan een vortex fase structuur van het elektromagnetische veld.

Tegenwoordig is bekend dat deze draaiimpuls een eigenschap is van de fotonen. De draaiimpuls kan niet alle waarden aannemen, maar is een veelvoud van een geheel getal  $\ell$  maal de constante van Planck  $\hbar$ . Fotonische toestanden met een draaiimpuls zijn belangrijk omdat quantuminformatie gecodeerd kan worden in de index  $\ell$  van de fotonen.

De fotonen die wij opwekken via SPDC zijn ook verstrengeld in de baan draaiimpuls (ofwel “orbital angular momentum” OAM). Als we één foton meten met een OAM gelijk aan  $\ell\hbar$ , dan heeft het andere foton een OAM van  $-\ell\hbar$ . De waarschijnlijkheid  $P_\ell$  om  $(\ell, -\ell)$  paren te vinden hangt echter af van het getal  $\ell$ .

In **Hoofdstuk 6** laten we zien hoe deze correlaties experimenteel kunnen worden gemeten. We ontwikkelen en demonstreren een interferometrische techniek om de verdeling van  $P_\ell$  te meten; deze verdeling geeft een volledig beeld van de ruimtelijke verstrengeling. Bovendien laten we zien hoe we op een efficiënte manier het aantal gegenereerde toestanden kunnen aanpassen en vergroten.

**Hoofdstuk 7** gaat over de verdeling van de draaiimpuls van losse fotonen in plaats van fotonparen. Klassieke lichtbronnen, zoals een LED-lamp, kunnen ook fotonen opwekken met een draaiimpuls. Over het algemeen is het deel fotonen met negatieve en positieve OAM praktisch hetzelfde, zodat de totale OAM-inhoud van de lichtbron nul is. In dit hoofdstuk onderzoeken wij experimenteel hoe groot precies het deel fotonen is met OAM gelijk aan  $\ell\hbar$ . We laten ook zien hoe deze verdeling veranderd kan worden.

De totale baan draaiimpuls inhoud van een lichtbundel kan veranderd worden met zogeheten spiraalfaseplaten. Deze platen veranderen de fasestructuur van het veld en kunnen daardoor de OAM vergroten of verkleinen. In de meeste experimenten met spiraalfaseplaten worden volledig coherente (laser)bundels gebruikt. In **Hoofdstuk 8** presenteren we echter een diepgaand experimenteel onderzoek naar het effect van een spiraalfaseplaat op gedeeltelijk coherente bundels. Wanneer we gedeeltelijk coherent licht door een spiralen faseplaat schijnen, dan zal het veld correlatiesingulariteiten vertonen, die alleen waargenomen kunnen worden door het veld met zichzelf te laten interfereren. We laten metingen zien van de coherentiefunctie voor velden met coherentiesingulariteiten.

### Verstrooiing (Hoofdstuk 9)

Wanneer compleet coherent licht, zoals laserlicht, wordt geschenen door of gereflecteerd door een ongeordend medium (zoals melk, witte verf, of diffusor), ontstaat er een gespikkeld intensiteitspatroon van lichte en donkere vlekjes. In dit patroon zit informatie over de coherentie-eigenschappen van de straling en over de microscopische details van het verstrooiende object. Voor veel soorten wanorde kunnen statistische argumenten worden gebruikt om nuttige informatie uit te halen.

Wanneer verstrengelde fotonen door een ongeordend medium worden verstrooid, ontstaat er een gespikkeld patroon in de posities van beide fotonen gecombineerd. **Hoofdstuk 9** beschrijft het experimentele onderzoek naar de statistiek van deze twee-foton patronen, die gemeten worden met twee detectoren. In dit laatste hoofdstuk worden de meeste fenomenen uit de eerdere hoofdstukken in eenzelfde context samengevoegd. We tonen aan hoe de ruimtelijke verstrengeling de twee-fotonvlekjes een rijkere structuur geeft en we bespreken de opmerkelijke verschillen tussen de patronen van een sterk verstrengelde toestand en een niet-verstrengelde toestand. Een interessant verband tussen ruimtelijke coherentie, ruimtelijke verstrengeling en spikkelstatistiek biedt een nieuwe manier om het aantal verstrengelde toestanden te meten (het Schmidt getal).

# Acknowledgements

Contrary to what is usually assumed, a Ph.D in optics does not only involve expending long hours alone in a dark lab. A successful research is a result of fruitful collaborations, scientific discussions, and a pleasant working environment. This thesis would certainly not have been possible without the effort, support, and friendship of many people, to whom I would like to express my gratitude.

First of all, I would like to acknowledge the excellent guidance provided by my co-promotor Martin van Exter, who was actively involved in the planning and implementation of all experiments described in this thesis. Martin, your passion for physics and your friendly approach as a supervisor were both inspiring and highly motivating. Thank you for your patience, for all the time spent reviewing my manuscripts, and for sharing your knowledge. I learned a lot from all our discussions. I would also like to thank my promotor Han Woerdman for the many useful advices concerning my Ph.D path and for the valuable recommendations on how to present scientific results.

During my years in the Quantum Optics group I had an unique opportunity to develop numerous professional and personal skills, which will be undoubtedly useful throughout my future work. For this, I am deeply grateful to Eric Eliel. Eric, thank you for caring so much about my progress within and outside academia, for drawing my attention to many interesting articles and conferences, and for encouraging me to face new challenges. I am very thankful to the Stichting FOM for financing this research and for investing so much in my professional development. Working for FOM was an extremely satisfying experience and I am very proud of it! In particular, I would like to thank Annette Bor and Maria Teuwissen for all the assistance provided before I moved to the Netherlands and during my Ph.D. I am also indebted to Danielle Verhoeff and Henriette van Leeuwen, whose efficient handling of all the administrative work at Leiden University allowed me to devote more time to this research.

I would like to thank Carlos Monken for all the guidance, which ultimately led me to pursue a Ph.D in the QO group in Leiden. Moreover, during his year as a visiting professor in our group I profited enormously from our long and always fun discussions. Working in the lab was even more pleasant in the company of three very enthusiastic students. I would like to thank Bastiaan Florijn, for his contributions to Chapter 6, Frans Coppens, for contributing to Chapter 4, and Jasper Woudenberg, who during both his bachelor and master internships contributed to Chapters 7, 8, and 9. Jasper, thank you also for all the good time outside the lab and for introducing me to a wealth of new experiences, from the Swiss gastronomy to entertaining action-parody movies. Many of the technical challenges I have faced during this research could only be overcome with the skillful assistance of Arno van Amersfoort and René Overgaww, from the Electronics Department, and of Fred Schenkel and Ewie de Kuyper from the Department of Fine Mechanics.

Research has always its ups and downs, but regardless of my scientific mood of the day I could always go home happy and carefree, thanks to the friendliness, encouragement, and cheerfulness of the people in the Quantum Optics group. I was very fortunate to share my office with two great colleagues, Wouter Peeters and Joris Berkhout. Wouter, thank you for all the discussions on entanglement

and scattering of light, for teaching me how to be a more methodical experimentalist, and for lending me the first season of *Lost*. Joris, thanks for the discussions on optical angular momentum and for sharing your enthusiasm for cycling, baseball, the Philadelphia Phillies (and its mascot). I would also like to acknowledge all the quantum and classical optical physicists in the QO group for their direct or indirect contribution to this thesis. Michiel, thank you for your feedbacks and for posing intriguing questions. Gerard, thanks for your good humor, for sharing your wisdom, and for offering free consultancy on theoretical physics. Wolfgang, if I would continue in experimental physics, I would like to be like you! Thanks for being so enthusiastic and for being always open for discussions. Nath, thanks for making me company during the lunches, when everyone else thought that outside was a “wonderful” day. Aura, thank you for organizing the movie evenings. Sumant, thanks for telling so many amusing stories. Ljubiša, thank you for defying social rules and for making our work a more cheerful place. Philip, your Labview expertise saved me a lot of work! Frerik, thanks for being such a nice neighbor. And also the colleagues who have already left our group, Eduard, thank you for updating me with the latest rumors; Bart-Jan, for your sympathies during the world cup and for bringing me such a tasteful orange cake; Steven, for the theoretical insights; and Michele, for introducing me to nice restaurants in Leiden.

Ik zou in het bijzonder Joris en Frerik willen bedanken voor de aanmoediging om ook op het werk Nederlands te spreken. Ik begrijp hoe moeilijk het kan zijn om in een grotendeels internationale omgeving niet automatisch naar het Engels over te gaan. Maar toch hebben jullie altijd Nederlands met mij gesproken. Bedankt! Ik zou ook niet vooruit zijn gegaan zonder de ondersteuning van de familie Meulenbroek (Bernard, Nicolette, Bernard Jan, Arwen, Gwendolijn en Elisabeth), niet alleen qua Nederlands, maar ik heb enorm geprofiteerd van hun waardevolle inzicht in de Nederlandse samenleving. Dank jullie allemaal! En lieve Elisabeth, wat je voor mij betekent en gedaan hebt valt niet in woorden te vatten. Zonder je liefde, geduld en steun zou mijn promotie een stuk minder soepel zijn verlopen. Bedankt om altijd aan mijn zijde te staan! Bedankt ook voor je hulp bij het vertalen van de samenvatting.

Morar longe de casa não seria possível sem o carinho e o amor incondicional da minha família, que sempre me apoiou nas minhas decisões, mesmo quando elas trouxeram a distância e saudades. Em especial eu gostaria de agradecer ao meu pai Antônio, não só por toda a dedicação como pai, mas também por ser o físico que mais me ensinou e inspirou em toda a minha carreira; à minha mãe Rosângela, por estar sempre ao meu lado, me trazendo amor, alegria, conforto e tranquilidade; ao meu irmão Guilherme (o Gui) por todos os momentos de descontração e por trazer um tipo de sabedoria nova à família; e à minha vó Carmem, por todas as lições de vida.

# Curriculum vitae

## Henrique Di Lorenzo Pires

- 21 January 1984      Born in Belo Horizonte, Brazil
- 1995 - 2001      Secondary School, Colégio Militar de Belo Horizonte
- 2002 - 2007      B.Sc. and M.Sc. Physics, Universidade Federal de Minas Gerais, Brazil  
*Emphasis on theoretical physics*  
*Master thesis: Quantum transformations and classical optics*  
*Supervisor: Prof. dr. Carlos Monken*
- 2008 - 2011      Ph.D. Research at Leiden University, the Netherlands  
*Thesis: Spatial coherence and entanglement of light*  
*Supervisors: Dr. M. P. van Exter and Prof. dr. J. P. Woerdman*  
*Teaching assistant in Econophysics*
- 2011 -      Technical consultant and product developer at Collis B.V., the Netherlands

## Oral presentations

1. Lunteren, the Netherlands, *32nd Meeting of Atomic Molecular and Optical Physics*, 2008
2. Leiden, the Netherlands, *1st Scientific Meeting on High-Dimensional Entangled Systems*, 2009
3. Lunteren, the Netherlands, *33rd Meeting of Atomic Molecular and Optical Physics*, 2009
4. San Jose, USA, *Frontiers in Optics*, 2009
5. Delft, the Netherlands, *Solid State Quantum Information Processing seminar*, 2009
6. Leiden, the Netherlands, *This Week's Discoveries, Faculty of Science*, 2010
7. Paris - Moulin d'Ande, France, *2nd Scientific Meeting on High-Dimensional Entangled Systems*, 2010
8. Cozumel, Mexico, *Quantum Optics V*, 2010
9. Ottawa, Canada, *International Conference on Quantum Information*, 2011
10. Como, Italy, *First International Workshop on High Dimensional Entanglement*, 2011

## Poster presentations

1. Amsterdam, the Netherlands, *Photons in complex media workshop*, 2008
2. Veldhoven, the Netherlands, *Physics@FOM*, 2010
3. Lunteren, the Netherlands, *34nd Meeting of Atomic Molecular and Optical Physics*, 2010
4. Veldhoven, the Netherlands, *Physics@FOM*, 2011

## Schools

1. Hven, Sweden, *Quantum and Nonlinear Optics Summer School*, 2008
2. London, England, *LERU Doctoral Summer School: Essential Enterprise Skills for Early Career Researchers*, 2011